Design and Analysis of Switching Circuits for Energy Harvesting in Piezostrutures

Woon Kyung Kim

Dissertation submitted to the faculty of the Virginia Polytechnic Institute and State University in partial fulfillment of the requirements for the degree of

Doctor of Philosophy

In

Mechanical Engineering

Andrew J. Kurdila, Chair

Daniel J. Inman

Shashank Priya

John A. Burns

Alper Erturk

August 6, 2012
Blacksburg, Virginia

Keywords: hybrid continuous-discrete system, piezoelectric material, energy harvesting, switching circuit systems, averaging method, PWM signal

Design and Analysis of Switching Circuits for Energy Harvesting in Piezostrutures

Woon Kyung Kim

Abstract

This study deals with a general method for the analysis of a semi-active control technique for a fast-shunt switching system. The benefit of the semi-active system is the reduction in power consumption, which is a significant disadvantage of a fully active system compared with a passive system. A semi-active system under consideration is a semi-actively shunted piezoelectric system, which converts the strain energy into electrical energy through strong electromechanical coupling achieved though the piezoelectric phenomenon.

Our proposed semi-active approach combines a PZT-based energy harvesting with a fast switching system driven by a Pulse-Width Modulated (PWM) signal. The fast switching system enables continuous adaptation of vibration energy control/harvesting by varying the PWM duty cycle. This contrasts with a conventional capacitance switching system that can only change the capacitance at discrete values.

The analysis of the current piezoelectric system combined with a fast-switching system poses a considerable challenge as it contains both continuous and discrete characteristics.

The study proposes an enhanced averaging method for analyzing the piecewise linear system. The simulation of the averaged system is much faster than that of the time-varying system. Moreover, the analysis derives error bounds that characterize convergence in the time domain of the averaged system to the original system.

The dissertation begins with the derivation of the equations governing the physics of a piezostructure combined with an electrical switching shunt network. The results of the averaging analysis and numerical simulation are presented in order to provide a basis for estimating the structural responses that range between open- and short-circuit conditions which constitutes two limiting conditions. An experimental study demonstrates that the capacitive shunt bimorph piezostructure coupled with a single switch can be adjusted continuously by varying the PWM duty cycle. And the behavior of such hybrid system can be well predicted by the averaging analysis.

To my wife, daughter and unborn child

Sanghoon, Reese and Baby

whose steadfast love

inspires my work

Acknowledgements

I would like to sincerely thank my advisor, Dr. Kurdila, for his endless support, advice, and knowledge that he has given me, without which, none of this work would not be possible.

I would like to thank my committee members, Dr. Inman, Dr. Priya, Dr. Burns and Dr. Erturk for their helpful advice. They have been a great influence on me and are greatly responsible for my academic accomplishments.

I would like to thank all members of the Center for Intelligent Material Systems and Structures for their friendship, assistance, and many interesting conversation.

I would like to acknowledge the staff of the Mechanical Engineering department for their assistance during my stay in graduate school.

I would like to thank my mother for her never-ending support. Her love and encouragement are a major reason that I accomplish my goal.

I would like to thank Dr. Canfield for his support and guidance. He always encourages me to be the best at everything that I attempt and not to settle for mediocrity.

Table of Contents

Contents

List of Figures

List of Tables

Chapter 1

Introduction

With recent growth in the applications of piezoelectric materials, switching or semi-active systems have risen as an effective method to reduce undesirable disturbance or produce electrical energy [1, 2]. These systems have primarily focused on improving the performance over passive and active vibration suppression techniques. It is now well appreciated that techniques have evolved from passive, to active, and most recently to semi-active methodologies. Classical passive techniques including devices such as vibration absorbers have been widely used to reduce disturbances in systems due to their robustness and stability. However, a disadvantage of these techniques is that the effective bandwidth of absorbing frequencies is very narrow, so they require precise tuning to be effective. Active vibration attenuation arose due to the need for the improved performance over passive methods. Active control methods have focused on providing enhanced robustness and stability. However, the benefits of active control do not come without a cost: the energy requirements are increased. To address some of these apparent weaknesses of both classical passive and active vibration attenuation strategies, many researchers have started working on semi-active vibration techniques that use a switching

strategy [3, 4]. Some of these works showed that the use of a capacitive shunt circuit greatly reduces the level of broadband disturbance in active piezo actuators [5]. This approach avoids either structural change or add-on passive damping materials.

1.1 Motivation

The work in this dissertation is motivated by recent efforts to develop a Tunable Piezoceramic Vibration Absorber (TPVA) [5]. The TPVA can filter some range of resonant frequencies by controlling electrical shunt impedance. This effect is achieved by integrating series of discrete capacitances. Thus, this device absorbs energy over a broad range of resonant frequencies. One focus of our research is to design an equivalent effect obtained by varying the duty ratio of a single switch. As in the discrete architecture, the band-width lower and upper bounds are defined by short-circuit and open-circuit conditions.

The architecture of the discretely switched control system is illustrated in Figure 1-1. Figure 1-1(a) shows the switched vibration absorber controlled by a finite number of switches, thus has discrete notch frequency shifts. Figure 1-1(b) is an energy harvesting circuit integrating DC – DC converter which uses fast switching control for energy transfer into the energy storage. The proposed approach in this research is the integration of Figure 1-1(a) and Figure 1-1(b). Specifically, the electromechanical switches in Figure 1-1(a) are replaced by fast switching topology in Figure 1-1(b), so that a novel vibration tuning system with fast switching topology is created.

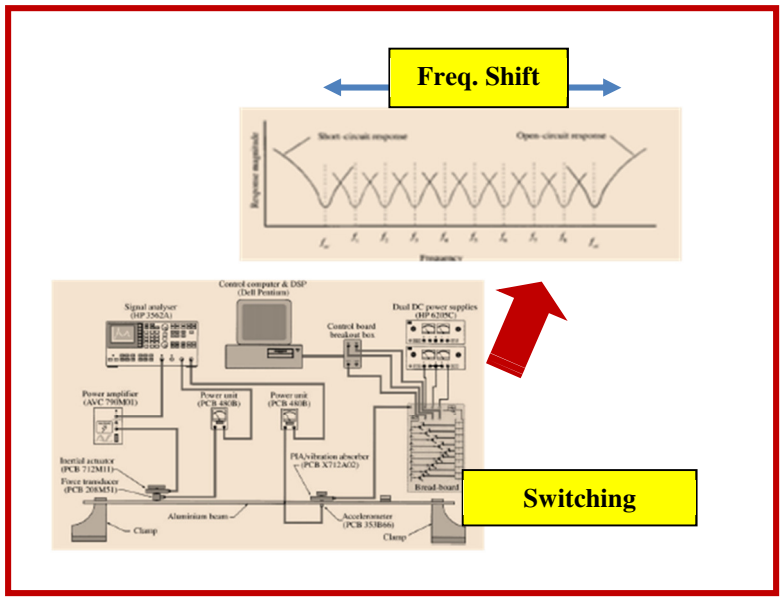

(a) Vibration absorber using a finite number of electro-mechanical switches [5].

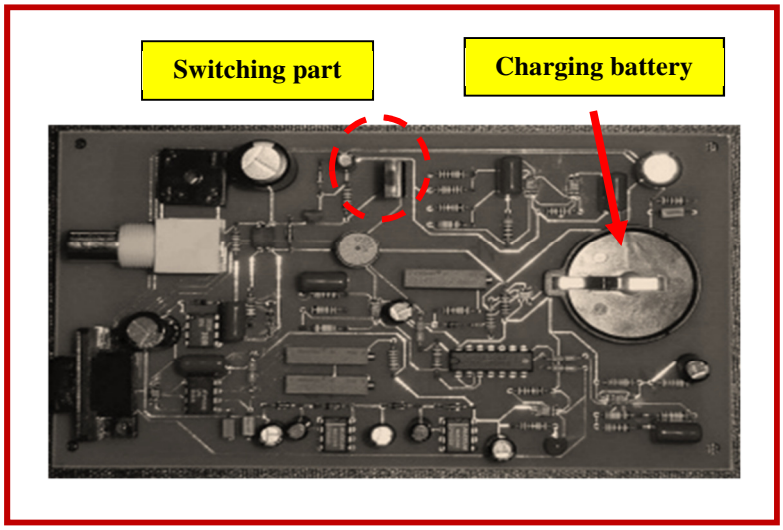

(b) Energy harvesting circuit integrating DC/DC converter: fast-operated switching [6].

Figure 1-1. Switching control strategies for vibration tuning system and energy harvesting.

1.2 Problem statement

This research derives an analytical framework based on hybrid or switched system theory for the representation of semi-actively shunted piezoelectric systems. In the case in which the gate driving frequency is a pulse-width modulated (PWM) signal, the averaging method approximates the dynamic response of the switched-shunt system. As introduced in the last section, recent study shows that piezostructures coupled to capacitances have series of notch frequencies. This research shows that a single-switched shunted piezostructure can achieve an adaptive bandwidth by varying the duty cycle of the PWM-driven signal [7]. The adaptive bandwidth of the semi-active piezoelectric system is identical to that of a corresponding discretely-switched capacitive shunted piezostructure. Questions that have arisen in development of this technology include the following:

- Can it be said that continuously-varying resonant frequency shifts are obtained through a single switching technique.

- Can an averaging analysis provide a useful tool to approximate the vibration responses in the time and frequency domains for piezostructural systems that include switched systems?

- Can this technique be extended to energy harvesting research in order to reclaim energy from periodic or ambient vibration sources?

- What is the effective switching frequency range of the PWM control signal that can be used to obtain the proper notch frequency shifts?

In the next section, we review important physics of piezoelectric materials and the general form of the constitutive laws for linear piezoelectricity.

1.3 Fundamentals and mathematics of piezoelectricity

Piezoelectricity, which originates from the Greek word "squeeze or press", decribes materials in which electric charge (electricity) is generated as a result of mechanical pressure. Historically, the direct piezoelectric effects were discovered by Pierre and Jacques Curie in 1880 in generation by crystals such as quartz. Since then, piezoelectric materials have become widespread as induced-strain transducers over the last few decades.

The poling is the process whereby non-polar or randomly-oriented dipoles are aligned in certain direction by applying a coercive electrical field, E_c, above Curie temperature, T_c. Electrical charges are distributed on the surface of the electroded ceramic as a result of polarization. It is worth noting that without the poling, the material is just inactive. Therefore, coercive field and Curie temperature are critical factors in polarization. It suffices to say that the coercive field reduces or loses the polarization, and Curie temperature is a point of phase transition, where polarization and strain vanish without electrical field.

A typical and simplified PZT molecule structure is shown in Figure 1-2. As seen in the figure, an electrically neutral charge distribution appears without external stress or disturbance. A mechanical force, causing mechanical expansion and compression in the thickness, separates the centers of positive and negative electrical charges and generates the array of dipoles. In this way, mechanical deformation is coupled to electrical charge generation and transport [8].

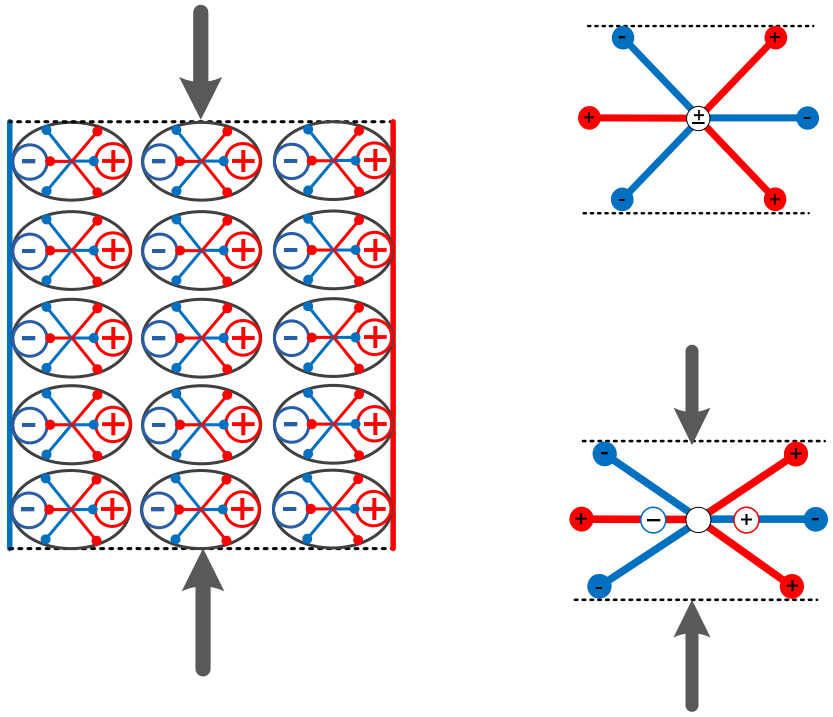

Figure 1-2. Simplified molecule structure : Before mechanical stress (upper right), after mechanical stress (lower right).

As shown Figure 1-3, piezoelectricity encompasses the two kinds of linear electro-mechanical coupling: the direct piezoelectric effect and the converse piezoelectric effect. The direct piezoelectric effect generates an electrical charge in response to applied mechanical stress or strain. In this case, crystal structures internally develop electric polarization which is linearly proportional to mechanical stress within the limited range of deformation behavior. The converse piezoelectric effect produces mechanical strain when electrical voltage (or electrical field) is applied along a certain direction. This is due to electric dipole movement causing ionic structure deformation. Piezoelectricity effects have been well documented in IEEE standards on piezoelectricity [9]. In this document, it is assumed that dynamic behavior of piezoelectricity is approximately linear and reversible within the limited strain region. Normally, the strain output of PZT (Lead zirconate titanate, $Pb(Zr, Ti)O_3$) is 0.1% ~ 0.3% [10]. The sign of electrical charge is

alternated by compressive or tensile stress and the polarization is affected by the magnitude of the mechanical stress.

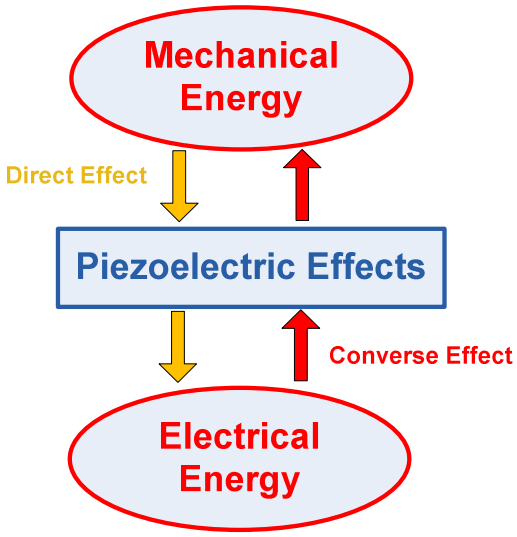

Figure 1-3. Diagram of piezoelectric effect. The conversion of energy from mechanical to electrical energies (the direct piezoelectric effect) or vice versa(The converse piezoelectric effect).

European communities have been interested in the application of piezoelectricity for several military tasks nearly one century ago. Paul Langevin and his co-workers developed an ultrasonic piezoelectric transducer to detect submarines in 1916. The transducer was a quartz crystal between thin plates and designed to be resonated around 50 kHz. A piezoelectric crystal transmitted a sound wave under water while another crystal received the rebounding signal. The distance was measured by computed time difference between transmitting and return signals.

Subsequent studies have explored and developed the piezoelectric materials in a wide range of applications. For example, piezoelectric materials have been used in

sensors such as accelerometers, microphones and voltage transformers due to their high reliability and light weight. By developing the manufacturing techniques, the enhanced actuators such as Active-Fiber Composites and Micro-Fiber Composites are common.

1.3.1 Constitutive laws for linear piezoelectric model

In this section, the general forms of the constitutive equations and electrical coupling effects for linear piezoelectricity will be discussed. The derivation of the fundamental relations of piezoelectricity is not considered in detail since many text books have dealt with this topic [11].

Table 1.1. List of symbols

Symbol	Meaning	Unit
$\mathbf{T}$ (T)	Mechanical stress vector (component)	N/m^2
$\mathbf{S}$ (S)	Mechanical strain vector (component)	m/m
$\mathbf{D}$ (D)	Dielectric displacement matrix (component)	C/m^2
$\mathbf{E}$ (E)	Electric field matrix (component)	V/m
$\mathbf{c}$ (c)	Young's modulus matrix (component)	N/m^2
$\mathbf{s}$ (s)	Compliance coefficient matrix (component)	m^2/N
$\boldsymbol{\varepsilon}$ (ε)	Dielectric permittivity matrix (component)	F/m or C/(m·V)
$\mathbf{d}$ (d)	PZT strain coefficient matrix (component)	m/V or C/N
$\mathbf{e}$ (e)	PZT stress constant matrix (component)	C/m^2
$\mathbf{g}$ (g)	PZT strain-voltage constant matrix (component)	m^2 /C or m·V/N
$\mathbf{h}$ (h)	PZT stress-voltage constant matrix (component)	V/m or N/C
	Superscripts	
$\mathbf{T}$	Values taken at constant stress $(\mathbf{T}=0)$	
$\mathbf{S}$	Values taken at constant strain $(\mathbf{S}=0)$	
$\mathbf{E}$	Values taken at constant electric field $(\mathbf{E}=0)$	
T	Transpose of a matrix (*Italic*)	
	Subscripts	
ij	Strain (or stress) is applied in the j-axis and the normal direction of the electrode is i-axis.	

Piezoelectric relations can be formulated in terms of various independent variable sets. The constitutive law shown in Table 1.2 effectively expresses the electro-mechanical coupling of piezoelectricity with respect to various independent variable sets.

Table 1.2. Linear piezoelectric relations

	Stress [N/m^2]	Strain [m/m]	
Charge [C/m^2]	$T, D \xleftarrow[c_{E=0}, e_{S=0}]{e} (S, E)$	$S, D \xleftarrow[s_{E=0}, e_{T=0}]{d} (T, E)$	Voltage
Voltage [V/m]	$T, E \xleftarrow[c_{D=0}, e_{S=0}^{-1}]{q} (S, D)$	$S, E \xleftarrow[s_{D=0}, e_{T=0}^{-1}]{g} (T, D)$	charge
	(strain)	(stress)	

As noted earlier, Piezoelectricity describes the conversion of mechanical energy to electrical energy or vice versa. The total mechanical stress is the sum of the mechanical stress due to the mechanical strain and the mechanical stress due to the electric field. Analogously, the total electric charge is the sum of the electric displacement due to the mechanical strain and the electrical displacement due to ghe applied electrical field [9]. This relationship is summarized in Equations (1.1) and (1.2).

$$\begin{aligned} \mathbf{T} &= \mathbf{c}^{\mathbf{E}} \cdot \mathbf{S} - \mathbf{e}^{T} \cdot \mathbf{E} \\ \mathbf{D} &= \mathbf{e} \cdot \mathbf{S} + \boldsymbol{\varepsilon}^{\mathbf{S}} \cdot \mathbf{E} \end{aligned} \tag{1.1}$$

$$\begin{aligned} \mathbf{S} &= \mathbf{s}^{\mathbf{E}} \cdot \mathbf{T} + \mathbf{d}^{T} \cdot \mathbf{E} \\ \mathbf{D} &= \mathbf{d} \cdot \mathbf{T} + \boldsymbol{\varepsilon}^{\mathbf{T}} \cdot \mathbf{E} \end{aligned} \tag{1.2}$$

where $\mathbf{e} = \mathbf{d} \cdot \mathbf{s}^{\mathbf{E}-1}$ and $\boldsymbol{\varepsilon}^{\mathbf{S}} = \boldsymbol{\varepsilon}^{\mathbf{T}} - \mathbf{d} \cdot \mathbf{s}^{\mathbf{E}-1} \cdot \mathbf{d}^{T}$.

Alternative forms of piezoelectric constitutive equations are summarized below:

Strain-Voltage form:

$$\begin{aligned} \mathbf{S} &= \mathbf{s}^{\mathbf{D}} \cdot \mathbf{T} + \mathbf{g}^{T} \cdot \mathbf{D} \\ \mathbf{E} &= -\mathbf{g} \cdot \mathbf{T} + \boldsymbol{\varepsilon}^{\mathbf{T}-1} \cdot \mathbf{D} \end{aligned} \tag{1.3}$$

where $\mathbf{s}^{\mathbf{D}} = \mathbf{s}^{\mathbf{E}} - \mathbf{d}^{T} \cdot \boldsymbol{\varepsilon}^{\mathbf{T}-1} \cdot \mathbf{d}$ and $\mathbf{g} = \boldsymbol{\varepsilon}_{\mathbf{T}=0}^{-1} \cdot \mathbf{d}$.

Stress-Voltage form:

$$\begin{aligned} \mathbf{T} &= \mathbf{c}^{\mathbf{D}} \cdot \mathbf{S} - \mathbf{h}^{T} \cdot \mathbf{D} \\ \mathbf{E} &= -\mathbf{h} \cdot \mathbf{S} + \boldsymbol{\varepsilon}^{\mathbf{S}-1} \cdot \mathbf{D} \end{aligned} \tag{1.4}$$

where $\mathbf{c}^{\mathbf{D}} = \mathbf{c}^{\mathbf{E}} - \mathbf{e}^{T} \cdot \boldsymbol{\varepsilon}^{\mathbf{S}-1} \cdot \mathbf{e}$ and $\mathbf{h} = \boldsymbol{\varepsilon}^{\mathbf{S}-1} \cdot \mathbf{e}$.

The piezoelectric strain constant measures the strength of coupling between mechanical and electrical fields. This constant is generally defined as the ratio of the strain developed in the j-axis to the electric field applied in the normal direction along the electrode of i-axis. Equation (1.5) represents the fact that the large piezoelectric constant results in large deformation when the generated voltage is applied.

$$d_{ij} = \frac{\text{Mechanical strain}}{\text{Applied electrical field}} \left[\frac{\text{m}}{\text{V}} \right] \tag{1.5}$$

Equation (1.6) results in alternative view of the coefficient. It is the ratio of the electrical charge at short circuit per unit area to the applied mechanical stress. The coefficient

describes how much of the electric charge flows through short circuit when the force generating strain is applied to the piezo transducer.

$$d_{ij} = \frac{\text{Short circuit charge density}}{\text{Applied mechanical strain}} \left[\frac{\text{C}}{\text{N}}\right] = k_{ij}\sqrt{\frac{\varepsilon_{jj}^{T}}{c_{ii}^{E}}} \tag{1.6}$$

The electro-mechanical coupling coefficient, k_{ij}, describes the energy conversion efficiency. More specifically, it represents the energy transfer from mechanical behavior to electrical behavior or vice versa. This coefficient measures how much of the electrical charge is stored when the piezoelectric material deforms or vice versa. In general, this coefficient has the form:

$$k_{ij} = \sqrt{\frac{\text{Stored electric energy}}{\text{Applied mechanical energy}}} = \frac{d_{ij}^{2}}{\sqrt{\varepsilon_{ii}^{T} s_{jj}^{E}}} \tag{1.7}$$

It is worth noting that this coefficient is a function of the dielectric, elastic and piezoelectric coefficients when no external force is applied.

1.3.2 Matrix form of constitutive relation

The notations in this document follow the IEEE standards for piezoelectricity and Ikeda's book [9, 11].

$$T_{ij} = c_{ijkl}^{E} S_{kl} - e_{kij} E_{k} \tag{1.8}$$

$$D_{i} = e_{ikl} S_{kl} + \varepsilon_{ij}^{S} E_{k} \tag{1.9}$$

Many possible forms of constitutive relations are encountered for linear piezoelectricity, depending on the selection of the linear independent variable set:

$$S_{ij} = s^{E}_{ijkl} T_{kl} + d_{kij} E_k \tag{1.10}$$

$$D_i = d_{ikl} T_{kl} + \varepsilon^{T}_{ik} E_k \tag{1.11}$$

The tensor forms for complete sets for linearized constitutive equations can be expressed in the summation convention shown as Equations (1.8) and (1.11). Alternately, they can be re-indexed in the forms of compact matrix notation, which are common in the literature. Figure 1-4 depicts schematically the coordinate axes when the poling direction is along the 3-axis. This matrix form replace the indices ij or kl by p or q. The correspondence between indices in the tensor and matrix notations is tabulated in Table 1.3. In the matrix notation, i and j take values of 1,2,3 and p and q take values of 1,2,3,4,5,6.

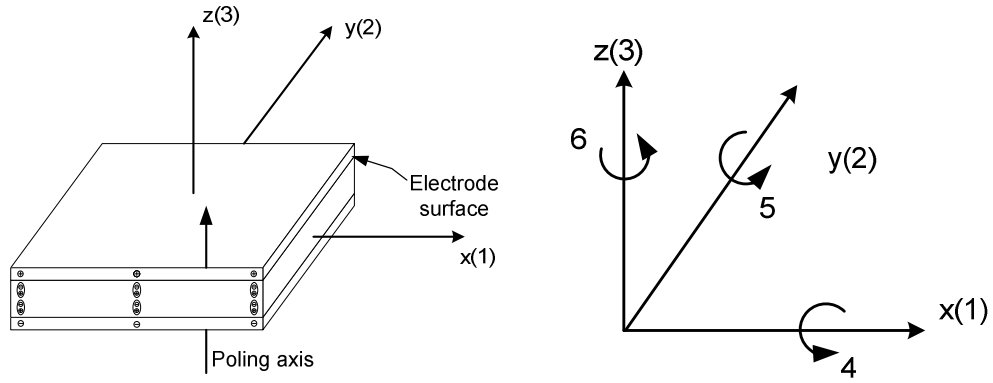

Figure 1-4. Schematic diagram indicating the coordinate axes for piezoelectric analysis.

Table 1.3. Conversion of tensor indices to matrix indices

ij or *kl*	*p* or *q*
11	1
22	2
33	3
23 or 32	4
31 or 13	5
12 or 21	6

Therefore, the tensor form of Equations is rewritten in the form of matrix

$$T_p = c_{pq}^E S_q - e_{kp} E_k \tag{1.12}$$

$$D_i = e_{iq} S_q + \varepsilon_{ik}^S E_k \tag{1.13}$$

or

$$S_p = s_{pq}^E T_q + d_{kp} E_k \tag{1.14}$$

$$D_i = d_{iq} T_q + \varepsilon_{ik}^T E_k \tag{1.15}$$

where strains are denoted

$$S_{ij} = S_p \text{ when } i = j,\ p = 1,2,3$$

$$S_{ij} = 2S_p \text{ when } i \neq j,\ p = 4,5,6$$

and compliance terms are given by

$$s_{pq}^E = s_{ijkl}^E \text{ when } i = j \text{ and } k = l \text{ or } p,q = 1,2,3$$

$$s_{pq}^E = 2s_{ijkl}^E \text{ when } i = j \text{ and } k \neq l \text{ or } p = 1,2,3,\ q = 4,5,6$$

$$s_{pq}^{E} = 4s_{ijkl}^{E} \text{ when } i \neq j \text{ and } k \neq l \text{ or } p, q = 4,5,6$$

Similarly, piezoelectric constant terms are

$$d_{iq} = d_{ikl} \text{ when } k = l \text{ or } q = 1,2,3$$

$$d_{iq} = 2d_{ikl} \text{ when } k \neq l \text{ or } q = 1,2,3$$

From Equations (1.12) ~ (1.15), the relationship between piezoelectric charge/stress constant and piezoelectric constant can be written as

$$e_{ip} = d_{iq} c_{qp}^{E} \tag{1.16}$$

The relationship between dielectric permittivity at constant strain and at constant stress is given by

$$\varepsilon_{ij}^{T} - \varepsilon_{ij}^{S} = d_{iq} e_{jq} \tag{1.17}$$

In this study, we consider special symmetry case, assuming the piezoelectric material is a transversely isotropic material and the poling direction is along the 3-axis, which is also the axis of transverse isotropy. Stress, T , and strain , S , are the 6×1 vectors, electric field, E , is the 3×1 vector, piezoelectric stress/charge constant, e, and piezoelectric constant, d ,are the 3×6 matrices, compliance, s,is the 6×6 matrix at constant electric field, and dielectric permittivity, ε^{S} is the 3×3 matrix at constant strain The constitutive relations from Eqs (1.14) and (1.15) can be simplified to:

$$\begin{bmatrix} S_1 \\ S_2 \\ S_3 \\ S_4 \\ S_5 \\ S_6 \end{bmatrix} = \begin{bmatrix} s_{11}^E & s_{12}^E & s_{13}^E & 0 & 0 & 0 \\ s_{12}^E & s_{11}^E & s_{13}^E & 0 & 0 & 0 \\ s_{13}^E & s_{13}^E & s_{33}^E & 0 & 0 & 0 \\ 0 & 0 & 0 & s_{55}^E & 0 & 0 \\ 0 & 0 & 0 & 0 & s_{55}^E & 0 \\ 0 & 0 & 0 & 0 & 0 & s_{66}^E \end{bmatrix} \begin{bmatrix} T_1 \\ T_2 \\ T_3 \\ T_4 \\ T_5 \\ T_6 \end{bmatrix} + \begin{bmatrix} 0 & 0 & d_{31} \\ 0 & 0 & d_{31} \\ 0 & 0 & d_{33} \\ 0 & d_{15} & 0 \\ d_{15} & 0 & 0 \\ 0 & 0 & 0 \end{bmatrix} \begin{bmatrix} E_1 \\ E_2 \\ E_3 \end{bmatrix} \tag{1.18}$$

and

$$\begin{bmatrix} D_1 \\ D_2 \\ D_3 \end{bmatrix} = \begin{bmatrix} 0 & 0 & 0 & d_{15} & 0 \\ 0 & 0 & d_{15} & 0 & 0 \\ d_{31} & d_{31} & d_{33} & 0 & 0 \end{bmatrix} \begin{bmatrix} T_1 \\ T_2 \\ T_3 \\ T_4 \\ T_5 \\ T_6 \end{bmatrix} + \begin{bmatrix} \varepsilon_{11}^T & 0 & 0 \\ 0 & \varepsilon_{11}^T & 0 \\ 0 & 0 & \varepsilon_{33}^T \end{bmatrix} \begin{bmatrix} E_1 \\ E_2 \\ E_3 \end{bmatrix} \tag{1.19}$$

Therefore, we have 4+2+1=7 constitutive constants.

$$\begin{aligned} &c_{11} = c_{22},\ c_{23} = c_{13},\ c_{55} = c_{44},\ c_{66} = \frac{c_{11} - c_{12}}{2}, \\ &e_{24} = e_{15},\ e_{32} = e_{31},\ \varepsilon_{22} = \varepsilon_{11} \end{aligned} \tag{1.20}$$

1.4 Research objective

This study presents an analytical methodology for the study of a system that employs a fast-switched and capacitively shunted circuit. The switching topology induces modal responses that can be adaptively tuned via modulation of the duty cycle. The switching system modulates capacitance and is used to vary the effective stiffness. As a result, the strategy enables amplitude attenuation over a broader bandwidth. The system can be designed such that it provides a continuous range of operation by use of the switching subsystem. The present study introduces an enhanced averaging analysis of the switching shunt circuit for the piezoelectric structure and develops a predictive

mathematical model of the PWM switching system. This method is used to obtain an approximate solution for the transient response, by treating the time-variant systems as the time-invariant systems. Analysis and simulation of the averaged approximation is much faster and simpler than that of the original system. Figure 1-5 shows a schematic of the switching system.

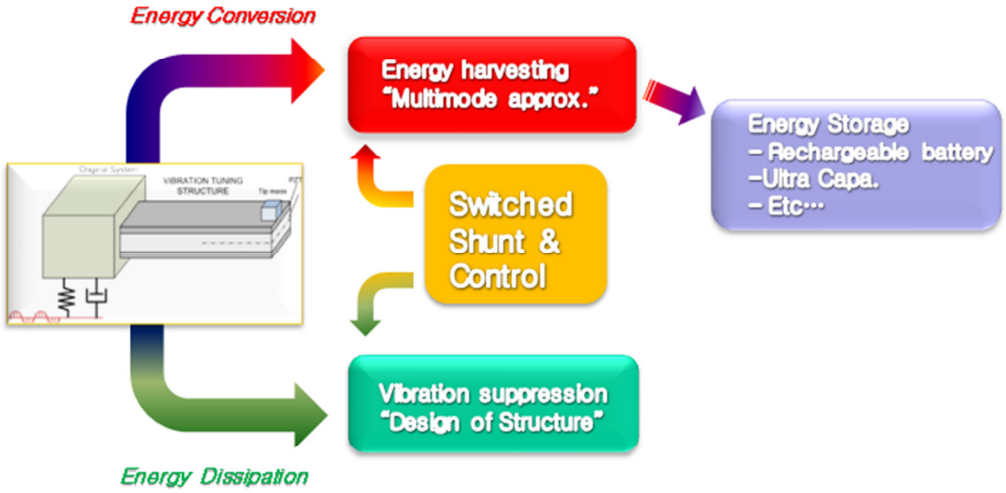

Figure 1-5. Conceptual switching system for vibration suppression/energy harvesting.

1.5 Chapter outline

Chapter 1 provides an overview of the primary goals in this research: (1) designing broadband piezoelectric structures via a semi-active switching strategy and (2) an enhanced averaging technique for approximating the original switching system.

Chapter 2 provides a comprehensive literature review of vibration suppressions and energy harvesting techniques. Specifically, passive and active control vibration suppression techniques using piezoelectric materials are presented. Novel energy harvesting systems using switching strategies are reviewed. An averaging method is derived from techniques arising in the study of power electronic systems based on PWM signals. which is advantageous to approximate solution associated with piecewise continuous systems.

Chapter 3 derives the weak form of the equations governing the PZT structures for numerical analysis. This derivation is based on the linear piezoelectricity and linear electrical networks. This chapter outlines the analysis method for derivation of equation of motion of structural dynamic systems.

Chapter 4 develops a capacitive shunt model for the PZT switching system. The discretized capacitance and the equivalent single-switch capacitance models are derived. A compact approximate solution is achieved using an averaging technique.

Chapter 5 presents results from an experiment to obtain wide bandwidth of resonant frequencies via the changes of duty ratio of PWM signal. The results are compared with an averaging method developed in Chapter 4.

The final chapter provides a brief summary of the research results presented in this dissertation and a discussion of potential future reseach.

1.6 Research contributions

A summary of the major findings in this research is given below:

The advantage of the switching system is that it enables continuous tuning of the electro-mechanical resonance frequency. This makes it possible for the power harvesting system to be optimally tuned to the structure (possible) in real time, therefore maximizing its power harvesting efficiency.

One of the strengths of this dissertation is the averaging analysis. The technique is really significant in that it allows for the analysis of a hybrid continuous/discrete system which is nonlinear in nature. The characteristics of the switching system are analyzed by an enhanced averaging method, which provides closed-form solution for the nonlinear system. There are good correlations between the analytical and experimental results in frequency responses.

In addition, a multi-ladder capacitance system, that can be used to reduce the vibration disturbance, is derived to reproduce earlier research. The analytical solution is compared with experimental results. Both of the results not only have a good agreement but also obtain broadband frequency shift as shown in the previous work.

Chapter 2

Literature review

The literature review summarizes previous research efforts in the areas of passive and active control vibration suppression techniques using piezoelectric materials, tuned vibration absorber with shunted electrical circuits, energy harvesting using shunt switching strategies, power electronic systems controlled by PWM signals and the approximate solution via averaging of piecewise continuous systems.

2.1 Passive/active techniques using piezoelectric materials for vibration attenuation

2.1.1 Passive damping techniques

Over the past decades, we have seen an increasing interest in the development of piezoelectric-based vibration suppression technique by integrating electrical shunt networks composed of resistors, inductors and capacitors. Similar to a tuned vibration

absorber, RLC networks electrically connected to the structure are designed to convert energy from structural vibrations into the electrical shunt system.

The piezoelectric effect, which is capable of converting the mechanical energy to the electrical energy or vice versa, causes current flow into the electrical circuit. In this manner, piezoelectric structures with shunt circuitry have been used to provide improved vibration attenuation over other passive control approaches [12, 13].

The basic principle of passive shunt systems introduced in these papers is shown in Figure 2-1. The capacitive piezostructure shown in Figure 2-1(a) is connected electrically to a resistive shunted network, therefore the coupled system behaves like a resistor in series with a capacitor system. While the converted energy from mechanical vibration in the piezostructure is stored in the capacitor, the resistance of the shunt system dissipates the energy. The damping effect of RC shunted piezeosystem results in the form of a frequency-dependent complex modulus and it behaves like viscoelasity. But, piezoelectric material properties distinguish from viscoelastic type materials. Piezoelectric materials have high stiff and insensitiveness to temperature, compared with viscoelastic material.

An electrical shunt network that also includes inductance,L,is shown in Figure 2-1(b). The combination of RLC components creates a second-order differential equation term which can be tuned to match the response of mechanical structure.

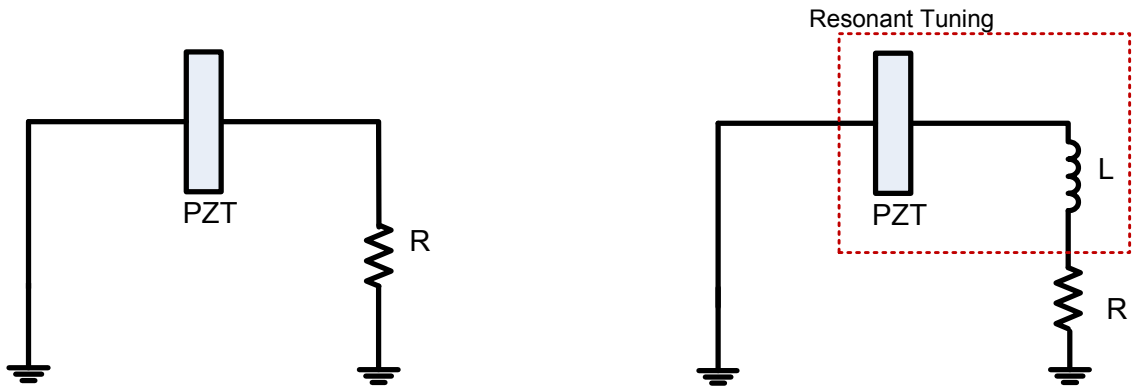

Figure 2-1. Piezostructure shunted with electrical networks: (a) Resistance only(left), (b) Resistance and inductance(right)

Forward [14] introduced passive damping techniques using piezoelectric materials for optical structures. This paper showed the feasibility of this type of passive damping system. Hagood *et al.* [12, 13] characterized impedance of shunt circuit coupled to piezoelectric materials. These papers proposed an analytical model to analyze the structural and electrical systems coupled via piezoelectric material. The papers derived effective mechanical impedance in order to optimize maximum values of damping ratio or energy transmission to the electrical loads. The expressions were represented in state-space form. The analytical solutions were derived for the simple example of a cantilever beam having bonded piezoelectric elements. The electrode faces or the piezoelectrics were connected to the electrical shunt network.

In order to improve damping due to resistive effects, Davis *et al.* [15] proposed using multiple piezoelectric elements for equal distribution of resistance. The modal strain energy approach was used to predict damping performance. The modal strain energy method expressed the damping effect in terms of the effective fraction of the modal strain energy in PZT, the effective material loss factor associated with the PZT electromechanical coupling coefficient, and the effective frequency shaping factor related to the shunt circuit dynamics. The analytical and experimental results showed that better damping over a wider range of frequencies.

Passive techniques are advantageous due to their robustness and stability. However, many passive techniques using electrical shunt system for vibration attenuation require high shunt impedances in order to have vibration attenuation over structure impedance [16].

2.1.2 Active control techniques

Historically speaking, active vibration attenuation has been developed in order to improve performance in comparison to passive methods. Active Noise Control [16] is a method for reducing unwanted noise with intentional interference and noise cancellation by introducing noise control source. Similar to active noise control technique, Active Structural Acoustic Control uses shakers, piezoelectric actuators (or patches) etc., as control inputs to a structural-acoustic system. Thus, this technique focuses on the transmission of sound and vibration energies radiating from periodically excited structures. PZT materials are often used for active control [16]. Wang *et al.* [17] studied the reduction of sounds radiated by the structure by using independently operated, multiple piezoelectric actuators. The quadratic optimal control technique has been widely used in this field because of its stability and robustness [18]. Experimental results have shown that piezoelectric actuators are quite effective at attenuating the structural vibrations at low frequency range. Fuller *et al.* [19] modeled a prototype of aircraft fuselage and conducted experiments to examine the effect of interior noise attenuation when PZT actuators are used.

PZT-based flexible composite materials have become more prevalent in the application of vibration suppression. The advantage of these composites include their physical flexibility which makes them easier to install onto arbitrary shape structures. They are also more durable than piezoceramic specimen which are relatively brittle. Sodano *et al.* [20] is a representative example of micro-fiber composite materials for vibration suppression.

2.2 Semi-active control of PZT

Passive and active piezo-shunt techniques, due to their stability and highly effective performance, have been widely developed in industry as well as research fields. The main driver behind the semi-active system is to combine advantages of both passive and active systems; the adaptability of active control system but with robustness and power efficiency of passive control system.

Passively tuned mechanical vibration absorbers are devices that are composed of a mass, spring and damp. Mechanical vibration absorbers were invented by Frahm in 1909. Since then, they have been further developed by Ormondroyd et al [21] and Den Hartog [22]. One disadvantage of these systems is that the bandwidth and center frequency of the tunable notch filter is fixed [23]. In practive, the vibration absorber natural frequency is precisely tuned to the natural frequency of the host structure such that it can absorb energy from the base structure. Unfortunately, in many real applications, the target resonant frequency is not known a priori and may not remain constant during operation of the system. Therefore, adjustable tuning strategies (or devices) are desired in order to obtain effective energy absorption. These efforts also form the basis of energy scavenging or harvesting by matching the energy transducer's natural frequency to the host's natural frequency [24, 25].

Due to their low power requirements, anecdotal and empirical evidence suggest that semi-active control systems can be attractive. Semi-active vibration attenuation systems are characterized by the synthesis of low power (usually switched) electronics that are intrinsically and physically integrated into an electromechanical system. One of the goals of semi-active control techniques for vibration suppression is to provide more broadband frequencies of operation over passive approaches and reduce the energy requirements often associated with fully active control approaches. Hence, there is an

emphasis on simple control methods that are implementable via energy-efficient switching strategies.

2.2.1 Self-tuning passive shunt systems combined with active control techniques

Many semi-active systems consist of passive shunt systems and active control systems with voltage or current sources. Advances in computing technology now enable real-time tracking of varying resonant frequencies. Hollkamp [26] studied a self-tuning shunt circuit to track a particular mode by adjusting inductance and resistance and tuning the resonant frequencies between the shunt circuit and the targeted structure. In this study, they suggested a simple method for multimodal vibration suppression. This capability was demonstrated experimentally using a cantilevered beam that hosts mounted multiple PZT patches arranged in parallel connection with a shunt circuit.

2.2.2 State-switching control strategies

Semi-active systems have been refined for decades to control vibration due to both periodic and random disturbances. Switching systems are broadly categorized as hybrid systems that combine both discrete and continuous dynamic characteristics. The mathematical framework of hybrid systems is studied in Witsenhausen [27]. Branicky [28], then, provided analytical tool for quantifying the stability of hybrid systems.

A state-switching system was developed by Larson *et al*. [29, 30] to obtain shifts in the system natural frequency using piezoelectric materials for an underwater acoustic transducer. This acoustic transducer resembles a passively tuned vibration absorber in that its resonant frequency must be tuned to the target frequency. This device is composed of a head mass, tail masses, an active spring, electronic switches and a control system. The active spring consists of piezoelectric material. The stiffness of piezoelectric materials can be varied by changing electrical boundary condition from an open circuit to

an short circuit condition. The piezoelectric material is connected by electronic switches to a stack of thin piezoelectric ceramic disks. If the target frequency is measured, the control system provides the signal to control the switches. This study demonstrated a 25 % resonant frequency shifts around 1kHz with experiment.

Clark [3, 31] and Corr *et al*. [32-34] developed vibration suppression techniques using a piezoceramic actuator coupled to a switching circuit. The synchronized switch controls the energy flow through the switching shunt network between the low short circuit and high open circuit stiffness. As a result, the targeted structure motion is attenuated because the shunt circuit absorbs the converted electrical energy obtained by transduction of mechanical energy.

2.2.3 Tunable capacitive shunt system

Semi-active switching system with a capacitive shunt circuit is typically used to vary the effective stiffness of transducers used for vibration attenuation, resulting in the vibration control over a broader bandwidth. This tunable vibration absorber employs a capacitive shunt circuit and discrete switch. The shift in center frequency and bandwithd can be measured by the ratio of the electrical impedance of the inherent piezoelectric capacitance to the electrical impedance of the external shunt circuit. This varies the resonant frequency of the piezostructural system as well as the modal damping [2].

Davis *et al*. [5] developed a tunable vibration absorber method based on electromechanical switches that control a capacitive ladder shunt circuit. This study was based on the work in Dosch *et al*. [35] which investigated an inertial vibration absorber. It was composed of an inertial mass or proof mass and piezoceramic disks that applied force. In order to obtain the electrical impedance change determined by a finite number of discrete capacitors, a pre-determined control signal corresponding to each resonant frequency was used to operate the electromechanical switches. The experimental results showed a 10 dB average improvement, in comparison to a passive system.

Charnegie *et al.* [36] studied a piezoelectric beam having an attached tuning layer. The piezostructural composite was coupled to capacitive shunt circuit for tuning resonant frequencies for energy harvesting.

2.2.4 Fast-switching control strategies

Recent research shows that by introducing a fast-switching strategy a continuous range of natural frequencies can be obtained using a switched shunt circuit. An analytical methodology for fast-switching absorber has been derived in [7]. They have derived an approach for the averaging method to analyze complex switching systems which can adjust the tuning frequency continuously.

Kim *et al*. [25] [37] demonstrated a vibration absorber controlled by a fast-switching topology integrated into an electromechanical system. In this study, they showed that the stiffness of a piezostructure can be varied continuously by controlling the PWM signal that drives a MOSFET switch, which is known to be energy-efficient.

Domme [38] applied a switching control technique to an electromagnetic device for maximizing energy harvesting efficiency.

2.3 Energy harvesting

By their nature, vibration absorbers dissipate energy. Energy harvesting, as opposed to the vibration absorbers, often employ electrical shunt systems across piezostructure to capture and store energy. These circuits have some characteristics of vibration absorbing in that they collect strain energy of the structure. Sometimes, this effect is called shunt damping. Electrical shunt circuits always induce some damping into the structure, which decreases the amount of vibration. On the other hand, the electric loads yield energy that is extracted from piezoelectric generators. Hence, the energy

moves from the structure into the electrical shunt network and is either dissipated as heat or stored in a circuit.

2.3.1 Energy harvesting generators

Many research studies have focused on modeling and analysis of energy harvesting designs based on various piezoelectric structures [39-43]. For example, there has been increasing interest in cantilever beams with proof mass or tip mass that are bonded to layers of piezoelectric materials for MEMS/Micro-scale applications [24].

Roundy *et al*. [44, 45] studied vibrations as a power source for wireless sensor nodes. The mechanical model is a cantilever beam bonded to piezoelectric patches. The main idea of this study is to exploit the analogies between structural and electrical components to convert energy optimally from the mechanical to the electrical system. The maximum generated power is a function of how the damping is matched between the electrical and mechanical systems along with the resonant frequency. The transducer is optimized to collect energy within a volume of the size of 1 cm^3. The experimental results in the paper show that the piezoelectric converter achieves 200uW/cm^3 power densities from input base acceleration having magnitude of 2.25m/s^2 at 120 Hz.

Sodano *et al*. [46-48] studied cantilever beam piezoelectric generators with various surface-mounted materials such as piezoceramic and micro-fiber composite. They demonstrated that the palm-sized piezoelectric structure was able to charge a 40mAh disk battery around one hour. In this experiment, a simple rectifier circuit consisting of a full bridge diode and a capacitor was used. Their analytical model took into account the damping effect due to electrical impedance and demonstrated the power generation efficiency of the shunt circuit.

In duToit *et al.* [39, 49], the authors focused on analytically predicting the electrical power versus frequency ratios when electrical loads on the generated power from a piezoelectric generator were varied.

Erturk *et al*. [50] derived the analytical solutions for a cantilever beam undergoing transverse motions as well as small rotations at the driven base for energy harvesting. Also, he extended his research using multi-resonant frequencies by devising an L-shaped PZT-type energy harvester[51].

Elvin *et al*. [52] suggested a method to analyze electro-mechanical structures that are described in two physically different domains by combining models obtained from the commercial software. They approximated the solution by performing simulations that alternate FEM and circuit simulation tools. They investigated output voltages across a simple electrical load that is coupled to a structure constructed from beam and plate models. The authors have validated their simulation strategy for PZT structures by hand and via numerical experiments.

2.3.2 Energy harvesting circuitry using switching topology

One of the key aspects of energy harvesting is how to extract energy from a shunted electrical network. As depicted in Figure 2-2, typical energy harvesting circuit consists of a voltage rectifier, an energy conditioner such as DC/DC converter and an energy storage device. One design consideration determines how to construct high efficiency energy conversion devices that minimize conversion loss. For this reason, the use of switching systems has been introduced to decrease the power loss and increase the power efficiency of the device.

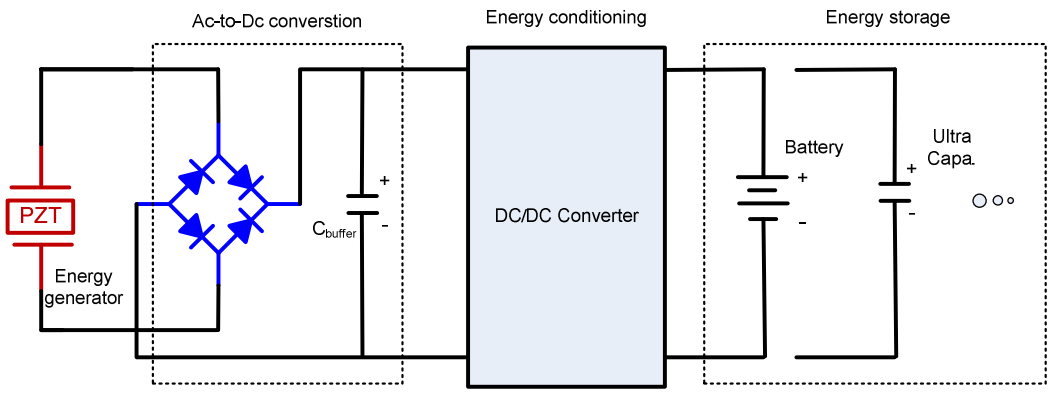

Figure 2-2. General diagram of a PZT energy harvesting circuit consisting of ac-to-dc rectifier, energy condition and energy storage devices.

The progress in the development of the semi-active vibration control method has been closely related to the derivation of the switching strategies. Ottman *et al.* developed a pulse-width modulated switching converter system to maximize power transfer from a piezoelectric system to an energy storage device, which can be either a capacitive storage or a battery [53, 54]. According to the authors, the use of the switching system increased the power efficiency by 400 %. This power electronic topology consumes very little energy. Theoretically no power loss at the switch. The switching strategy maximizes power transfer at a certain range of the duty ratio. However, it requires some amount of additional power for operating the switching and feedback controller, which is the main souce of power loss for a switching circuit.

Lesieutre *et al.* [6] proposed a two-mode energy harvesting circuit to reduce the power requirements for running an adaptive switching control. The two-mode energy harvester not only introduces classical energy storage but also delivers power to energy storage via a DC/DC converter. The DC/DC converter delivers energy to the storage device at an optimal design condition. For example, the battery is directly charged by a low-level voltage, and the adaptive switching controller is operated to increase the efficiency of charging the battery at high-level voltage conditions.

Another set of advanced energy harvesters using switching for piezoelectric structures is presented by Lallart *et al*. [55, 56]. This technique is designed to maximize electrical power transfer by fine-tuning synchronized switching. Figure 2-3 illustrates one example of the power extracting circuits employed to maximize power transfer with two synchronous switches. This strategy is based on impedance matching of the piezoelectric materials and the power adaptation via a DC/DC converter. The overall technique is known as the zero power loss in the ideal case. In this circuit, the component values, source and switching frequencies are arbitrarily determined to have the switches opened and closed at the positive and negative peaks. In this circuit, S_1 is closed until the capacitor C_{int} is fully charged when the voltage generated across the PZT has reached a peak. As soon as the capacitor C_{int} is charged fully and the switch S_1 is open, the switch S_2 is closed and power flows from C_{int} to an electrical load or energy storage device. Therefore, this power electronic circuit is switched to achieve the efficient energy transfer in that the maximum power is obtained via the impedance matching of piezoelectric materials in the 1st stage and a buck-boost converter.. The authors show that the efficiency increases by more than 500%.

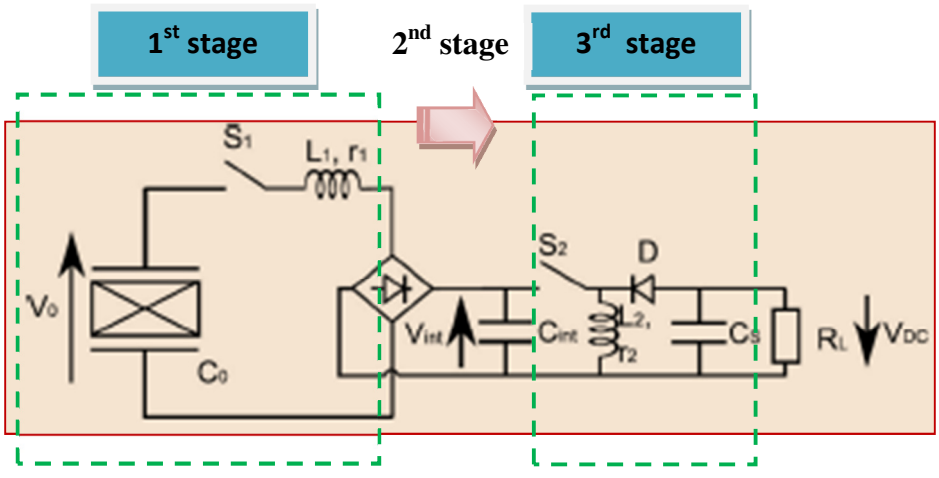

Figure 2-3. Power extraction associated with synchronized switching control [55]. 1st stage: PZT impedance matching, 2nd stage: AC-DC conversion, 3rd stage: Power conditioning.

2.4 State-space averaging method for analyzing (averaging methods) fast-switching dynamic systems

Numerical approximation of a time variant system can be more challenging than that for a continuous system. For example, the analysis of switching systems must account for both the continuous motion of the dynamics and the discontinuous states of the switching signals. In order to analyze switching control systems, one technique transforms the discontinuous system model into a continuous model. One approach to achieve this goal is the averaging method, which is useful for the linearization of certain piecewise continuous or nonlinear systems. In the power electronics and dynamic system fields, averaging methods have been developed as approximation techniques for studying nonlinear dynamics. In essence, averaging methods replace discontinuities in the original model with smooth and continuously changing functions. State space averaging techniques have been applied to the analysis of switching converters in power electronics [57] and also the dynamic behavior of general nonlinear systems [58, 59].

Middlebrook *et al.* [60] suggested a new approach when he developed a state-space averaging technique. His approach has proven to be an efficient and popular design tool for the analysis of small signal behavior of PWM converters. In his analysis, it is assumed that the complicated switching system can be represented in terms of a set of linear independent state equations. It is worth note that each state equation is obtained by averaging of multiple configurations indexed by the duty ratio of the switching converter [61].

Motivated by the work by Middlebrook *et al*. [60], Witulski *et al*. [62]extended the state space modeling technique to represent resonant switch converters, which are

generally operated at lower switching frequency than PWM converters. The resonant switching technique is used since more energy loss may occur as the switching frequencies increase [63]. Due to the operation at low switching frequencies, the averaging method based on the small signal assumption is not valid any longer: the high switching frequency term must be filtered through the LC circuit. In this study, the investigators suggested a new method where the state space equations of the original system were represented by two separate expressions corresponding to the steady state and switching components.

Krein *et al*. [64, 65] focused on a large signal nonlinear averaged model by applying the Krylov, Bogoliubov and Miltropolsky (KBM) method. This technique allows for a generalization of the averaging used in fast switching power converters to separate the complicated discontinuous system into linear approximations of the converter. The KBM method is used to establish the approximate solution of the system by varying a small parameter, ϵ, and expanding approximations in terms of a power series and the small parameter.

Chapter 3

Linear analysis of piezostructures

3.1 Introduction

In this chapter, we derive linear governing equations of the PZT composite structures. This derivation is based on the equations of linear piezoelectricity and linear electrical networks.

3.2 Linear piezostructural system modeling

3.2.1 Piezostructure continuum modeling: Hamilton's extended principle

Active composite structures have complex dynamic characteristics involving both strain energy as well as electrical energy. Hamilton's extended principle (HEP), based on principle of variational calculus is well suited in this case for finding the equations of motions of these complex systems [10, 12, 66, 67]. This formulation establishes the equations of motion by integrating the motion of the system between times t_1 and t_2.

The mathematical statement of HEP is written as the integral form of virtual change of the Lagrangian, L, and virtual work, δW_{nc}, performed by non-conservative forces over time interval t_1 and t_2,

$$H \triangleq \delta \int_{t_1}^{t_2} L dt + \int_{t_1}^{t_2} \delta W dt = 0 \tag{3.1}$$

where

i) $L = \mathrm{T} - \mathrm{V}$, T is the total kinetic energy and V is the total potential energy,

ii) δW_{nc} is the virtual work including conservative and non-conservative forces, and

iii) The variation of displacement vector of $\delta \mathbf{u}(\cdot, t)$ is zero at $t = t_1$ and $t = t_2$.

The kinetic energy, T, of the composite structure having bonded PZT patches over domain, Ω, is written as

$$\mathrm{T} = \frac{1}{2} \int_{\Omega} \rho(\mathbf{x}) \dot{\mathbf{u}}(\mathbf{x}, t)^T \dot{\mathbf{u}}(\mathbf{x}, t) d\Omega \tag{3.2}$$

where $\mathbf{u}(\mathbf{x}, t)$ is the vector of mechanical displacement at the location $\mathbf{x} \in \Omega$. The composite density, $\rho(\mathbf{x})$, is given by

$$\rho(\mathbf{x}) = \rho_s(\mathbf{x}) + \sum_{i=1}^{N} \chi_{pi}(\mathbf{x}) \rho_p(\mathbf{x})$$

where the $\chi_{pi}(\mathbf{x})$ is the characteristic function of the i^{th} PZT patch with domain Ω_{pi},

$$\chi_{pi}(\mathbf{x}) = \begin{cases} 1, & \mathbf{x} \in \Omega_{pi}, \quad \text{electrode regions} \\ 0, & \mathbf{x} \notin \Omega_{pi} \end{cases}$$

Assuming that the variation operator, δ, and the differentiation operator, $\frac{d}{dt}$, commute, the integration by parts of the total kinetic energy over the time interval from t_1 to t_2 yields,

$$\begin{aligned} \int_{t_1}^{t_2} \delta \mathrm{T} dt &= \int_{t_1}^{t_2} \left\{ \int_\Omega \rho(\mathbf{x}) \delta \dot{\mathbf{u}}^T \dot{\mathbf{u}} d\Omega \right\} dt \\ &= \int_\Omega \left\{ \rho(\mathbf{x}) \delta \mathbf{u}^T \cdot \dot{\mathbf{u}} \Big|_{t_1}^{t_2} \right\} d\Omega - \int_{t_1}^{t_2} \left\{ \int_\Omega \rho(\mathbf{x}) \delta \mathbf{u}^T \cdot \ddot{\mathbf{u}} d\Omega \right\} dt \\ &= -\int_{t_1}^{t_2} \left\{ \int_\Omega \rho(\mathbf{x}) \delta \mathbf{u}^T \cdot \ddot{\mathbf{u}} d\Omega \right\} dt \end{aligned} \tag{3.3}$$

The potential energy, V, for the composite piezostructure is written as,

$$\begin{aligned} \mathrm{V} &= \frac{1}{2} \int_\Omega \mathbf{S}^T \mathbf{T} d\Omega \\ &= \frac{1}{2} \int_{\Omega_s} \mathbf{S}^T \mathbf{T} d\Omega + \frac{1}{2} \int_{\Omega_p} \mathbf{S}^T \mathbf{T} d\Omega \end{aligned} \tag{3.4}$$

where Ω_s is the host structure) regions. Substituting Equation (1.1) into Equation (3.4), we have

$$\mathrm{V} = \frac{1}{2} \int_{\Omega_s} \mathbf{S}^T \mathbf{c}_\mathbf{s} \mathbf{S} d\Omega + \frac{1}{2} \int_{\Omega_p} \mathbf{S}^T \mathbf{c}^\mathbf{E} \mathbf{S} d\Omega - \frac{1}{2} \int_{\Omega_p} \mathbf{S}^T \mathbf{e}^T \mathbf{E} d\Omega \tag{3.5}$$

In a similar manner to Equation (3.3), the variation of the potential energy is

$$\delta \mathrm{V} = \int_{\Omega_s} \delta \mathbf{S}^T \mathbf{c}_\mathbf{s} \mathbf{S} d\Omega + \int_{\Omega_p} \delta \mathbf{S}^T \mathbf{c}^\mathbf{E} \mathbf{S} d\Omega - \frac{1}{2} \int_{\Omega_p} \delta \mathbf{E}^T \mathbf{e} \mathbf{S} d\Omega - \frac{1}{2} \int_{\Omega_p} \mathbf{E}^T \mathbf{e} \delta \mathbf{S} d\Omega \tag{3.6}$$

The electrical energy is given by definition as

$$\begin{aligned} W_e &= \frac{1}{2} \int_{\Omega_p} \mathbf{E}^T \mathbf{D} d\Omega \\ &= \frac{1}{2} \int_{\Omega_p} \mathbf{E}^T \mathbf{e} \mathbf{S} d\Omega + \frac{1}{2} \int_{\Omega_p} \mathbf{E}^T \boldsymbol{\varepsilon}^\mathbf{S} \mathbf{E} d\Omega \end{aligned} \tag{3.7}$$

Variation of electrical energy is calculated to be

$$\delta W_e = \frac{1}{2} \int_{\Omega_p} \delta \mathbf{E}^T \mathbf{e} \mathbf{S} d\Omega + \frac{1}{2} \int_{\Omega_p} \mathbf{E}^T \mathbf{e} \delta \mathbf{S} d\Omega + \int_{\Omega_p} \delta \mathbf{E}^T \boldsymbol{\varepsilon}^\mathbf{S} \mathbf{E} d\Omega \tag{3.8}$$

The non-conservative work term includes contributions due to extend electrical and mechanical loads. The virtual work is expressed as

$$\delta W_{nc} = \sum_{i=1}^{N_f} \delta \mathbf{u}(\mathbf{x}_i, t) \mathbf{f}(\mathbf{x}_i, t) - \sum_{j=1}^{N_q} \delta \boldsymbol{\varphi}(\mathbf{x}_j, t) \mathbf{q}_j \tag{3.9}$$

where discrete applied loads $\mathbf{f}(\mathbf{x}_i, t)$ concentrated at position $\mathbf{x}_i$, and imposed charges $\mathbf{q}_j$ are imposed at $\mathbf{x}_j$. The Hamiltonian formulation for the generalized equations of motion can be described by substituting Equations (3.3) ~ (3.9) into Equation (3.1),

$$
\begin{aligned}
H &= \int_{t_1}^{t_2} \left[\delta(\mathrm{T} - \mathrm{V}) + \delta W_e + \delta W_{nc} \right] dt \\
&= \int_{t_1}^{t_2} \Bigg[-\int_{\Omega} \rho(x) \delta \mathbf{u}^T \ddot{\mathbf{u}} d\Omega - \int_{\Omega_s} \delta \mathbf{S}^T \mathbf{c}_\mathbf{s} \mathbf{S} d\Omega - \int_{\Omega_p} \delta \mathbf{S}^T \mathbf{c}^\mathbf{E} \mathbf{S} d\Omega + \int_{\Omega_p} \delta \mathbf{E}^T \mathbf{e} \mathbf{S} d\Omega \\
&\quad + \int_{\Omega_p} \mathbf{E}^T \mathbf{e} \delta \mathbf{S} d\Omega + \int_{\Omega_p} \delta \mathbf{E}^T \boldsymbol{\varepsilon}^\mathbf{S} \mathbf{E} d\Omega + \sum_{i=1}^{N_f} \delta \mathbf{u}(\mathbf{x}_i, t) \mathbf{f}(x_i, t) - \sum_{j=1}^{N_q} \delta \boldsymbol{\varphi}(\mathbf{x}_j, t) \mathbf{q}_j \Bigg] dt
\end{aligned}
\tag{3.10}
$$

3.3 Distributed parameter modeling of cantilever beam mounted with PZT

In this section, a symmetric bimorph, cantilevered structure is considered. This piezostructure is depicted in Figure 3-1. The two piezoelectric layers are of uniform thickness. The adhesion to the substrate shim metal is assumed to be perfect. The voltage varies linearly along the layer thickness, that is, along the z axis. In other words we assume a 31 mode of operation, where $E_1 = E_2 = 0$.

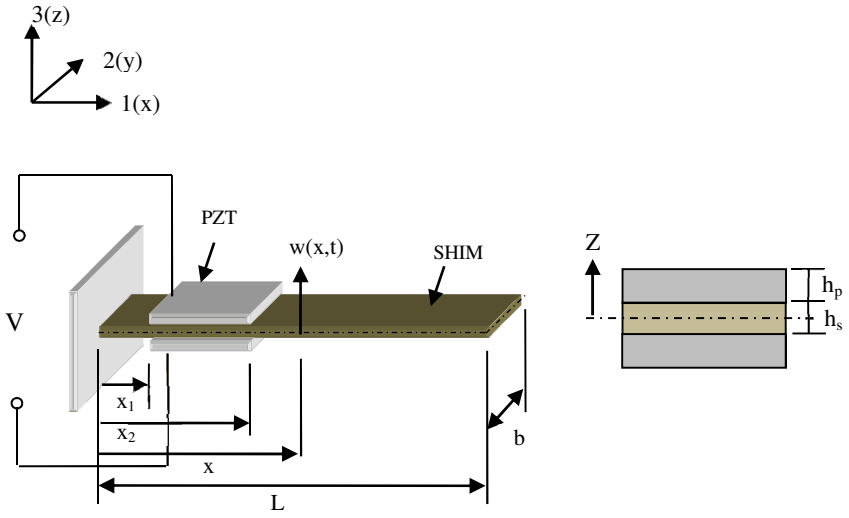

Figure 3-1. The bimorph-cantilevered structure symmetrically covered with piezoelectric layers. The region x∈[x_1,x_2] defined the range with the surface-mounted patch.

3.3.1 Strain-displacement and electrical field-potential relationships

It is generally difficult to find closed form solutions to the partial differential equations governing the dynamics of complex composite structures. However, one can obtain solutions by applying a modal decomposition method where the dynamics of the structure is described in terms of a superposition of independent vibration modes. Thus, the set of partial differential equations are recast as a set of ordinary differential equations. The derivation begins with a modal expansion of the transverse displacement, $\mathbf{w}(x,t)$, and the electrical potential, $\boldsymbol{\varphi}(z,t)$;

$$\mathbf{w}(x,t) = \boldsymbol{\psi}_r(x)\mathbf{r}(t) = \sum_i \psi_{ri}(x) r_i(t) \tag{3.11}$$

$$\boldsymbol{\varphi}(z,t) = \boldsymbol{\psi}_v(z)\mathbf{V}(t) = \sum_i \psi_{vi}(z) V_i(t) \tag{3.12}$$

where $\boldsymbol{\psi}_r$ is the assumed mode shape, $\boldsymbol{\psi}_v$ is the vector of assumed mode shapes of electrical field, $\mathbf{r}(t)$ is a time-dependant modal amplitude, and subscript i is the i^{th} mode and $\mathbf{V}(t)$ is the vector of the electrical potential difference between the final and initial positions. Note that bold and italic denote a matrix and a component respectively. That is, we have $\boldsymbol{\psi}_r^T = \{\psi_{r1}, \psi_{r2}, \cdots\}$ for example.

The standard differential operators, L_u and L_φ, are introduced as shown below. Strain-displacement and electrical field-potential relationships are written respectively as,

$$\mathbf{S} \equiv L_u \mathbf{w}(x,t) = \mathbf{N}_\mathbf{r}(x)\mathbf{r}(t) = \sum_i N_{ri}(x) r_i(t) \tag{3.13}$$

$$\mathbf{E} \equiv L_\varphi \boldsymbol{\varphi}(z,t) = \mathbf{N}_\mathbf{v}(z)\mathbf{V}(t) = \sum_i N_{vi}(z) V_i(t) \tag{3.14}$$

where the displacement vector $\mathbf{N}_\mathbf{r}(x)$, and electrical voltage vector $\mathbf{N}_\mathbf{v}(z)$, are defined as

$$\mathbf{N}_\mathbf{r}(x) = L_u \boldsymbol{\psi}_\mathbf{r}(x)$$
$$\mathbf{N}_\mathbf{v}(z) \equiv L_\varphi \boldsymbol{\psi}_\mathbf{v}(z) = -\nabla \boldsymbol{\psi}_\mathbf{v}(z)$$

In the case of the simple beam model that satisfies Euler-Bernoulli assumption, the strain is along the x axis. The strain distribution is given by

$$S_{11} = L_u w(x,t) = -z \frac{\partial^2 w(x,t)}{\partial x^2} \tag{3.15}$$

Therefore, the displacement vector, $\mathbf{N}_\mathbf{r}(x)$

$$\mathbf{N}_\mathbf{r}(x) = -z \frac{\partial^2 \boldsymbol{\psi}_\mathbf{r}(x)}{\partial x^2} \tag{3.16}$$

3.3.2 Voltage over the layers

In this section, the voltage distribution will be derived over the piezoelectric layer polarized along, z axis which corresponds to the 31 mode of operation. The voltage difference between electrodes depends on the electrical connection. Two examples are shown Figure 3-2: a parallel connection and a series connection. The illustration in Figure 3-2(a) depicts the simple model of parallel connection, where the piezoelectric layers have their poling direction along the positive z-axis. The patches undergo opposite bending strains above and below the neutral axis, one is extension, the other contraction,

but have same strain magnitudes. The result is that the same voltage sign is measured at the outer and inner surfaces respectively. Three wires are required: two for the outer surfaces and one for the inter surface. The total voltage is the same as that of an individual layer. But, the total current is the sum of currents from the individual layers.

A series connection is illustrated with Figure 3-2(b). The total voltage is double that of the individual voltage, while the total current is same as that of each layer.

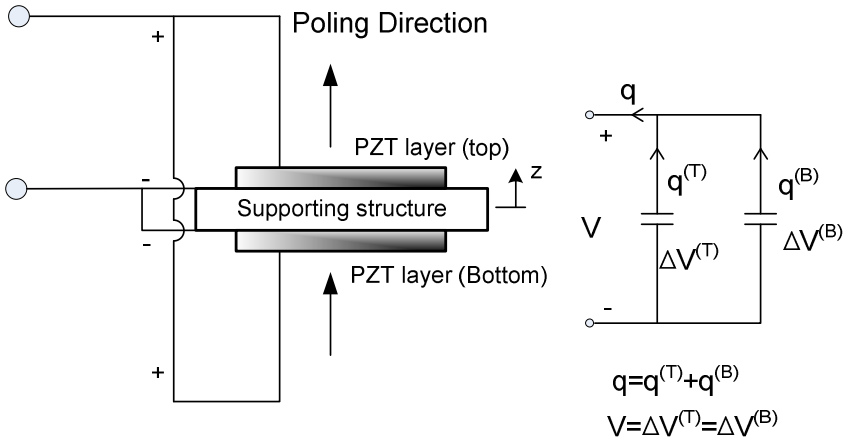

(a) Parallel connection

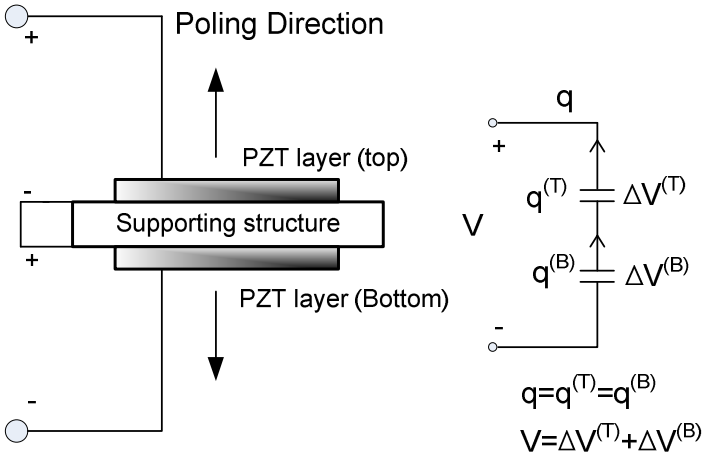

(b) Series connection

Figure 3-2. Electrical wiring for surface-mounted PZT patches of piezostructure.

(a) Voltage connection in parallel

As mentioned in the previous section, the electric field generated is a function of the deflection of structure. It is assumed that: (1) the voltage difference through thickness of PZT varies linearly along z-axis and is constant along the x and y axes, and (2) the electric field is parallel to the direction of poling direction and is perpendicular to the direction of extension and contraction of piezoelectric layers during bending motion.

Suppose that the voltage difference, $\Delta V^{(T)}$, between the upper and the lower surfaces of the top layer is

$$\Delta V^{(T)}(t) \equiv V^{(T)+}(t) - V^{(T)-}(t) \tag{3.17}$$

Note that $V^{(T)+}(t)$ is defined to be equal to or greater than $V^{(T)-}(t)$. Therefore, the voltage over the top layer, $V^{(T)}(z,t)$, can be written as a linear function of z

$$\begin{aligned} V^{(T)}(z,t) &= \frac{V^{(T)+}(t) - V^{(T)-}(t)}{h_p + h_s/2 - h_s/2}\left(z - h_s/2\right) + V^{(T)-}(t) \\ &= \frac{\Delta V^{(T)}(t)}{h_p}\left(z - h_s/2\right) + V^{(T)-}(t) \end{aligned}$$

Similar to the top layer, a linear variation of the voltage over the bottom layer, $V^{(B)}(z,t)$, can be written as a linear function of z

$$\begin{aligned} V^{(B)}(z,t) &= \frac{V^{(B)+}(t) - V^{(B)-}(t)}{-\left(h_p + h_s/2\right) + h_s/2}\left(z + h_s/2\right) + V^{(B)-}(t) \\ &= -\frac{\Delta V^{(B)}}{h_p}\left(z + h_s/2\right) + V^{(B)-}(t) \end{aligned} \tag{3.18}$$

where $\Delta V^{(B)}(t) = V^{(B)+}(t) - V^{(B)-}(t)$.

Assuming that the bimorph structure is perfectly symmetric, the voltages generated in PZT patches are the same;

$$\varphi_3(z,t) = \boldsymbol{\psi}_v(z)\mathbf{V}(t) = \begin{cases} dV^{(T)} = V^{(T)-}(t) - V^{(T)}(z,t) = -\dfrac{\Delta V^{(T)}(t)}{h_p}\left(z - h_s/2\right) \\ dV^{(B)} = V^{(B)-}(t) - V^{(B)}(z,t) = \dfrac{\Delta V^{(B)}(t)}{h_p}\left(z + h_s/2\right) \end{cases} \tag{3.19}$$

Thus, electrical field along z-axis is given by the piecewise constant expression

$$E_3 \equiv -\nabla\varphi_3 = \mathbf{N}_{\mathrm{v}}(z)\mathbf{V}(t) = \begin{cases} \dfrac{\Delta V^{(T)}(t)}{h_p}, & \text{on the top layer} \\ -\dfrac{\Delta V^{(B)}(t)}{h_p}, & \text{on the bottom layer} \end{cases} \tag{3.20}$$

The voltage is $V(t) = \Delta V^{(T)} = \Delta V^{(B)}$

From Kirchhoff's current law, the total current is $\dot{q} = \dot{q}^{(T)} + \dot{q}^{(B)}$.

(b) Voltage connection in serial

When the patches are connected in serial, the voltage over the top layer can be written as a linear function of z

$$\begin{aligned} V^{(T)}(z,t) &= \frac{V^{(T)+}(t) - V^{(T)-}(t)}{h_p + h_s/2 - h_s/2}\left(z - h_s/2\right) + V^{(T)-}(t) \\ &= \frac{\Delta V^{(T)}(t)}{h_p}\left(z - h_s/2\right) + V^{(T)-}(t) \end{aligned} \tag{3.21}$$

Similar to the top layer, the voltage over bottom layer can be written as a linear function of z

$$\begin{aligned} V^{(B)}(z,t) &= \frac{V^{(B)+}(t)-V^{(B)-}(t)}{-h_s/2-\left\{-\left(h_p+h_s/2\right)\right\}}\left(z+h_s/2\right)+V^{(B)-}(t) \\ &= \frac{\Delta V^{(B)}}{h_p}\left(z+h_s/2\right)+V^{(B)-}(t) \end{aligned} \tag{3.22}$$

where $\Delta V^{(B)}(t)=V^{(B)+}(t)-V^{(B)-}(t)$.

Assuming that the bimorph structure is perfectly symmetry, the voltages generated in PZT patches are the same;

$$\varphi_3(z,t)=\boldsymbol{\psi}_v(z)\mathbf{V}(t)=\begin{cases} dV^{(T)}=V^{(T)-}(t)-V^{(T)}(z,t)=-\dfrac{\Delta V^{(T)}(t)}{h_p}\left(z-h_s/2\right) \\ dV^{(B)}=V^{(B)-}(t)-V^{(B)}(z,t)=-\dfrac{\Delta V^{(B)}(t)}{h_p}\left(z+h_s/2\right) \end{cases} \tag{3.23}$$

Thus, electrical field along z-axis is

$$E_3\equiv-\nabla\varphi_3=\mathbf{N}_{\mathrm{v}}(z)\mathbf{V}(t)=\begin{cases} \dfrac{\Delta V^{(T)}(t)}{h_p}, & \text{on the top layer} \\ \dfrac{\Delta V^{(B)}(t)}{h_p}, & \text{on the bottom layer} \end{cases} \tag{3.24}$$

In contrast to the parallel connection case, the total voltage in the series connection is

$$V(t)=\Delta V^{(T)}(t)+\Delta V^{(B)}(t) \tag{3.25}$$

and the total current is

$$\dot{q} = \dot{q}^{(T)} = \dot{q}^{(B)} . \tag{3.26}$$

3.4 Strong form equations

The equations of motion for the electromechanical composite structure are now presented. The kinetic energy and its variation of the piezostructure are

$$\mathrm{T} = \int_0^L \rho_\ell(x)\dot{w}(x,t)^2 dx \tag{3.27}$$

$$\int_{t_1}^{t_2} \delta \mathrm{T} dt = -\int_{t_1}^{t_2} \left\{ \int_0^L \rho_\ell(x)\delta w(x,t)\cdot \ddot{w}(x,t) dx \right\} dt \tag{3.28}$$

where $\rho_\ell(x) = \rho(x)A(x)$ is the linear density of PZT structure. From Equation (3.6), the variation of potential energy and electrical work for cantilever beam structures is

$$\begin{aligned} \delta \mathrm{V} - \delta W_e = & \int_0^L EI(x) w_{xx}\delta w_{xx} dx + \int_0^L \chi_p(x) e_{31} Q_p w_{xx} \delta E_3 dx + \int_0^L \chi_p(x)\delta w_{xx} Q_p e_{31} E_3 dx \\ & - \int_0^L \chi_p(x)\left(bh_p\right)\varepsilon_{33}^S E_3 \delta E_3 dx \end{aligned} \tag{3.29}$$

Recalling that $E_3 = -\dfrac{V(t)}{h_p}$, the integration can be calculated as,

$$\begin{aligned} \delta \mathrm{V} - \delta W_e = & \int_0^L EI(x) w_{xx}\delta w_{xx} dx - \int_0^L \chi_p(x) e_{31} Q_p w_{xx} \frac{\delta V(t)}{h_p} dx - \int_0^L \chi_p(x)\delta w_{xx} Q_p e_{31} \frac{V(t)}{h_p} dx \\ & - \int_0^L \chi_p(x)\left(bh_p\right)\varepsilon_{33}^S \frac{V(t)\delta V(t)}{h_p} dx \end{aligned} \tag{3.30}$$

where $Q_p = \int_{A_p} z dA$, $EI(x) = c_s I^{(S)} + \chi_p(x) c_{11}^E I^{(P)}$ and $(\ )_{xx} = \dfrac{\partial^2}{\partial x^2}$. Note that c_s is the Young's modulus of substrate, and $I^{(S)}$ and $I^{(P)}$ are the 2nd area moment of inertia of the substrate and the piezostructure, respectively. Performing integration by parts twice with respect to x yields

$$\begin{aligned}\delta \mathrm{V} - \delta W_e = & \int_0^L \left(EI(x) w_{xx}\right)_{xx} \delta w dx + \int_0^L \chi_p(x) e_{31} Q_p w_{xx} \delta E_3 dx \\ & + \int_0^L \left(\chi_p(x) e_{31} Q_p E_3\right)_{xx} \delta w dx - \int_0^L \chi_p(x) \left(b h_p\right) \varepsilon_{33}^S E_3 \delta E_3 dx + EI(x) w_{xx} \delta w_x \Big|_0^L \\ & - \left(EI(x) w_{xx}\right)_x \delta w \Big|_0^L + \chi_p(x) e_{31} E_3 Q_p \delta w_x \Big|_0^L - \left(\chi_p(x) e_{31} E_3 Q_p\right)_x \delta w \Big|_0^L\end{aligned} \quad (3.31)$$

Inserting the variation of the kinetic energy (3.28), the variation of the potential energy, the virtual electrical work (3.31), and the virtual non-conservative work (3.9), the Hamiltonian formulation yields

$$\begin{aligned}\delta H = & \int_{t_1}^{t_2} \left[\delta\left(\mathrm{T} - \mathrm{V}\right) + \delta W_e + \delta W_{nc}\right] dt \\ = & \int_{t_1}^{t_2} \left[\int_0^L \left(-\rho \ddot{w}(x,t) + V(t) \frac{\partial^2}{\partial x^2} B_p(x) - \left(EI(x) w_{xx}(x,t)\right)_{xx} + f(x_i,t) \right) \delta w dx \right] dt \\ & + \int_{t_1}^{t_2} \delta V(t) \left[C_p^S V(t) + \int_0^L B_p(x) w_{xx}(x,t) dx - \sum_j^{N_q} \psi_{vj}(z) q_j \right] dt \\ & \underbrace{- \int_{t_1}^{t_2} \left[\left\{ EI(x) w_{xx} + \chi_p(x) e_{31} Q_p E_3 \right\} \delta w_x \Big|_0^L \right] dt + \int_{t_1}^{t_2} \left[\left\{ \left(EI(x) w_{xx}\right)_x + \left(\chi_p(x) e_{31} Q_p E_3\right)_x \right\} \delta w \Big|_0^L \right] dt}_{B.C.} = 0\end{aligned} \quad (3.32)$$

The above functional must be equal to zero for all admissible variations δw and δV. We conclude that the strong form governing equations must hold. One is referred to as the piezoelectric actuator equation and the other is known as the sensor equation;

$$\rho_\ell(x)\ddot{w} + \left(EI(x)w_{xx}\right)_{xx} = \frac{\partial^2}{\partial x^2}\left(B_p(x)V(t)\right) + f(x,t), \qquad 0 < x < L \tag{3.33}$$

$$q = \sum_{j=1}^{N_q} \psi_{vj} q_j = C_p^S V(t) + \int_0^L B_p(x) w_{xx} dx \tag{3.34}$$

If the proportional damping terms are considered [10], the strong form equation of the actuator is

$$\rho_\ell(x)\ddot{w} + \gamma\frac{\partial w}{\partial t} + \frac{\partial^2}{\partial x^2}\left(EI\frac{\partial^2 w}{\partial x^2}\right) = V(t)\frac{\partial^2}{\partial x^2}B_p(x) + f(x,t), \qquad 0 < x < L \tag{3.35}$$

The coefficients C_p^S, B_p and Q_p are given by

$$C_p^S = \varepsilon_{33}^S \frac{A_m}{h_p}, \qquad B_p(x) = \chi_p(x)\frac{e_{31}}{h_p}Q_p \text{ and } \qquad Q_p = \frac{b}{2}\left[\left(\frac{h_s}{2}+h_p\right)^2 - \left(\frac{h_s}{2}\right)^2\right]$$

where $A_m(x) = \int_0^L \chi_p(x) b dx = \chi_p(x) bL$ is the area of electrodes normal to the poling axis.

In particular, the piezoelectric actuator equation is called the strong form equation. This form should be change to the weak form for analytical solution. And the rest of them are used to find proper boundary conditions. The weak form equation will be described later.

$$\left\{EI(x)w_{xx} + \chi_p(x)e_{31}E_3Q_p\right\}\delta w_x\Big|_0^L = 0 \tag{3.36}$$

$$\left\{\left(EI(x)w_{xx}\right)_x + \chi_p(x)\left(e_{31}E_3Q_p\right)_x\right\}\delta w\Big|_0^L = 0 \tag{3.37}$$

3.5 Weak form equations

The strong form of the governing equations discussed so far are not quite suitable for numerical analysis. When numerical methods such as finite differences are applied to the strong form directly, they require 4th order spatial approximations. It can be quite difficult to tailor approximations of such high order spatial derivatives to arbitrary domains. In order to avoid such numerical approximation difficulties, the strong form equations can be converted into corresponding weak form equations. The weak form imposes fewer smoothness conditions on the approximation solution.

Multiplying Equation (3.35) by a test function, ψ, one of the governing equations is the piezoelectric actuator equation [50, 52]

$$\begin{aligned}\int_0^L \rho_\ell(x)\frac{\partial^2 w}{\partial t^2}\psi dx + \int_0^L \gamma\frac{\partial w}{\partial t}\psi dx + \int_0^L EI\frac{\partial^2 w}{\partial x^2}\frac{d^2\psi}{dx^2}dx \\ = V(t)\int_0^L B_p(x)\frac{d^2\psi}{dx^2}dx + \int_0^L f(x,t)\psi dx\end{aligned} \tag{3.38}$$

The second equation is the sensor equation representing the differential equation of charge q with respect to time,

$$i(t) = \frac{dq}{dt}(t) = C_p^S\dot{V}(t) + \int_0^L B_p(x)\frac{\partial^2\dot{w}}{\partial x^2}dx \tag{3.39}$$

In these equations, the composite linear density is given by

$$\rho_\ell(x) = h_s b\rho_s + 2\cdot\chi_p(x)h_p b\rho_p$$

γ is the viscous damping, $EI(x)$ is the effective bending stiffness, $B_p(x)$ is the electro-mechanical coupling parameter, $V(t)$ is the voltage across the PZT thickness, q is the total charge, C_p^S is the inherent capacitance of PZT layer, ρ_s is the density of the substrate, and ρ_p is the density of the PZT. Here the electro-mechanical coupling parameter is given by the integral

$$B_p(x) = \int_{A_p} \chi_p(x) z e_{31} N_{vj} dA \tag{3.40}$$

where z is the distance from neutral axis and $e_{31} = d_{31} \cdot c_{11}$ is the piezoelectric constant.

Chapter 4

Averaging analysis of switching piezostructures

4.1 Introduction

The dynamic system under consideration introduces a switching topology to generate the voltage and currents that drive the piezostructures. Switching topologies can be modeled based on the concept of *hybrid systems*. The switched systems have complexity for mathematical model and computational analysis to closely describe the physical systems since these systems change abruptly in time. For this reason, simplified but accurate models are needed for the physical system. This chapter describes analytical techniques and tools for the design and analysis of switched systems based on the method of averaging.

4.2 Shunt capacitance representation

The averaging method has been used for analyzing complicated switching behavior in power electronics and nonlinear vibrations [57, 68]. Recently, this approach

was applied to piezoelectric switching systems in Kurdila *et al.* and Kim *et al.* [7, 25]. The averaging method allows one to approximate the original, linear, time variant system model by time invariant system.

In this section, a model of a switched capacitive shunt system is developed. A prototype of a vibration absorber for energy harvesting is described which can shift the target frequencies within a discrete range of capacitances. In the special case, the dynamics can be represented in terms of a collection of discrete switching states or in terms of a single fixed switching state as shown Figure 4-1 and Figure 4-2.

Figure 4-1 is a compact representation of the linear piezoelectric system and the discrete switching system. The total capacitance in this system is realized through a collection of parallel capacitors that are engaged by actuating a finite number of discrete switches. In contrast, a fast-switching configuration is depicted in Figure 4-2. In this configuration, the total capacitance of the shunt circuit is changed by using a switching cycle that is modulated rapidly. This results in a system that exhibits nearly continuous variation of capacitance.

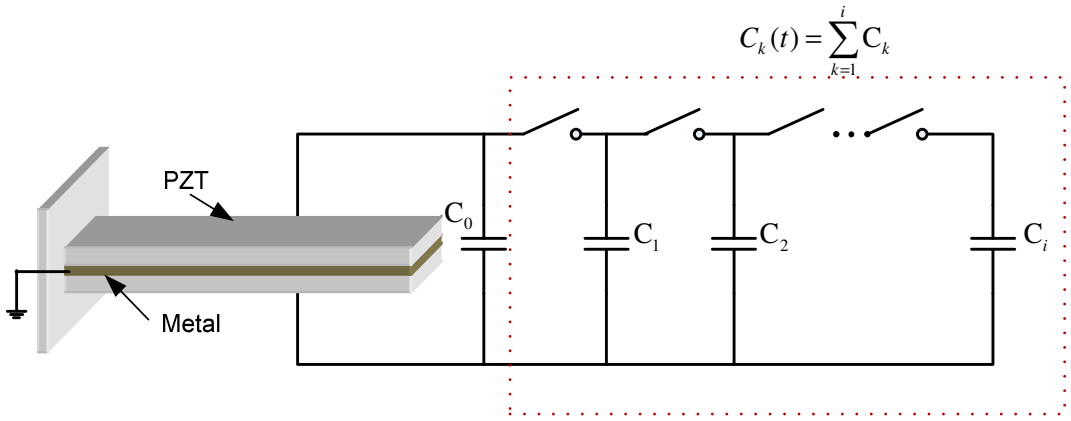

Figure 4-1. Multi-discrete capacitive shunt system. Total shunt capacitance value is sum of each capacitor

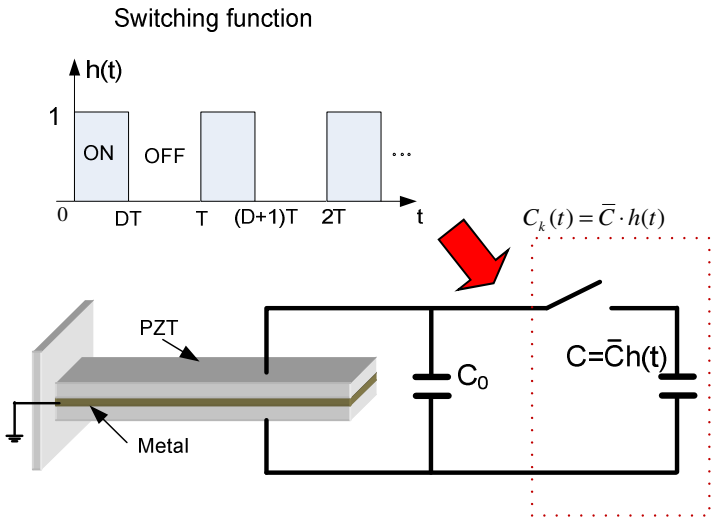

Figure 4-2. Switched capacitive shunt system controlled by switching function. In the switching function, $D = T_{ON}/T$ is duty ratio.

According to the Kirchhoff's law, the charges are a function of the sum of capacitances. Recall that the charge and the voltage are related by

$$q_{sh} = C_k(t)V(t) \tag{4.1}$$

Note that the sum of the charge q through the PZT structure and charge q_{sh} in the shunt capacitance is given by

$$q_{sh} + q = 0 \tag{4.2}$$

After integrating Equation (3.39) over time and substituting Equation (4.2), the voltage across the shunt capacitance becomes

$$V(t) = -\frac{\int_0^L B_p(x)\dfrac{\partial^2 w(x,t)}{\partial x^2}dx}{C_p^S + C_0 + C_k(t)} \tag{4.3}$$

where $C_k(t)$ is a time variant capacitance controlled by the switches. The discrete configuration of the switching circuit is indexed by the integer, k. Substitution of Equation (4.3) into Equation (3.38) provides the weak form of the equations for the switched piezostructure;

$$\int_0^L \rho_A(x)\frac{\partial^2 w}{\partial t^2}\psi dx + \int_0^L \gamma\frac{\partial w}{\partial t}\psi dx + \int_0^L EI(x)\frac{\partial^2 w}{\partial x^2}\frac{\partial^2 \psi}{\partial x^2}dx + \frac{\int_0^L B_p(x)\frac{\partial w^2}{\partial x^2}dx \cdot \int_0^L B_p(x)\frac{\partial^2 \psi}{\partial x^2}dx}{C_P^S + C_0 + C_k(t)} = \int_0^L f(x,t)\psi dx \tag{4.4}$$

4.3 Switching representation

Several observations should be made regarding the governing equations summarized in the previous chapter. These equations were derived from the principles of linear piezoelectricity and linear electrical networks. As long as the topology of the network does not change with time, and the assumption of linearity of the electrical components and transducer elements holds. With the introduction of the idealized switches, the network topology can now change abruptly in time. In this section the switched piezoelectric system will be discussed.

4.3.1 Switching function

As illustrated in Figure 4-3, $h(t)$ is a pulse-width-modulated (PWM) function characterized by the period T and the duty ratio D which takes a value between 0 and 1. The pulse function $h(t)$ is one when the switch is on and zero when the switch is off.

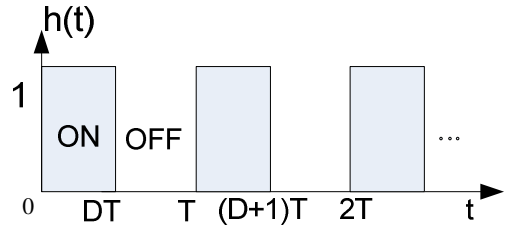

Figure 4-3. Switching function h(t), Period T and duty ratio D.

The capacitance value is expressed as $C_k(t) = \overline{C} \cdot h(t)$, where $h(t)$ is defined as

$$h(t) = \begin{cases} 1, & t \in [(k-1)T \quad ((k-1)+D)T] \\ 0, & t \in [((k-1)+D)T \quad kT], \quad k = 1,2,3... \end{cases} \tag{4.5}$$

4.3.2 Capacitive shunt switching

The set of governing equations describing the current system can be transformed into a set of ordinary differential equations using the modal expansion Equations (3.11) and (3.12) , we can write

$$\mathbf{M}\ddot{\mathbf{r}}(t) + \mathbf{Q}\dot{\mathbf{r}}(t) + (\mathbf{K} + \Delta\mathbf{K})\mathbf{r}(t) = \mathbf{f} \tag{4.6}$$

where the matrices $\mathbf{M}$, $\mathbf{Q}$, $\mathbf{K}$, $\Delta\mathbf{K}$ and vectors $\mathbf{b}$, $\mathbf{f}$ above are defined to be

$$\mathbf{M} = \int_0^L \rho_A \psi_{ri}(x)\psi_{rj}(x)dx$$

$$\mathbf{K} = \int_0^L EI(x) \cdot \frac{\partial^2 \psi_{ri}}{\partial x^2} \frac{\partial^2 \psi_{rj}}{\partial x^2} dx$$

$$\mathbf{Q} = \alpha_0 \mathbf{M} + \alpha_1 \mathbf{K}$$

$$\Delta \mathbf{K}(t) = \frac{\int_0^L B_p(x) \frac{\partial^2 \psi_{ri}}{\partial x^2} dx \cdot \int_0^L B_p(x) \frac{\partial^2 \psi_{rj}}{\partial x^2} dx}{C_p^S + C_0(t) + C_k(t)} = \begin{cases} \dfrac{\mathbf{b} \cdot \mathbf{b}^T}{C_p^S + C_0 + \sum_{k=1} C_k} : & \text{for multi-switching system} \\ \dfrac{\mathbf{b} \cdot \mathbf{b}^T}{C_p^S + C_0 + \bar{C}h(t)} : & \text{for single switching system} \end{cases}$$

$$\mathbf{b} = \int_0^L B_p(x) \frac{\partial^2 \psi_{ri}}{\partial x^2} dx$$

$$\mathbf{f} = \int_0^L f(x_i, t) \psi_{ri} dx$$

For the special case of base excitation, the force vector $\mathbf{f}$ can be written as [52]

$$\mathbf{f} = -\mathbf{M}_b \ddot{u}_g = -\left[\int_0^L \rho(x) \psi_{ri}(x) dx \right] \ddot{u}_g$$

where $\ddot{u}_g$ is base acceleration.

4.4 Switching system: state-space representation

4.4.1 Theoretical background of switching system

The piezoelectric transducer that is connected to a switched shunt circuit can be modeled as a hybrid switching system [27]. The hybrid switching system is characterized by discrete states and continuous states, depending on transitions between continuous and discrete inputs and states. The continuous state continues until the discrete state occurs, and then it abruptly changes in time when the discrete state is triggered. The modified hybrid switching system [69] is described in Equation (4.7) .

$$\frac{d\mathbf{x}(t)}{dt} = \mathbf{f}_{i_k}(t, \mathbf{x}(t)), \qquad t \in \left[t_k, t_{k+1}\right) \tag{4.7}$$

where $i_k\left(t_k\right) = S(t_k, \mathbf{x}(t_k), \{i_j\}_{j=0\ldots k-1})$ is the switching control input, representing the particular topology that is taken by the switched piezoelectric system. It equivalently can be viewed as a state designating the on/off conditions of all the switches. The function, S, is the switching sequence that describes how the switching variable changes as a function of time, state and previous switching history. The switching time sequence is given by $\{\cdots, t_{k-1}, t_k, t_{k+1}, \cdots\}$ while the switching state i_k for $k = 1, 2, 3, \cdots, K$ evolves.

4.4.2 State-space modeling for switching pulse input

The electromechanical switching system evolves according to the switching dynamics. Suppose that the closing or opening switching interval is defined as illustrated in Figure 4-3. The set of ordinary differential equations in Equations (4.6) can be converted into a periodically switched state-space form of equations with simple switching state, i,

$$\dot{\mathbf{x}}(t) = \mathbf{f}_i\left(t, \mathbf{x}(t), \mathbf{u}(t)\right), \qquad \mathbf{x}(0) = \mathbf{x}_0 \tag{4.8}$$

where, $\mathbf{x}(t)$ is the state vector, $\mathbf{u}(t)$ is input force vector, $\mathbf{f}_i$ is a smooth vector field and $\mathbf{x}(t) = [\mathbf{r}(t) \quad \dot{\mathbf{r}}(t)]^T$.

The open-circuit and short-circuit system illustrated in Figure 4-3 is a special case of hybrid-switching systems. Suppose that $i = 1$ and 2 represent the switch turned on and off, respectively. Equation (4.6) can be expressed in the state form;

$$\begin{aligned} &\dot{\mathbf{x}}(t) = \mathbf{A}_i(t)\mathbf{x}(t) + \mathbf{B}_i(t)\mathbf{u}(t) \qquad \text{for} \qquad i = 1,2 \\ &\mathbf{x}(0) = \mathbf{x}_0 \end{aligned} \tag{4.9}$$

with $\mathbf{x} \in \mathbb{R}^{n\times 1}$ the state-state variables, $\mathbf{u} \in \mathbb{R}^{n\times 1}$ the control input for $t \geq 0$. The system matrix is $\mathbf{A}_i \in \mathbb{R}^{n\times n}$, and the control influence matrix is $\mathbf{B}_i \in \mathbb{R}^{n\times m}$. Equation (4.9) can be expressed as

$$\dot{\mathbf{x}}(t) = \begin{cases} \mathbf{A}_1(t)\mathbf{x}(t) + \mathbf{B}_1\mathbf{u}(t) & t \in \left[(n-1)T \qquad \{(n-1)+D\}T \right], \text{ switch on} \\ \mathbf{A}_2(t)\mathbf{x}(t) + \mathbf{B}_2\mathbf{u}(t) & t \in \left[\{(n-1)+D\}T \qquad nT \right], \qquad \text{switch off} \end{cases}, \quad n = 1,2,\cdots,N$$

(4.10)

where

$$\mathbf{A}_1(t) = \begin{bmatrix} \mathbf{0} & \mathbf{I} \\ -\mathbf{M}^{-1}\left(\mathbf{K} + \dfrac{\mathbf{b}\cdot\mathbf{b}^T}{C_p^S + C_0 + \bar{\bar{C}}} \right) & -\mathbf{M}^{-1}\mathbf{Q} \end{bmatrix}, \quad \mathbf{A}_2(t) = \begin{bmatrix} \mathbf{0} & \mathbf{I} \\ -\mathbf{M}^{-1}\left(\mathbf{K} + \dfrac{\mathbf{b}\cdot\mathbf{b}^T}{C_p^S + C_0} \right) & -\mathbf{M}^{-1}\mathbf{Q} \end{bmatrix}$$

(4.11)

Assuming that the external source is not affected by the switch, the control influence matrix $\mathbf{B}$ is given as,

$$\mathbf{B} = \mathbf{B}_1 = \mathbf{B}_2 = \begin{bmatrix} \mathbf{0} \\ -\mathbf{M}^{-1}\mathbf{M}_b \end{bmatrix} \tag{4.12}$$

4.5 Mathematical background of averaging method

In this section, the equations derived in Sections 4.2 and 4.3 are cast in the form that is amenable to the derivation of an equivalent, averaged system. This discussion begins with a quick review of averaging techniques in general, and subsequently applies that framework to the governing equations for linear piezoelectricity.

4.5.1 General method of averaging

As derived in the previous section, The method of averaging can be an efficient approach to approximating the solution by superimposing two different time scale states. The dynamics of the system is described within the framework of hybrid systems, wherein the switching law is considered as a control input and the state variables are regarded as smoothly varying terms. Under the assumptions of existence and uniqueness of the solution of this hybrid system as shown below [70], the averaging theory can be applied provided that the original system dynamics is periodic or quasi periodic.

The assumptions commonly encountered in the literature include the following:

a) The functions $\mathbf{f}$ and $\partial \mathbf{f} / \partial \mathbf{x}$ are defined, continuous and bounded by a constant M in $[0,\infty)\times D$.

b) The function $\mathbf{f}(t,\mathbf{x})$ is T-periodic in t and has the average of $\mathbf{f}^0(\mathbf{x})$ where T is a constant independent of ε. That is, the average is defined to be

$$\mathbf{f}^0(\mathbf{x}) = \lim_{T\to\infty} \frac{1}{T}\int_0^T \mathbf{f}(t,\mathbf{x})dt \tag{4.13}$$

c) The average response $\mathbf{y}(t)$ belongs to an interior subset of D. The equation governing $\mathbf{y}(t)$, an approximation of $\mathbf{x}(t)$, is written as

$$\frac{d\mathbf{y}}{dt} = \varepsilon \mathbf{f}^0(\mathbf{y}), \quad \mathbf{y}(t_0) = \mathbf{x}_0 \tag{4.14}$$

Then, $\mathbf{x}(t) - \mathbf{y}(t) = O(\varepsilon)$ for $0 < \varepsilon t < C$ where C is constant. The detailed proof is shown in [70]

Prior to developing the averaging theory as it applies to the switching system, it is important to understand the basic structure and theorems of classical averaging theory. In the present dynamic model, the dynamic motion consists of continuously varying states and discrete switching states. The dynamic response of the system to be averaged can be represented as a set of first order differential equation

$$\dot{\mathbf{x}} = \mathbf{f}(t, \mathbf{x} : \varepsilon) \tag{4.15}$$

where $\mathbf{x}(t) \in \mathbb{R}^n$, $\mathbf{f}(t, \mathbf{x} : \varepsilon)$ is a mapping of $\mathbb{R}^+ \times \mathbb{R}^n \mapsto \mathbb{R}^n$ and $t \geq 0$. The standard form of avearging is written as

$$\dot{\mathbf{x}} = \varepsilon \mathbf{f}(t, \mathbf{x}(t)), \ \mathbf{x}(0) = \mathbf{x_0} \text{ , and } 0 < \varepsilon \ll 1 \tag{4.16}$$

The average of $\mathbf{f}$ is typically given as

$$\mathbf{f^0}(\mathbf{x}) \triangleq \frac{1}{T} \int_0^T \mathbf{f}(s, \mathbf{x}) ds \tag{4.17}$$

The associated form of the averaged initial value problems is defined to be

$$\dot{\mathbf{y}} = \varepsilon \mathbf{f}^0(\mathbf{y}), \quad \mathbf{y}(t_0) = \mathbf{x}_0 \tag{4.18}$$

4.6 Application of averaging method to switching shunt systems

4.6.1 Switching function: change of variable

The response of the switched electromechanical system has its characteristic time constant defined in forms of the switching frequency. From the switching scheme shown in Figure 4-3, the parameter ε is inversely proportional to switching frequency. Thus, ε and τ can be chosen as the switching period T and the switching integers N respectively. From Equation (4.5), the switching time, t, satisfies $t \in [0, NT]$ if and only if $\tau \in [0, N]$. Thus, the switching function can be written as

$$\hat{h}(\tau) \triangleq h(\varepsilon\tau) = h(T \cdot \tau) = \begin{cases} 1, & \tau \in [(n-1), \quad n-1+D] \\ 0, & \tau \in [(n-1+D), \quad n] \end{cases} \tag{4.19}$$

where $n = 1, 2, 3, \cdots, N$

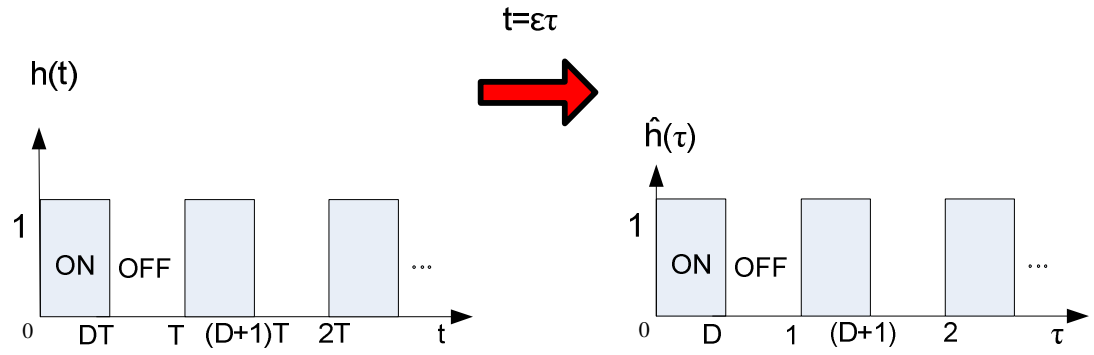

Figure 4-4. The switching function is characterized by period T and duty ratio D.

A new time scale variable τ is introduced. In order to establish an approximation of the original time variant system, the time scaling factor ε is introduced. The switched equation can be cast in a form that is suitable for applying the classical averaging technique by introducing new independent variable or a time scaling factor. Suppose that the time scaling is written as

$$t = \varepsilon\tau \tag{4.20}$$

with

$$\varepsilon = T = \frac{1}{f_s} \tag{4.21}$$

where f_s is switching frequency. Note that ε approaches zero as the switching frequency f_s increases to infinity. It is worth noting that switching rate depends on the hardware used to realize the switch. In practice, the switching period T may be measured in *microseconds.* It is assumed that structural period is NT where $N \gg 1$.

4.6.2 State-space averaging for switching system

Denote that $\mathbf{x}(t) \equiv \mathbf{x}(\varepsilon\tau) = \hat{\mathbf{x}}(\tau)$. We can now change variables and write

$$\frac{d\mathbf{x}}{dt}(t) = \frac{d\mathbf{x}}{dt}(\varepsilon\tau) = \frac{1}{\varepsilon}\frac{d\hat{\mathbf{x}}}{d\tau}(\tau) \tag{4.22}$$

After applying the change of variables, we define the scaled vector field

$$\hat{\mathbf{f}}(\tau, \hat{\mathbf{x}}) = \varepsilon\left(\hat{\mathbf{A}}_i\hat{\mathbf{x}}(\tau) + \hat{\mathbf{B}}_i\hat{\mathbf{u}}(\tau)\right) \tag{4.23}$$

where $i = 1, 2, 3, \cdots, r$. After applying the change of the variables, we have

$$\begin{aligned}\frac{d\hat{\mathbf{x}}}{d\tau}(\tau) &= \hat{\mathbf{f}}(\tau, \hat{\mathbf{x}}, \varepsilon) \\ &= \varepsilon\left[\hat{\mathbf{A}}_i\hat{\mathbf{x}}(\tau) + \hat{\mathbf{B}}_i\hat{\mathbf{u}}(\tau)\right]\end{aligned} \tag{4.24}$$

From Equation (4.13), evolution in τ domain is given in terms of the average

$$\begin{aligned}\mathbf{f}^0(\hat{\mathbf{x}}) &= \frac{1}{T_f}\int_0^{T_f}\sum_{i=1}^{S}\mathbf{f}_i(\tau, \hat{\mathbf{x}}, \hat{h}(\tau))dt, \qquad i = 1, 2 \\ &= \frac{1}{NT}\int_0^{TN}\left[\mathbf{f}_1(\tau, \hat{\mathbf{x}}, \hat{h}(\tau)) + \mathbf{f}_2(\tau, \hat{\mathbf{x}}, \hat{h}(\tau))\right]dt\end{aligned} \tag{4.25}$$

where $\mathbf{f}_1(t, \mathbf{x}(t))$ corresponds to switch-on and $\mathbf{f}_2(t, \mathbf{x}(t))$ corresponds to switch-off.

Define the response in the τ time scale to be

$$\mathbf{x}(t) = \mathbf{x}(T\tau) \triangleq \hat{\mathbf{x}}(\tau) \tag{4.26}$$

The general equations of averaging for the piezostrucutral system can then be written as

$$\mathbf{y}(t) = \mathbf{x}_{avg}(t) \triangleq \frac{1}{T_f}\int_0^{T_f} \mathbf{x}(t)dt \tag{4.27}$$

$$\dot{\mathbf{y}}(t) = \dot{\mathbf{x}}_{avg}(t) \triangleq \frac{1}{T_f}\int_0^{T_f} \frac{d\mathbf{x}(t)}{dt}dt \tag{4.28}$$

where $T_f = T \cdot N$ is final switching time. In the similar manner, we define

$$\begin{aligned}\mathbf{y}(\tau) \triangleq \hat{\mathbf{x}}_{avg}(\tau) &= \frac{1}{TN}\int_0^{TN} \mathbf{x}(t)dt \\ &= \frac{1}{TN}\int_0^{TN} \mathbf{x}(T\tau)(Td\tau) \\ &= \frac{1}{N}\int_0^{N} \hat{\mathbf{x}}(\tau)d\tau\end{aligned} \tag{4.29}$$

Note that, from Equation (4.20), the relation between the variables of integration dt and $d\tau$ is $dt = Td\tau$.

Immediately, we have

$$\begin{aligned}\mathbf{y}'(\tau) \triangleq \frac{d\mathbf{y}(\tau)}{d\tau} &= \frac{d}{d\tau}\frac{1}{N}\int_0^{TN} \hat{\mathbf{x}}(\tau)d\tau \\ &= \frac{1}{N}\int_0^{N} \frac{d\hat{\mathbf{x}}(\tau)}{d\tau}d\tau\end{aligned} \tag{4.30}$$

Substituting Equation (4.24) into Equation (4.30), the final form of the system to be averaged is obtained

$$\mathbf{y}'(\tau) \triangleq \varepsilon\frac{1}{N}\int_0^{N} \left[\mathbf{A}_i\hat{\mathbf{x}}(\tau) + \mathbf{B}_i\hat{\mathbf{u}}(\tau)\right]d\tau \tag{4.31}$$

Application of the averaging method to the switched piezostructural system requires several integrals. By definitions introduced above, we can write

$$\begin{aligned}
\hat{\mathbf{A}}_{avg} &= \frac{1}{N}\left[\int_0^N \mathbf{A}_1(\hat{h}(\tau))d\tau + \int_0^N \mathbf{A}_2(\hat{h}(\tau))d\tau\right] \\
&= \frac{1}{N}\left\{\sum_{n=1}^{N}\int_{n-1}^{n-1+D} \mathbf{A}_1(\hat{h}(\tau))d\tau + \sum_{n=1}^{N}\int_{n-1+D}^{n} \mathbf{A}_2(\hat{h}(\tau))d\tau\right\} \\
&= \frac{1}{N}\left\{\sum_{n=1}^{N}\left[\begin{array}{cc} \mathbf{0} & \mathbf{I} \\ -\mathbf{M}^{-1}\left(\mathbf{K} + \dfrac{\mathbf{b}\cdot\mathbf{b}^T}{C_p^S + C_0 + \bar{C}}\right) & -\mathbf{M}^{-1}\mathbf{Q} \end{array}\right]D + \sum_{n=1}^{N}\left[\begin{array}{cc} \mathbf{0} & \mathbf{I} \\ -\mathbf{M}^{-1}\left(\mathbf{K} + \dfrac{\mathbf{b}\cdot\mathbf{b}^T}{C_p^S + C_0}\right) & -\mathbf{M}^{-1}\mathbf{Q} \end{array}\right](1-D)\right\} \\
&= \left[\begin{array}{cc} \mathbf{0} & \mathbf{I} \\ -\mathbf{M}^{-1}\mathbf{K}_{eff} & -\mathbf{M}^{-1}\mathbf{Q} \end{array}\right]
\end{aligned}$$

(4.32)

The effective stiffness is defined as

$$\mathbf{K}_{eff} = \left(\mathbf{K} + \frac{\mathbf{b}\cdot\mathbf{b}^T}{C_p^S + C_0 + \bar{C}}D + \frac{\mathbf{b}\cdot\mathbf{b}^T}{C_p^S + C_0}(1-D)\right) \tag{4.33}$$

In this equation, D is duty ratio of PWM signal. Therefore, the averaged equations of motion are given as

$$\mathbf{y}'(\tau) = \varepsilon\left[\hat{\mathbf{A}}_{\mathbf{avg}}(D)\mathbf{y}(\tau) + \mathbf{B}\mathbf{u}(\tau)\right] \tag{4.34}$$

By using the chain rule,

$$\frac{d(\cdot)}{dt} = \frac{d(\cdot)}{d\tau}\frac{d\tau}{dt} = \frac{1}{\varepsilon}\frac{d(\cdot)}{d\tau} \tag{4.35}$$

It is easy to see that

$$\begin{aligned}\mathbf{y}(\tau) &= \hat{\mathbf{x}}_{avg}(\tau) \\ &= \mathbf{x}_{avg}(\varepsilon\tau) \\ &= \mathbf{y}(t)\end{aligned} \tag{4.36}$$

and

$$\begin{aligned}\mathbf{y}'(\tau) &= \frac{1}{N}\int_0^N \frac{d\hat{\mathbf{x}}(\tau)}{d\tau}d\tau \\ &= \frac{\varepsilon}{TN}\int_0^{TN} \frac{d\mathbf{x}(t)}{dt}dt \\ &= \varepsilon\dot{\mathbf{y}}(t)\end{aligned} \tag{4.37}$$

Substituting Equations (4.36) and (4.37) into Equation (4.34), the averaged model is rewritten as

$$\frac{d}{dt}\mathbf{y}(t) = \hat{\mathbf{A}}_{\mathbf{avg}}(D)\mathbf{y}(t) + \mathbf{B}\mathbf{u}(t) \tag{4.38}$$

If the mass is invariant over the switching period, the dynamic equation with respect to the averaged variable $\mathbf{y}(t)$ can be written as

$$\mathbf{M}\ddot{\mathbf{y}}(t) + \mathbf{Q}\dot{\mathbf{y}}(t) + \left(\mathbf{K} + \frac{\mathbf{b}\cdot\mathbf{b}^T}{C_p^S + C_0 + \bar{C}}D + \frac{\mathbf{b}\cdot\mathbf{b}^T}{C_p^S + C_0}(1-D)\right)\mathbf{y}(t) = \mathbf{f} \tag{4.39}$$

4.7 Frequency variation in capacitive shunt system

Equation (4.39) shows that the stiffness in the averaged system is a function of the duty cycle and capacitance. It is easy to see that the natural frequency can be shifted by controlling the duty cycle. It also implies that the semi-active switching system can induce variations in the natural frequencies of the system. Let Φ_r and η_r be the modal vector and modal amplitude at the r^{th} mode respectively. A modal expansion that retains I-modes is given by

$$\mathbf{y}(t) = \mathbf{\Phi\eta} = \sum_{r=1}^{I} \Phi_r \eta_r(t) \tag{4.40}$$

Substitution Equation (4.40) into (4.39), we find

$$\mathbf{M}^*\ddot{\boldsymbol{\eta}}(t) + \mathbf{Q}^*\dot{\boldsymbol{\eta}}(t) + \mathbf{K}^*_{eff}\boldsymbol{\eta}(t) = \mathbf{f}^* \tag{4.41}$$

where

$$\mathbf{M}^* = \mathbf{\Phi}^T\mathbf{M}\mathbf{\Phi}$$

$$\mathbf{Q}^* = \mathbf{\Phi}^T\mathbf{Q}\mathbf{\Phi}$$

$$\mathbf{K}^*_{eff} = \mathbf{\Phi}^T(\mathbf{K} + D\frac{\mathbf{b}\cdot\mathbf{b}^T}{C_p^S + C_0 + \bar{C}} + (1-D)\frac{\mathbf{b}\cdot\mathbf{b}^T}{C_p^S + C_0})\mathbf{\Phi}$$

$$= \mathbf{k}^* + D\frac{\boldsymbol{\theta}\cdot\boldsymbol{\theta}^T}{C_p^S + C_0 + \bar{C}} + (1-D)\frac{\boldsymbol{\theta}\cdot\boldsymbol{\theta}^T}{C_p^S + C_0}$$

$$\mathbf{K}^* = \mathbf{\Phi}^T\mathbf{K}\mathbf{\Phi}$$

$$\boldsymbol{\theta} = \mathbf{\Phi}^T\mathbf{b}$$

$$\mathbf{f}^* = \mathbf{\Phi}^T\mathbf{f}$$

From the modal expansion of the dynamic equation, one can estimate the shifted natural frequency induced via the switching. The effective frequency ω_r^{eff} in the averaged equations is written as

$$\omega_r^{eff} = \sqrt{\left(k_r^* + D\frac{\theta_r \cdot \theta_r^T}{C_p^S + C_0 + \bar{C}} + (1-D)\frac{\theta_r \cdot \theta_r^T}{C_p^S + C_0} \right) \Big/ M_r^*} \quad , \qquad r = 1,2,... \qquad (4.42)$$

Equation (4.43) is readily interpreted as the ratio between the shifted natural frequency and the natural frequency at closed-circuit condition.

$$\frac{\omega_r^{eff}}{\omega_r^E} = \sqrt{\left(k_r^* + D\frac{\theta_r \cdot \theta_r^T}{C_p^S + C_0 + \bar{C}} + (1-D)\frac{\theta_r \cdot \theta_r^T}{C_p^S + C_0} \right) \Big/ \left(k_r^* + \frac{\theta_r \cdot \theta_r^T}{C_p^S + C_0 + \bar{C}} \right)} \qquad (4.43)$$

Where ω_r^E are the resonant frequency at the closed-circuit condition.

Chapter 5

Experimental results

5.1 Experimental setup

An experimental study was conducted to investigate the dynamic characteristics of a switched piezostructural system and also to validate the theoretical models described in the previous section. A schematic of the test arrangement used in the following experiments is presented in Figure 5-1. The test fixture is a PZT composite bimorph cantilever beam which is labeled as, “T226-A4-503X”. The piezoelectric material patches are attached symmetrically to the top and bottom side of the brass beam. The detailed material properties are summarized in Table 5.1.

A laser vibrometer is used to measure the velocity near the tip at the far right of the piezoelectric bimorph. The base of the beam is driven by an excitation at the far left in Figure 5-1. A force transducer (PCB 2008C02) is used to measure the input signal generated by the electromagnetic shaker. The input signal is a sine sweep signal with a frequency resolution o f0.13Hz. The spectrum analyzer SIGLAB is used to analyze the signal.

The electrodes on the top and bottom surfaces of the piezoelectric layers are connected to the electric circuits described below. For the capacitive shunt tests, two different types of switching systems are used: the Discrete Capacitor (DC) and the

MOSFET Fast Switched (MFS) configurations. The DC configuration as illustrated in Figure 4-1 is a capacitance array operated by several switches. It is easy to see that the capacitance is maximized when all of the switches are closed. For the single switching test, the MOSFET IRF 820 was used. The control input is a PWM signal which is generated by a function generator (HP3341A).

Table 5.1. Material properties of beam and piezoceramics: T226-A4-503X (source :www.piezo.com)

Brass	Density(ρ_s)	8700 kg/m^3
	Effective length(L)	50×10^{-3}m
	Effective width(b)	31.8×10^{-3}m
	Thickness(h)	0.127×10^{-3}m
	Elastic modulus(c_S)	95 GPa
Piezoceramic	Density (ρ_p)	7800 kg/m^3
	d constant (d_{31})	-190e-12 m/V
	Zero strain capacitance (C_P^T)	50nF
	Dielectric (ε_{33}^T)	1800 ε^0
	Coupling coefficient (k_{31})	0.35
	Effective length(L)	51.0×10^{-3}m
	Effective width(b)	31.8×10^{-3}m
	Effective thickness (h_p)	0.27×10^{-3}m
	Elastic modulus (c_{11}^E)	66 Gpa
Shunt capacitance	Initial shunted capacitance (C_0)	330 pF
	Shunted capacitance ($\overline{C}$)	480 nF

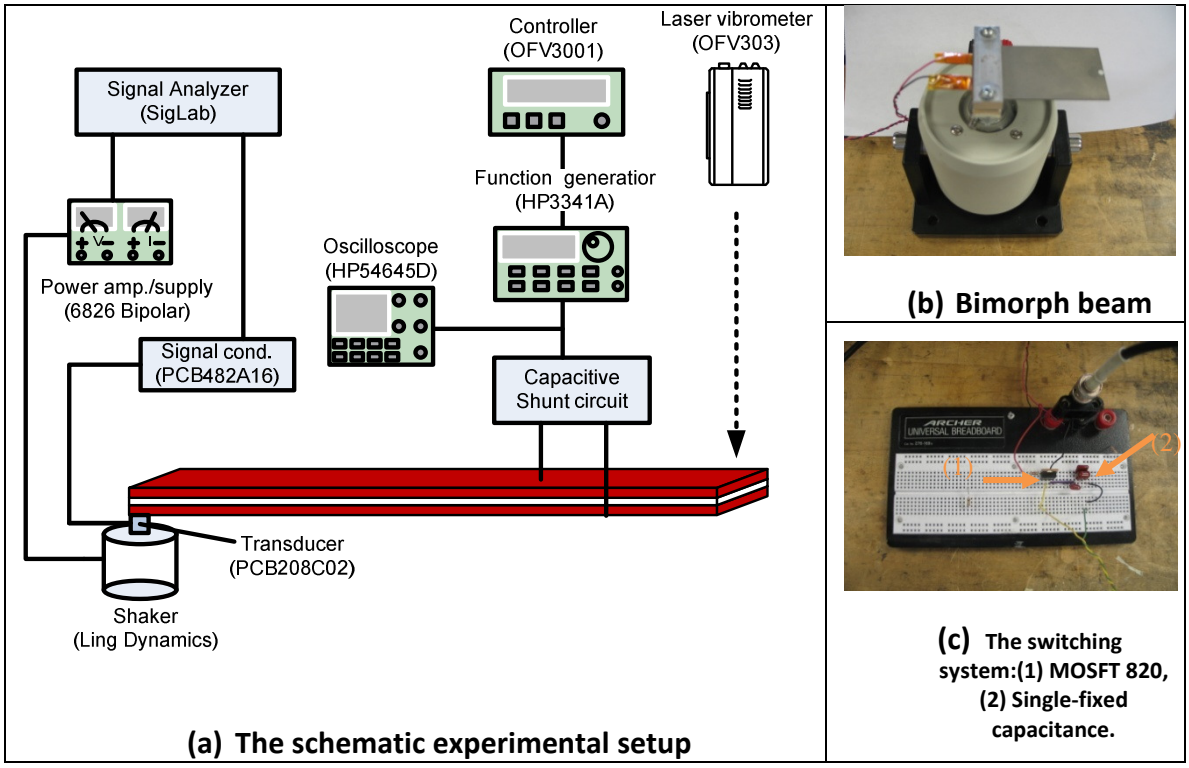

Figure 5-1. A bimorph cantilever beam cantilever beam setup

5.2 Results and discussion

5.2.1 Frequency response: analytical prediction and experimental results

The purpose of this section is to summarize the results of experiments to verify and validate the approximate solutions described in the previous Chapter. In turn, it will be shown how to obtain continuously varying natural frequencies by integrating a PWM driven switch into piezostructural system. We show that the approximate solution obtained via an averaging method is well matched with the experimental results. Note that only the first mode is considered in the models of the experiment.

Table 5.2 includes the range of resonant frequencies, the comparison between experiment and the simulation results, and the sum of ladder capacitance from the short to the open circuit conditions. Figure 5-2 and Figure 5-3 are the frequency response functions and tuning response of the ladder capacitance corresponding to Table 5.2. Each capacitance has a tuning frequency. "Tuning 1" is the effective range of frequency shift. This range is the possible change of the frequency from the short circuit to the open circuit conditions. Note that tuning 1 corresponds to the tuning ratio between 0.01 and 100 times the initial capacitance C_p, and tuning 2 corresponds to the tuning ratio between 0.1 and 10 times the initial capacitance C_p as shown in Figure 5-3. The initial capacitance C_p is the sum of C_p^T and C_0. Clearly, the difference between the frequency ranges described by tuning 1 and tuning 2 is that the change in the plot in Figure 5-3 over the range given by turning 2 is rising sharply. The change of the plot in Figure 5-3 in the frequency range labeled tuning 1 has small slope.

In order to obtain approximately continuous frequency shifts, the capacitance value had to be chosen carefully. As shown in Figure 5-3, $C^{eff} / C_p = 10$ is the critical transition point from shallow to steep slope and indicates an almost short circuit

condition. The short circuit condition is a static condition in that all switches are turned on. In other words, switching frequencies are not involved. This implies that regardless of switching frequencies, the critical capacitive value of the capacitive ladder circuit at short circuit condition is the same as that of a single switch circuit and can be selected to determine the shunt capacitive value for any single switching system. As highlighted in Table 5.2, the capacitance of 480nF corresponds to $C^{eff} / C_p = 10$. This value is chosen for a single switch system.

Table 5.2. Tuning frequency of the ladder capacitance

Frequency [Hz]				Sum of capacitance [nF] $C_k(t)$	
No.(k)	Tuning	Numerical	Experimental		
13	f_{SC}	122.7			
12	f_1	122.8	122.6	2431.33	
11	f_2	123	123.2	1231.33	
10	f_3	123.3	123.4	480.33	
9	f_4	124.0	124.0	206.33	
8	f_5	124.8	124.5	112.33	
7	f_6	125.6	125.4	66.33	
6	f_7	126.3	126.0	44.33	
5	f_8	127.3	127.0	22.33	
4	f_9	128.1	127.8	11.33	
3	f_{10}	128.5	128.4	5.93	
2	f_{11}	128.9	128.5	2.37	
1	f_{12}	129.1	128.7	0.99	
0	f_{OC}	129.1	128.9	0.33	

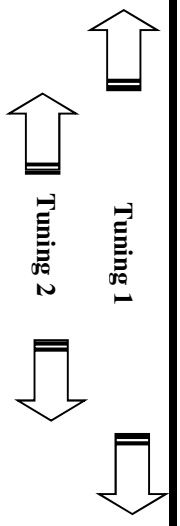

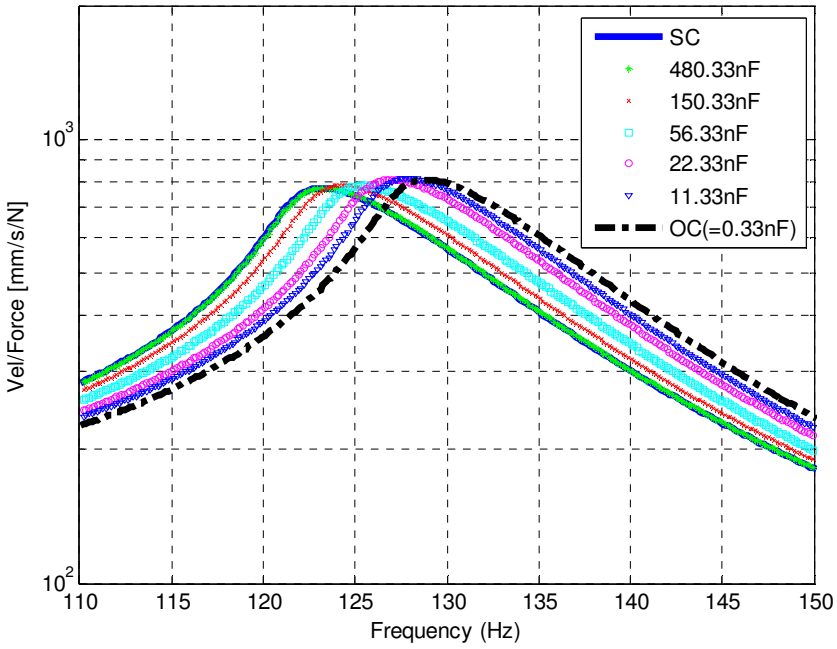

Figure 5-2. Frequency response function: Multi-ladder capacitance.

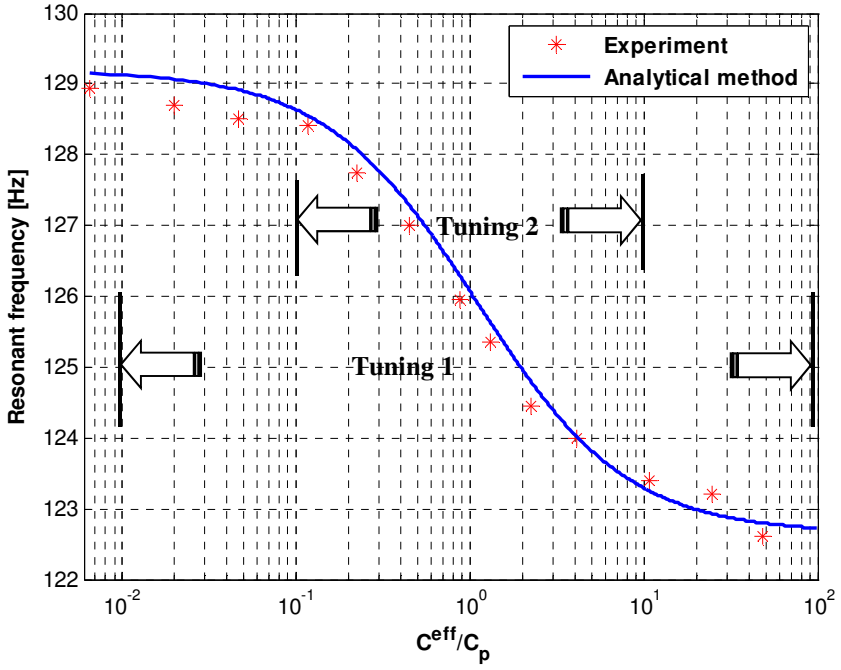

Figure 5-3. Tuning frequency at ladder capacitance: Comparison of analytical and experimental results. This graph corresponds to Table 5.2

Figure 5-4 and Figure 5-5 depict the change in resonant frequencies obtained by the experiments. On the vertical axis the normalized effective frequency ratio $\omega_r^{eff} / \omega_r^E$ is plotted, where ω_r^{eff} is the resonant frequency of the shunted bimorph that depends on the shunted capacitance values and ω_r^E is the natural frequency of the elastic short circuit bimorph. The normalized effective frequency ratio measures the frequency range over which the resonant frequency of the shunted bimorph may be shifted. The value of this ratio varies from $\omega_r^{eff} / \omega_r^E = 1$, to roughly $\omega_r^{eff} / \omega_r^E = 1.05$. This range means that the range over which the resonant frequency can be changed is roughly 5% of the short circuit frequency.

Figure 5-4 illustrates the ratio of the effective natural frequency as a function of the normalized discrete capacitances, C^{eff} / C_p. The constant C^{eff} is the sum of the ladder

capacitances. The initial capacitance C_p is the sum of C_P^T and C_0. It shows that the effective range of the capacitance values is between 0.01 and 100 times the initial capacitance C_p. The data points marked in red (*) correspond to measurements made in the DC configuration. As noted in the figure, the data for the DC configuration is in good agreement with the theoretical prediction of Equation (4.6). This is also consistent with the results in [5].

Figure 5-5 suggests that there is a feasible alternative to selecting among a fixed set of pre-selected design points. The data in Figure 5-4 corresponding to the MFS configuration shows that the same range of effective frequencies is achieved as in the DC configuration. The effective frequency of the shunted piezoelectric in the MFS configuration is controlled by the duty cycle D. The duty cycle can be modulated nearly continuously. Moreover, the data for the MFS Configuration is in good agreement with the analysis represented in Equation (4.43)

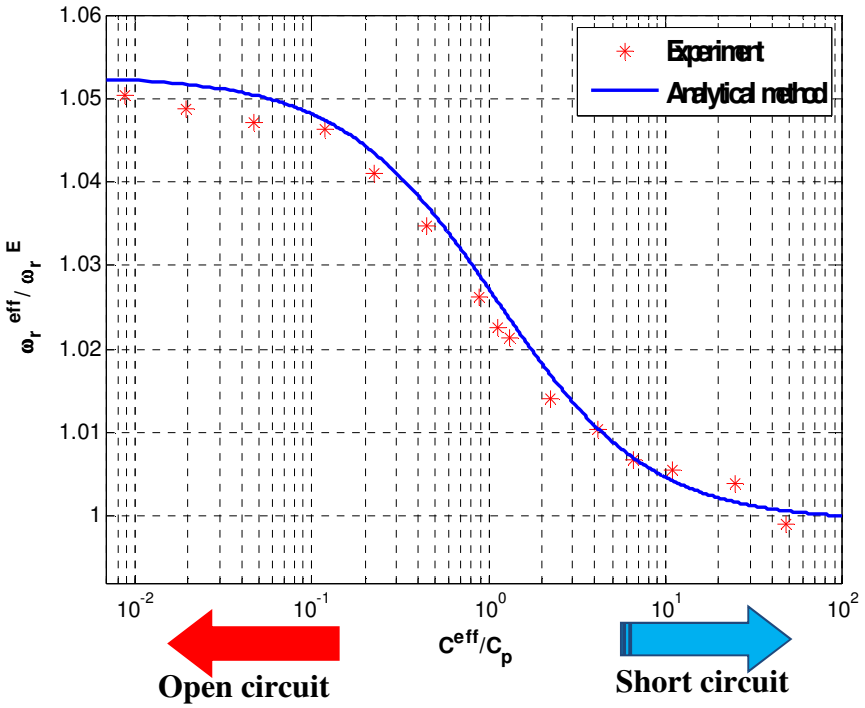

Figure 5-4. Normalized effective frequency versus effective shunt capacitance for DC configuration at 1st mode.

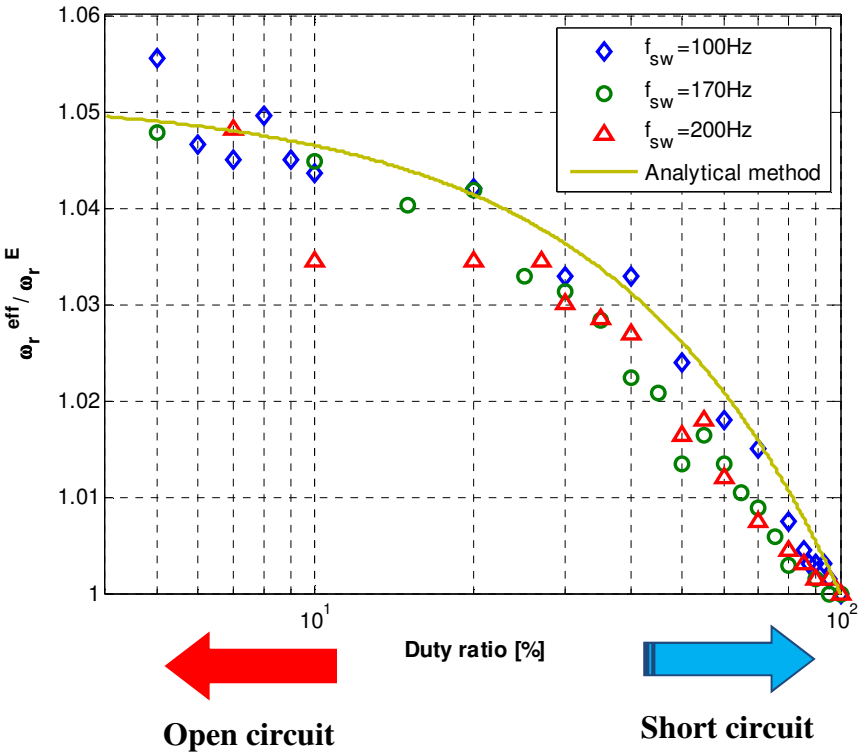

Figure 5-5. The comparison of experimental results and analytical solution at 1st mode: Normalized effective frequency versus Duty ratio in MFS configuration.

In the following Figure 5-6 and Figure 5-7, we will see how the effective natural frequency appears to vary with the duty cycle for various switching frequencies. These results provide insight into the variation of the effective frequency ratio as we vary the switching frequency.

The modal amplitude is shown in Figure 5-6, which depicts the effective natural frequency versus the duty cycle when the switching frequency is 100Hz and 200Hz, respectively. In this range of switching frequencies, the natural frequency shifts vary almost equally when the duty ratio changes.

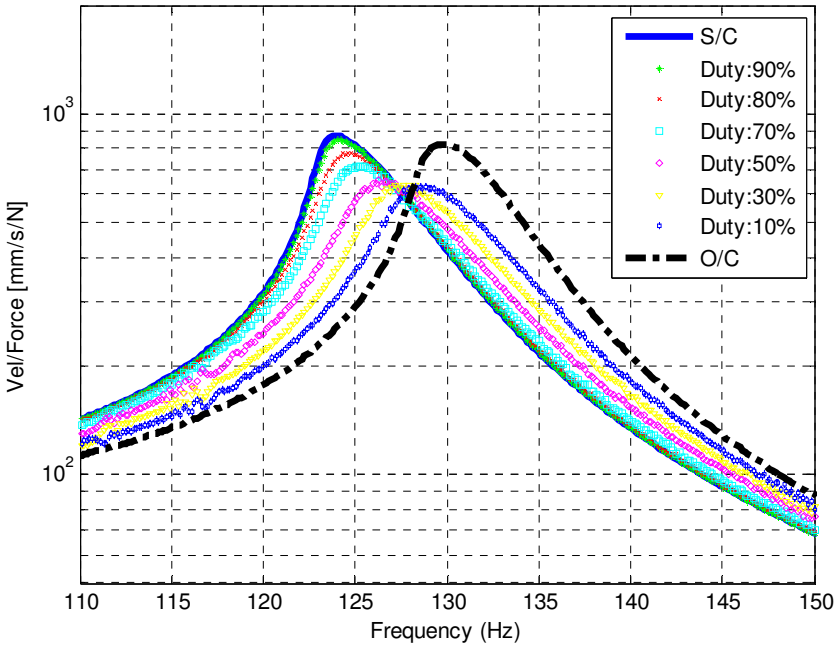

(a) Switching frequency (fs) = 100Hz

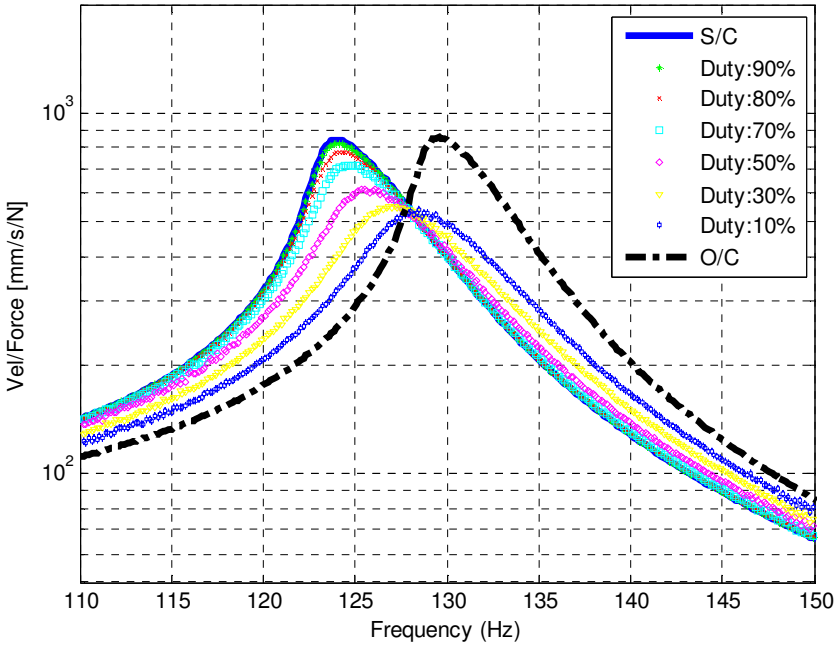

(b) Switching frequency (fs) = 170Hz

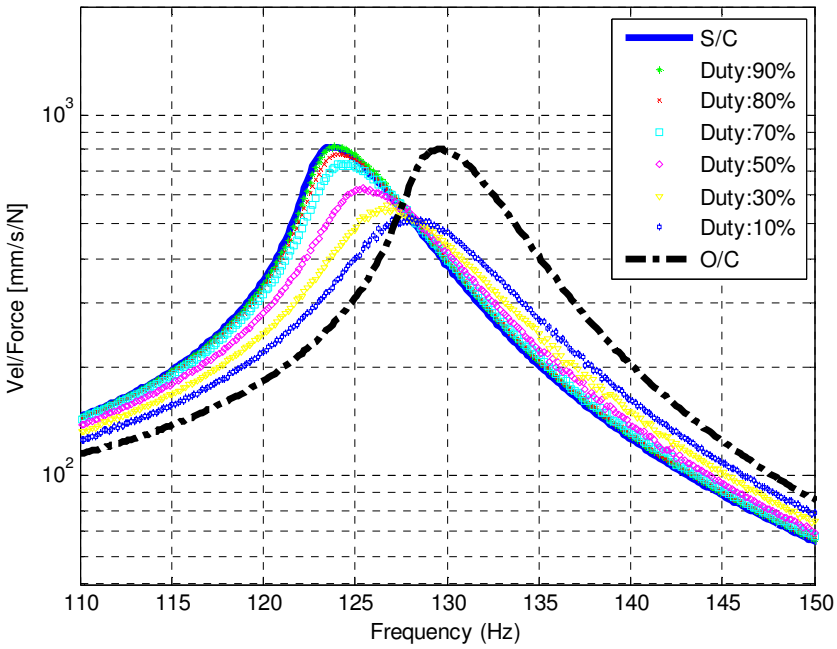

(c) Switching frequency (fs) = 200Hz

Figure 5-6. Effective range of PWM switching frequency at 1st mode: Resonant frequency varies from 123Hz at short circuit condition to 130Hz at open circuit condition.

The following graphs illustrate the modal amplitude variation when a PWM switching signal is applied. As can be seen in Figure 5-7(a) and Figure 5-7(b), all of the values of frequency for different duty cycles tend to accumulate near the short circuit condition whenever the switching frequency is too high, beyond a range of 600Hz. Furthermore, it is observed that there is no significant difference in modal amplitude with respect to duty cycle when the switching frequency is 1kHz. This implies how fast the capacitance is charged or discharged plays an important role in determining when the switching systems can yield frequency adaptation. One of the recommendations for future research suggests additional study of this behavior. The more detailed relationship between switching frequency and averaging behavior should be considered in further research.

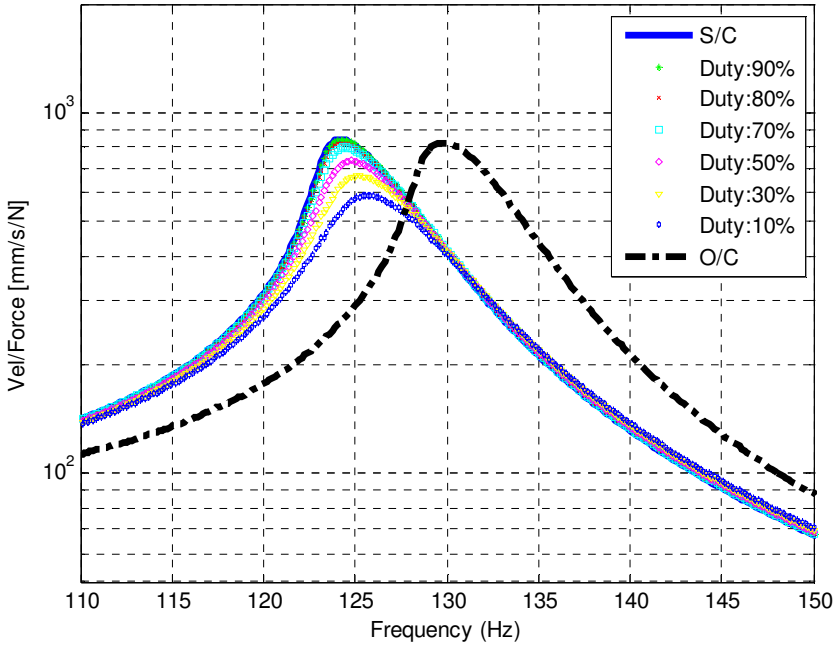

(a) Switching frequency (fs) = 600Hz

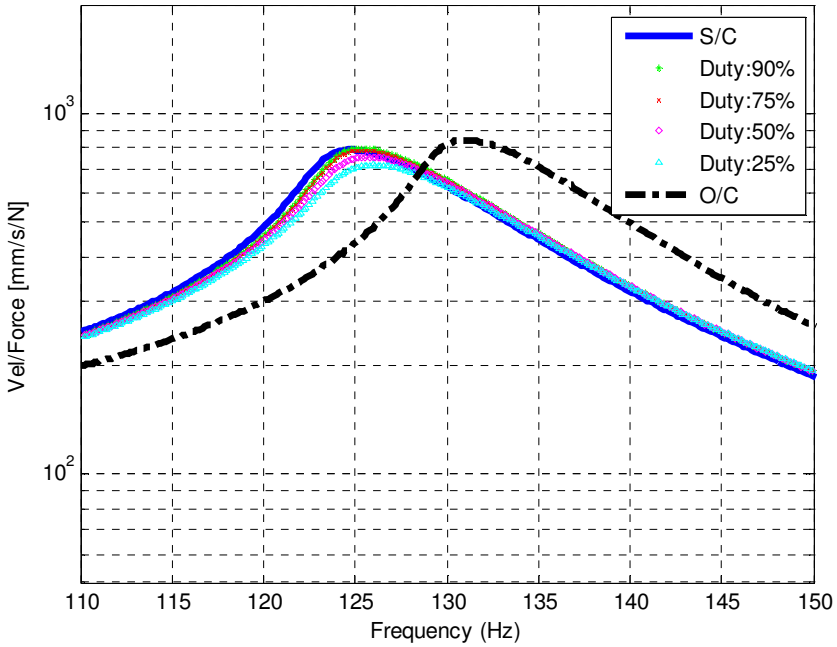

(b) Switching frequency (fs) = 1kHz

Figure 5-7. Out of range of PWM switching frequency at 1st mode

5.2.2 Harmonic excitation response for switching shunt

In order to extract the maximized power, it is important that the mechanical system is designed to vibrate near the resonant frequency. In our system, a single switch topology, controlled by the duty cycle, is employed to tune the natural frequency. It is important to investigate the effects of the structural resonant frequency coinciding with that of the energy harvesting transducer. The following graphs show a trend that was observed when the switching frequency was selected to be 100Hz.

In this section, the velocity at the beam tip and the voltage obtained from the PZT patches as the duty cycles was varied for a 100Hz switching frequency is summarized in Figure 5-8 through Figure 5-10. These figures illustrate the resonant structural responses in the time domain as we varied the duty ratio. The vibrometer is used to measure the velocity at the beam tip. The electromagnetic shaker connected to the fixed end of the beam generates the sinusoidal excitation associated with the resonant frequency for a specific duty ratio. However, instead of using SIGLAB as the previous experiment, a data acquisition system (NI cDAQ 9172) from National Instrument is used to collect data in time domain.

Figure 5-8(a) and Figure 5-8(b) show the amplitudes of velocities at or near the short circuit resonant condition, which corresponds to the exciting frequency f_s at 124 Hz. As shown in the Figure, the amplitude of velocity is higher when the base excitation frequency from the shaker is tuned to match the resonant frequency corresponding to a specific duty ratio. Velocities are markedly lower away from this specifically tuned duty ratio. Figure 5-8(b) compares the voltage extracted from the PZT transducer for different duty cycles. It is shown that the voltage for the tuned condition increases to twice as much as the voltage at the untuned condition. As seen in the figures, great improvement was observed when the natural frequency is tuned by adapting the duty ratio.

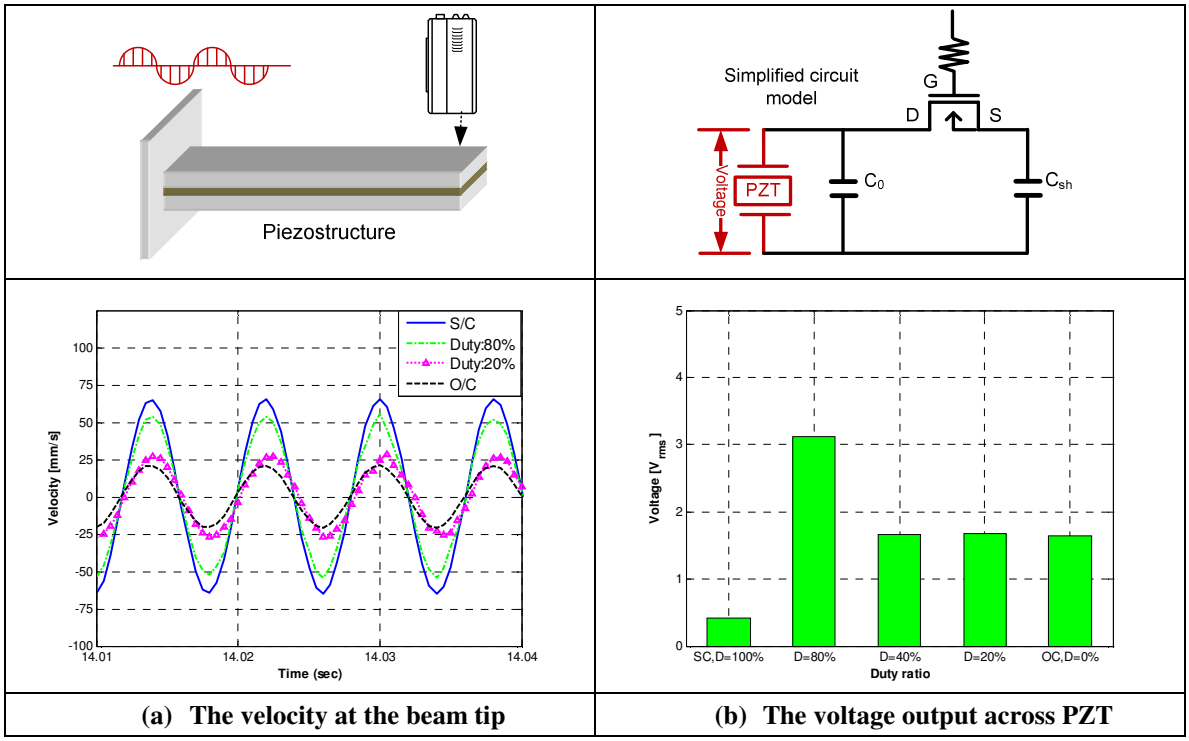

(a) The velocity at the beam tip **(b) The voltage output across PZT**

Figure 5-8. Excitation at short circuit resonance: source frequency, fs, from the exciter is 124 Hz. Switching frequency, fsw = 100 Hz. The fine-tuned duty ratio at resonant frequency provides higher amplitude than those at off-resonant frequency.

Figure 5-9 represents another tuning effect at or near a resonance when the excitation frequency varies. The excitation frequency f_s is set at 127 Hz. The duty ratio is arbitrary changed. It is observed that the amplitude of the velocity and the voltage are increased when the duty ratio is operated at 40%. This means that the duty ratio of 40% corresponds to the resonant frequency of 127 Hz. In a similar manner to that in Figure 5-8 and Figure 5-9, Figure 5-10 show the variation of tip response. Again, performance is improved by modulating the duty cycle to match the input frequency.

This work clearly demonstrates that adaptive tuning of the duty cycle can produce a response that has a strong resonant peak provided that some switching control strategies are involved. The PWM-driven switched piezostructures can provide larger amplitude at the resonance.

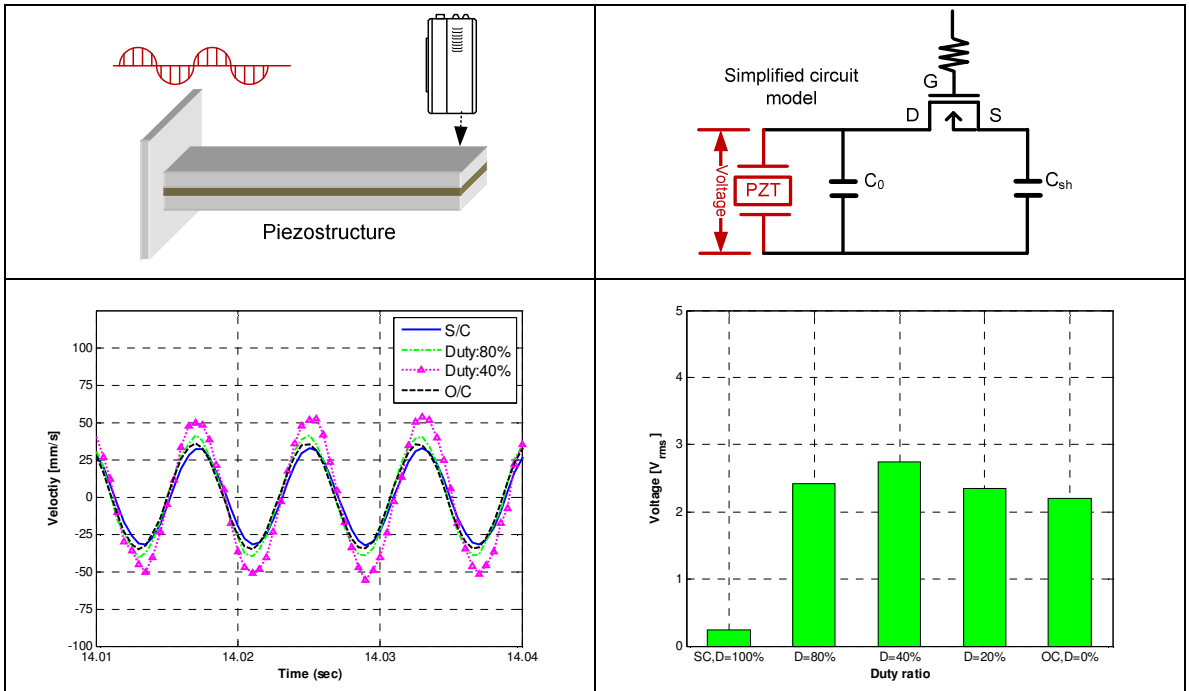

(a) The velocity at the beam tip **(b) The voltage output across PZT**

Figure 5-9. Excitation at D =40% resonance: source frequency, fs, from the exciter is 127 Hz. Switching frequency, fsw = 100 Hz.

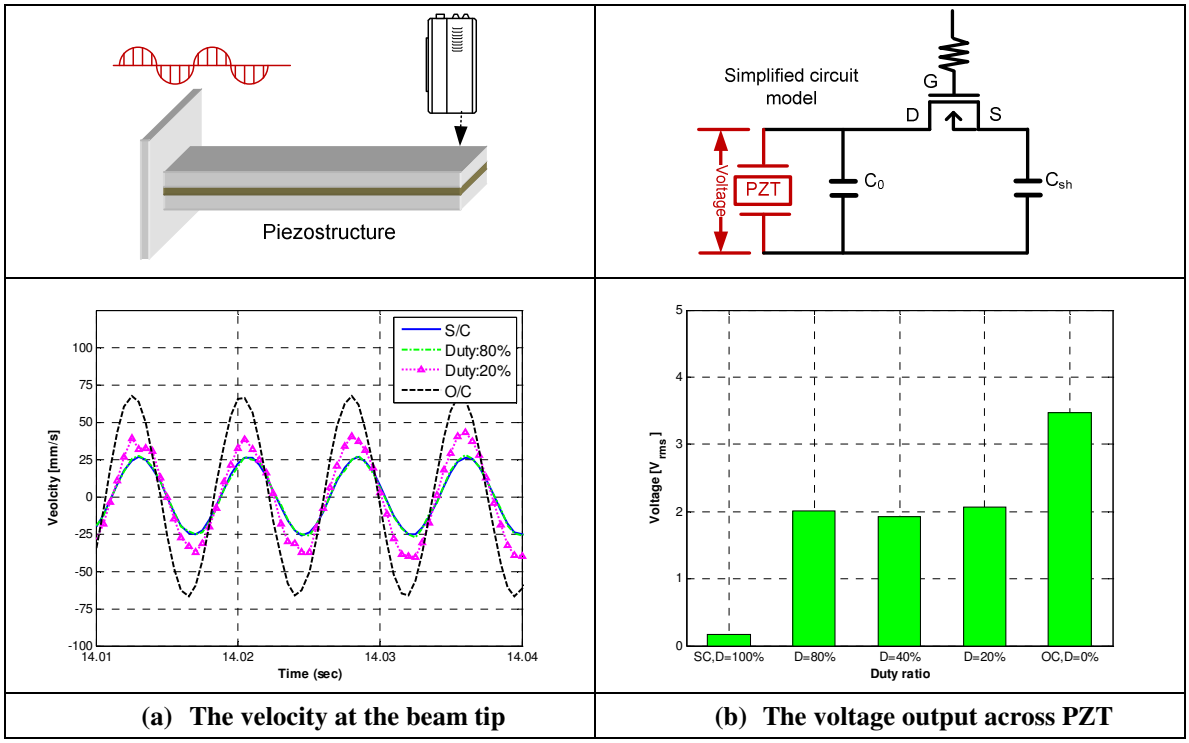

(a) The velocity at the beam tip | **(b) The voltage output across PZT**

Figure 5-10. Excitation at open circuit: source frequency, fs, from the exciter is 130 Hz. Switching frequency, fsw = 100 Hz.

Chapter 6

Conclusions and Future work

Conclusions

This research has developed a transducer and described a method to model a switch controlled semi-active piezoelectric structure. It is shown that the semi-active system shunted with capacitance is able to vary natural frequency by integrating a fast switch. The switching topology is analyzed by using an averaging method, which provides a simple and accurate estimate of the. The experimental study clearly shows that the first mode of a semi-actively shunted piezoelectric bimorph can be adjusted continuously by varying the duty cycle of the PWM input over a range of switching frequencies driven by a PWM signal.

Important conclusions of this research include the following:

i) Capacitive shunt, switching networks coupled to piezostructural systems enables resonant frequencies to be modulated nearly continuously between open-circuit (high stiffness) and short-circuit (low stiffness) conditions.

ii) Analytical framework for studying the vibration of switched piezostructural systems via ***averaging methods*** has been developed. It is shown that this analysis provides accurate and cost effective estimates of the dynamics for some semi-actively shunted piezoelectric structures.

iii) A new strategy to modulate the absorber frequency based on PWM signals is introduced, as opposed to the discrete switching system. A simple and compact equation describing the vibration response is expressed as a function of duty ratio of the PWM control input.

iv) The experimental study verifies that the first mode of the experimental prototype can be adjusted by continuously varying the duty cycle of the PWM input.

v) The approximate solution and experimental results are well matched as long as the switching frequencies are not too high.

Recommended Future work

The research presented in this dissertation has raised many questions. There are several lines of research arising from this work that should be pursued.

At the outset, it has been our intention to modify the effective stiffness of a piezoelectric structure. Capacitive ladder circuits and low frequency or quasi static switching have been used in the past to provide variable shunt capacitance. The focus of this dissertation is the replacement of such a circuit with a single high-frequency switched capacitor. In principle, both the switching frequency and duty cycle can be varied in this design. However, this dissertation focuses on modulation of the duty cycle alone and, as a result, the results are correct for a limited range of switching frequency. In the future, the timescale of capacitive discharging and the dissipative effects of rapid switching will be considered. When this is done, the averaging method employed to develop the PWM signal should give more complete results.

In addition, the semi-active switching system seems well-suited to the development of an adaptive energy harvesting device. Therefore, it would be interesting to see how the switching strategy introduced in this document could be used to achieve an adaptive energy harvesting transducer.

Appendix A

Stability of switching systems

A.1 Stability of state-switching system

The piezoelectric switching model in this dissertation can be described in terms of linear differential equations with time variant coefficient or as a hybrid system that contains continuous states and discrete states. As demonstrated in [3] and [69], it is theoretically possible that the state switched system can be destabilized by the input switching sequence. In this appendix, we will show for the example of a PZT structure how a state-switched system can be driven unstable by switching.

A.2 Two-state switching system

This section begins with the review of Kurdila's stability [69] based on Lyapunov function for a two-state system. This study showed that the trajectory of motion that results from using instantaneous switching can become unstable. Ideally, this example considered the case when switch events occurred at zero displacement and zero velocity. There is no change in potential energy and kinetic energy.

The analysis will be given for linear structures that are driven by switching systems. Consider the two-state switching system with a function of switching time,

$$m_{i_k}\ddot{x}(t)+c_{i_k}\dot{x}(t)+k_{i_k}x(t)=0 \tag{A.1}$$

where m is the mass, c is the damping, k is the stiffness and i_k is the discrete switching state. If m, c and k are constant between each switching event, the dynamics for a two state switching system results in two classical and stable oscillators denoted by the switching state $i_k = 1$ or $i_k = 2$. We can write the system equations as

$$m_1\ddot{x}(t) + c_1\dot{x}(t) + k_1x(t) = 0 \tag{A.2}$$

$$m_2\ddot{x}(t) + c_2\dot{x}(t) + k_2x(t) = 0 \tag{A.3}$$

The differential equation for the switching system in Equation (4.7) is defined as

$$\dot{\mathbf{y}}(t)=\mathbf{A}_{i_k}\mathbf{y}(t) \tag{A.4}$$

$$\mathbf{y}(t_0)=\mathbf{y}_0$$
$$\dot{\mathbf{y}}(t_0)=\dot{\mathbf{y}}_0$$

where

$$\mathbf{y}(t)=[x(t),\ \dot{x}(t)]^T,$$

$$\mathbf{A}_{i_k}=\begin{bmatrix}\mathbf{I} & \mathbf{0}\\ \mathbf{M}_{i_k}^{-1}\mathbf{K}_{i_k} & \mathbf{M}_{i_k}^{-1}\mathbf{C}_{i_k}\end{bmatrix}$$

$$x(t_0)=x_0$$
$$\dot{x}(t_0)=\dot{x}_0$$

Suppose for purposes of illustration. Define the k^{th} Lyapunov function $V_{i_k}(\mathbf{y})$ as

$$V_{i_k}(\mathbf{y}) = \frac{1}{2} k_{i_k} x_1 + \frac{1}{2} m_{i_k} x_2 \tag{A.5}$$

where $x_1 = x$ and $x_2 = \dot{x}$. It is straightforward to show that the integral of motion

$$\frac{x_1^2}{\left(\sqrt{2V_{i_k} / k_{i_k}}\right)^2} + \frac{x_2^2}{\left(\sqrt{2V_{i_k} / m_{i_k}}\right)^2} = 1 \tag{A.6}$$

holds for the k^{th} interval of time.

A.2.1 Switching analysis with variable elasticity driven by PWM signal

The stability of certain state-switching control strategies are studied in this section. We have seen previously that the trajectory of the switched system generates integrals of motion for each switching interval. We cans use these integrals of motion to infer that the response to some input switching systems yields unbounded evolution.

In this section, we assume linear second order dynamic system coupled by a switch as described in Equation (A.7). We will show that if the structure is driven by a specific periodically operated, then the trajectory become unstable.

One simple example of the differential equation with variable elasticity can be expressed as

$$m\ddot{x} + \left(k_1 + (1 - h(t))k_2\right) x = 0 \tag{A.7}$$

where $h(t)$ is a periodic function of the time. Suppose the function h(t) has two states, where $h(t)$ is equal to zero or one and a periodic switching frequency $\omega_k(t)$,

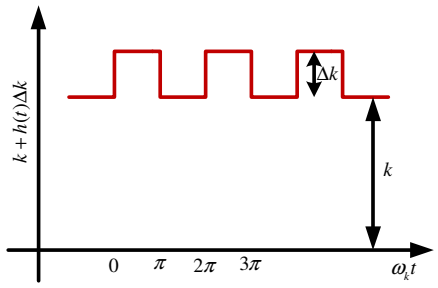

Figure A-1. Variation in elasticity for the rectangular switching function.

Figure A-1 illustrates the driving signal $h(t)$ and Figure A-2 depicts that the phase portrait of a state switching system corresponding to this periodic pulse input. The system starts in the high stiffness state. During the switch activation, $i_k = 1, 2, \cdots$, it alternates between the stiffness states.

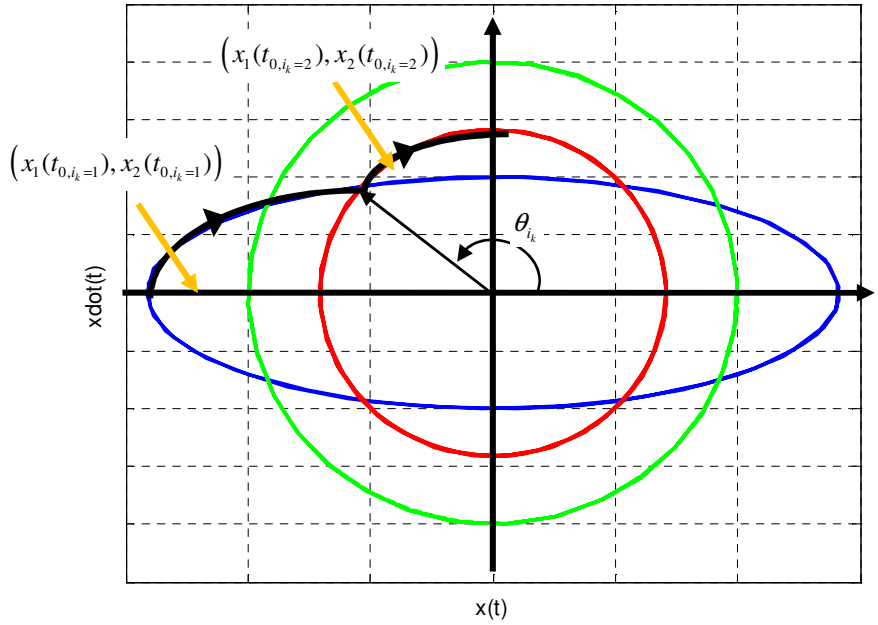

Figure A-2. Schematic of trajectory when switching events occur at arbitrary time.

From Equation (A.6), the states x_1 and x_2 are respectively

$$x_1 = \pm\sqrt{2V_{i_k}(x)/k_{i_k}}\cos(\theta_{i_k}(t))$$
$$x_2 = \pm\sqrt{2V_{i_k}(x)/m_{i_k}}\sin(\theta_{i_k}(t)) \quad \text{(A.8)}$$

The energy is always same when we have assumed that there is no damping and the switches are lossless. If we divide x_2 by x_1, we have

$$\frac{x_2}{x_1} = \sqrt{m_{i_k}/k_{i_k}}\tan(\theta_{i_k}(t)) \quad \text{(A.9)}$$

It is easy to see that $\theta_{i_k}(t)$ is written as

$$\theta_{i_k}(t) = \tan^{-1}\left(\frac{1}{\Delta\omega_{r,i_k}}\frac{x_2}{x_1}\right) \tag{A.10}$$

where $\Delta\omega_{r,i_k} = \frac{k_{i_k}}{m_{i_k}}$. The total energy can be written as

$$\begin{aligned} V_{i_k}(\mathbf{y}) &= k_{i_k}/2\left(x_1/\cos(\theta_{i_k}(t))\right)^2 \quad \text{or} \\ V_{i_k}(\mathbf{y}) &= m/2\left(x_2/\sin(\theta_{i_k}(t))\right)^2 \end{aligned} \tag{A.11}$$

where $\mathbf{y} = \{x_1, x_2\}^T$.

Figure A-3 illustrates the phase portrait for the switching system. As shown in the Figure, the stiffness is abruptly changed as a function of time. This system can always conserve energy by increasing the kinetic energy and not adding external energy. In addition, when the system switches from the lower stiffness to the higher stiffness, the stiffness is gradually increased to the higher state. As this occurs, potential energy steadily increases while the kinetic energy steadily decreases. If the system reaches zero velocity, or zero displacement, the total energy can dramatically be increased. For this case, external energy, due to initial condition, must be added to the system to achieve the stiffness change. This energy is gradually added until the switch is complete, at which point the system's trajectory is at a higher energy level. As this response continues, energy is added with each switch from low stiffness to high stiffness causing the trajectory to diverge and the system to become unstable.

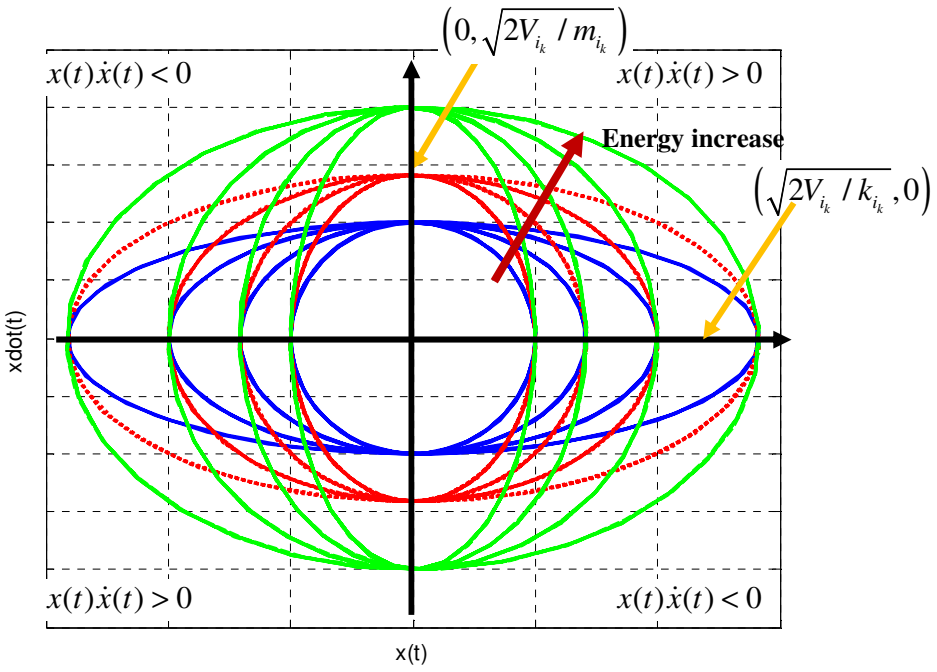

Figure A-3. The phase portrait for a linear and undamped system. This graph corresponding to Equation (A.6) shows the variation of mass and stiffness.

A.2.2 Motivating example I : switching occurs at zero displacement, but same level energy sets

Consider a second-order system with constant mass $m = 1$, with multiple discrete values for the stiffness. Choose, for example, the multiple discrete stiffness values to be $k = \{16.0, 8.0, 4.0, 2.0, 1.0, 0.5, 0.25\}$. Assume the switching is activated whenever $x_1 \cdot x_2 > 0$. Note that the initial conditions are $\mathbf{y}_0 = \left(\sqrt{V(x)/k_1}, 0\right)$. As shown in Figure A-4, the mass is constant and stiffness varies. Theoretically, the trajectory of displacement may evolve so that it is far from the origin by transitioning the stiffness at zero displacement. When this occurs, the velocity maintains a constant value and there is no change in the mechanical energy.

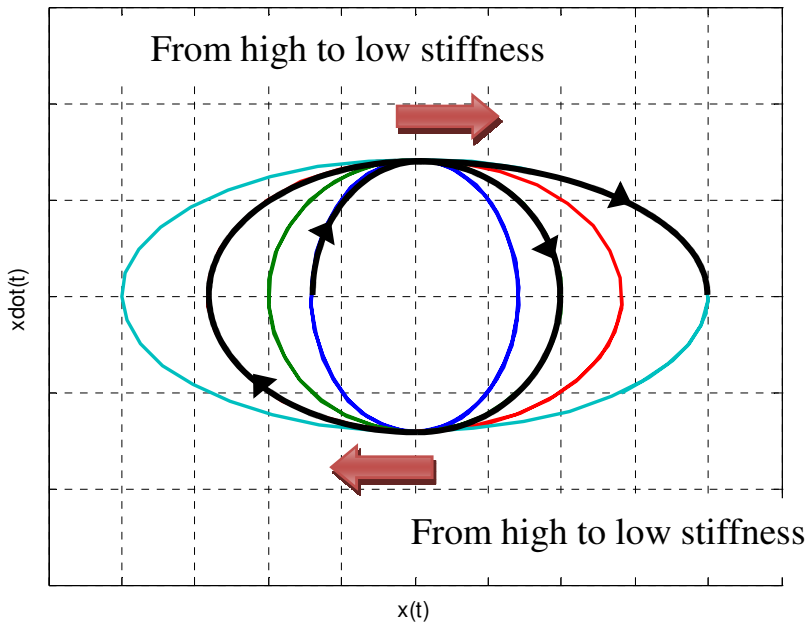

a) The conceptual phase portrait for destabilized switching system (Kurdila,2002).

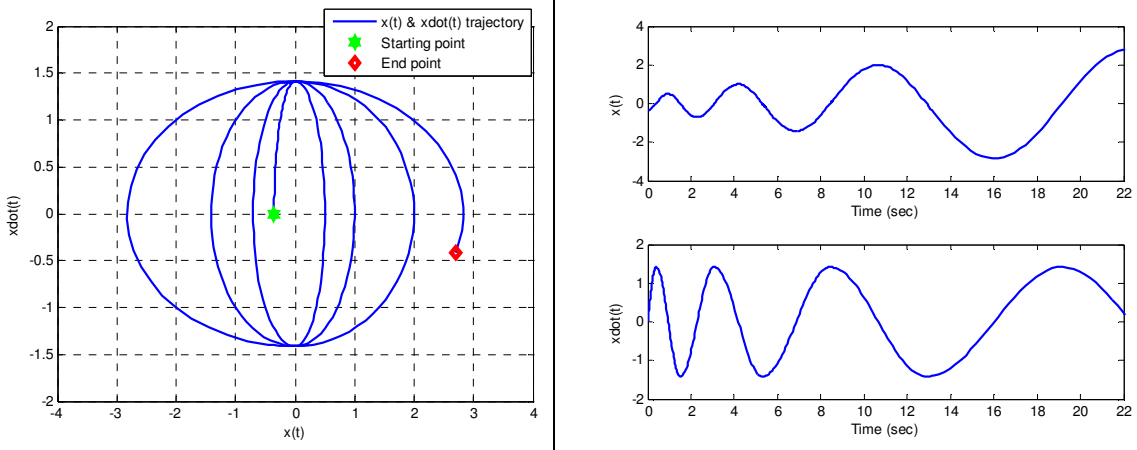

b) The switch is activated at $x \cdot \dot{x} \geq 0$.

Figure A-4. An example of destabilized switching system: the switch is activated at zero displacement points

.

A.2.3 Motivating examples II: switching occurs at arbitrary time.

In the real world, it is not possible that the switching events occur preciously at the instant of zero displacement or zero velocity. This section constructs a counterexample for stability of a randomly switched system. The switch is driven by PWM signal and randomly activated.. Let us consider a second-order system,

$$m\ddot{x} + \left(k_1 + (1-h(t))k_2\right)x = 0, \quad x_0 = \left(\sqrt{V_1 / k_1}, 0\right) \tag{A.12}$$

The multiple discrete stiffness variables are $\{k_1,\ k_2\} = \left\{(2\pi)^2 \times 1e4, (2\pi)^2 \times 1e5\right\}$. Note that the initial condition is selected to be $\mathbf{y}_0 = \left(\sqrt{V_{i_k,t_0}(\mathbf{y}) / k_1}, 0\right)$.

As shown in

Figure A-5. ~ Figure A-7. the mass is constant, but the stiffness varies. Theoretically, the trajectory of displacement may go far from the origin by transitioning the stiffness at zero displacement, but the velocity maintains constant value without change in the mechanical energy.

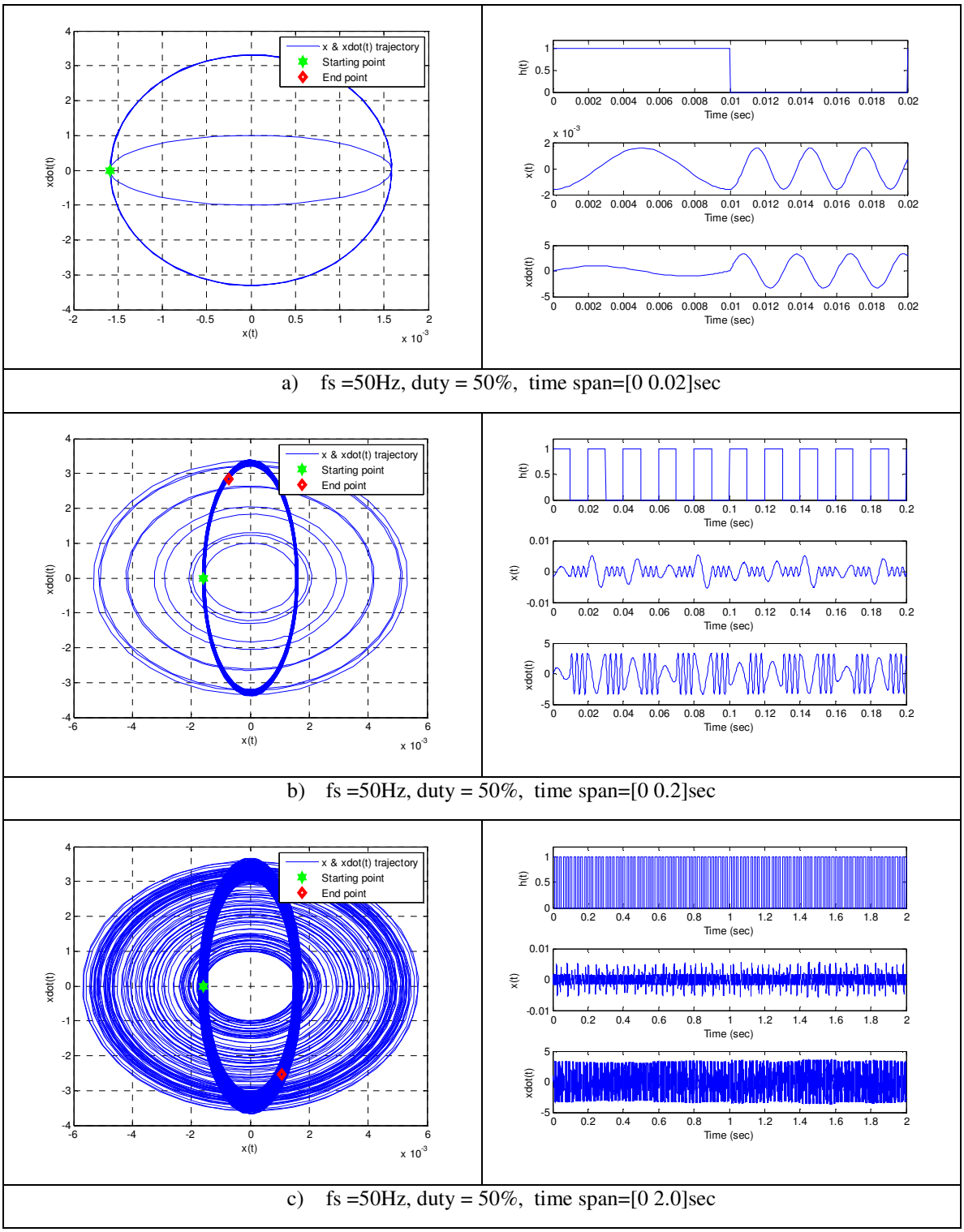

a) fs =50Hz, duty = 50%, time span=[0 0.02]sec

b) fs =50Hz, duty = 50%, time span=[0 0.2]sec

c) fs =50Hz, duty = 50%, time span=[0 2.0]sec

Figure A-5. Phase portrait diagram. The mas m is constant and the stiffness k varies. The switching frequency (fs) =50Hz, duty ratio = 50%. Simulation time increases downwardly. The left column is phase portrait and the right is the corresponding displacement and velocity.

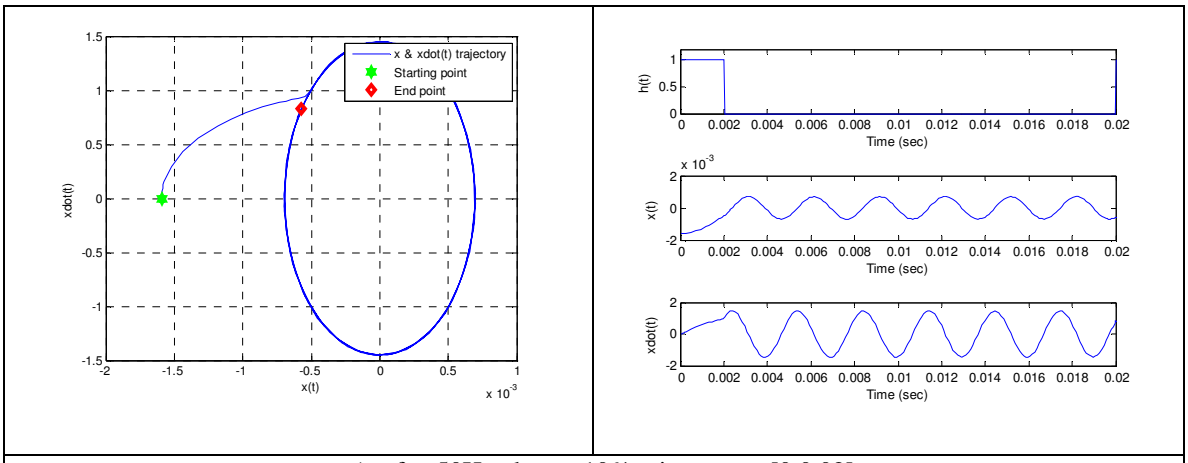

a) fs =50Hz, duty = 10%, time span=[0 0.02]sec

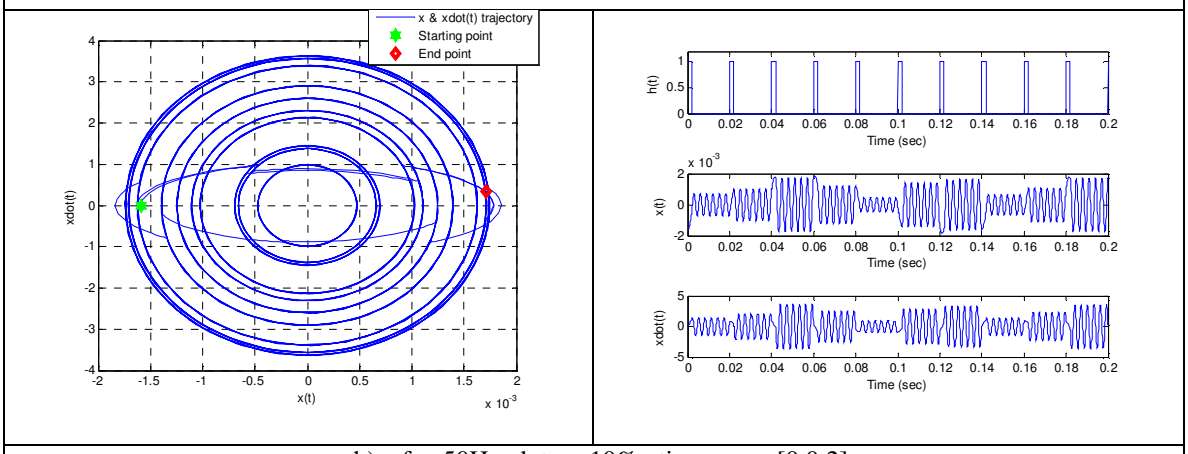

b) fs =50Hz, duty = 10%, time span=[0 0.2]sec

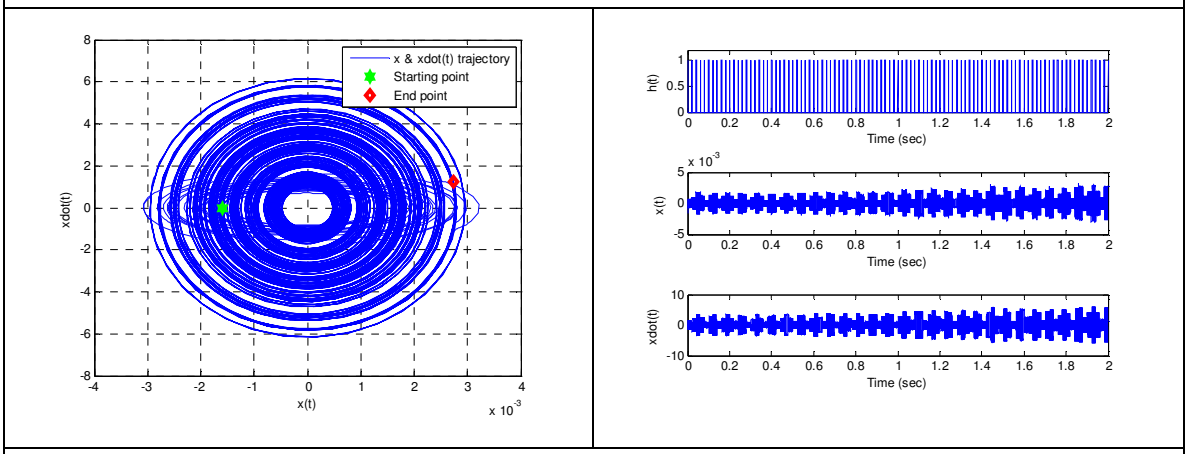

c) fs =50Hz, duty = 10%, time span=[0 2.0]sec

Figure A-6. Phase portrait diagram. The mas m is constant and the stiffness k varies. The switching frequency (fs) =50Hz, duty ratio = 10%. Simulation time increases downwardly. The left column is phase portrait and the right is the corresponding displacement and velocity.

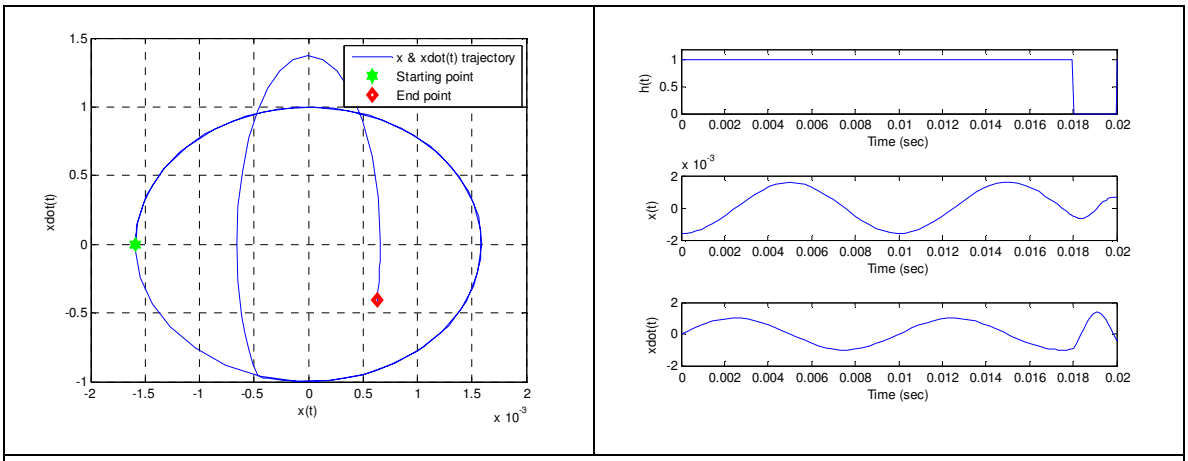

a) fs =50Hz, duty = 90%, time span=[0 0.02] sec

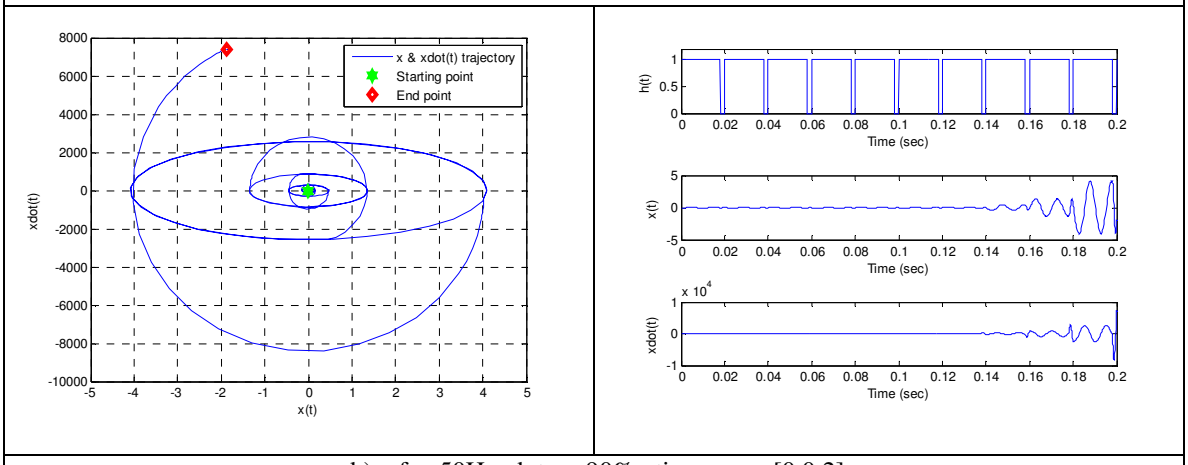

b) fs =50Hz, duty = 90%, time span=[0 0.2] sec

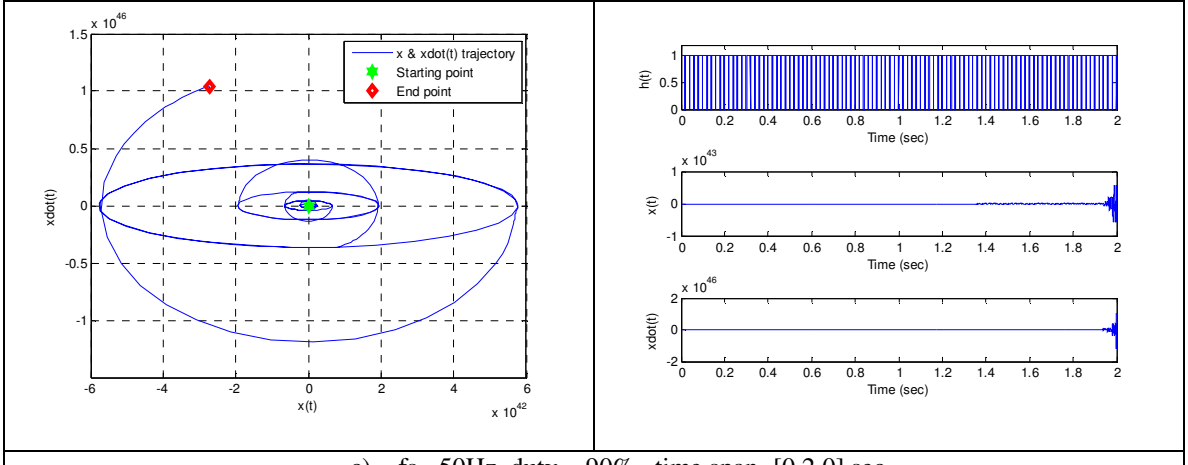

c) fs =50Hz, duty = 90%, time span=[0 2.0] sec

Figure A-7. Phase portrait diagram. The mass m is constant and the stiffness k varies. The switching frequency (fs) =50Hz, duty ratio = 90%. Simulation time increases downwardly. The left column is phase portrait and the right is the corresponding displacement and velocity.

Appendix B

This appendix decribes the details of the model for the shunt capacitance used in chapter 4. We construct a determined model and simulate the respond in time domain. Figure B-1 shows the simplified circuit model.

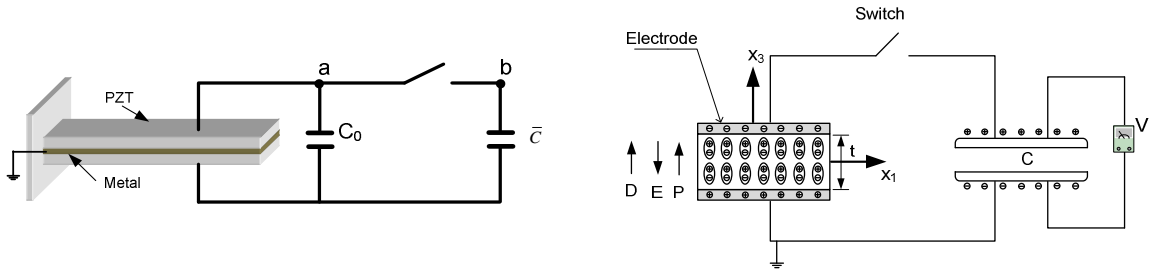

(a) The single-switched beam model (b) Simplified circuit model

Figure B-1. Schematic of peizelectric material shunted by the single capacitor and the simplified circuit model.

This numerical example is used to investigate the effect of switching frequency on the system response. Figure B-2 through Figure B-4 provide examples of simulation results for different driving frequencies. The voltage across the shunt circuit as a function of time is obtained when each switching frequency is employed.

As can be seen in the Figures, when a high PWM frequency signal is applied, there is no significant difference between the 500Hz and 1kHz cases as the duty cycle is varied. This case should be carefully contrasted with the case where the switching frequency set to 100Hz. The results suggest that the time constant associated with charging or discharging capacitance plays an important role in determining when the averaged system provides a good approximation of the original system. When the

switching frequency is too high relative to the time constant associated with the shunt capacitor, there is insufficient time interval to discharge or charge the capacitor. Thus, the numerical experiments suggest that there is insufficient time to vary capacitance in the shunt circuit at higher frequencies.

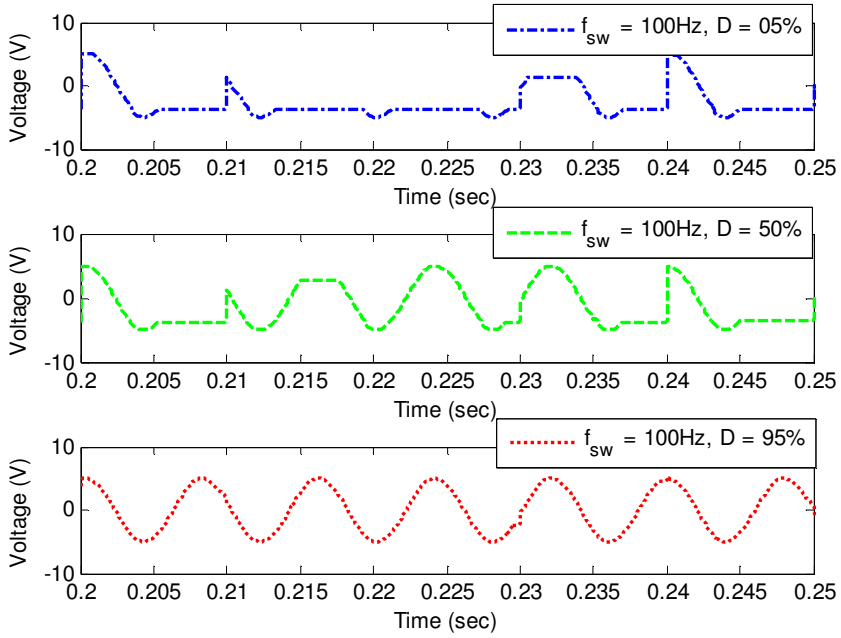

Figure B-2. Voltage across shunt capacitor: f_{sw} = 100Hz, Input source frequency(f_s) = 126Hz.

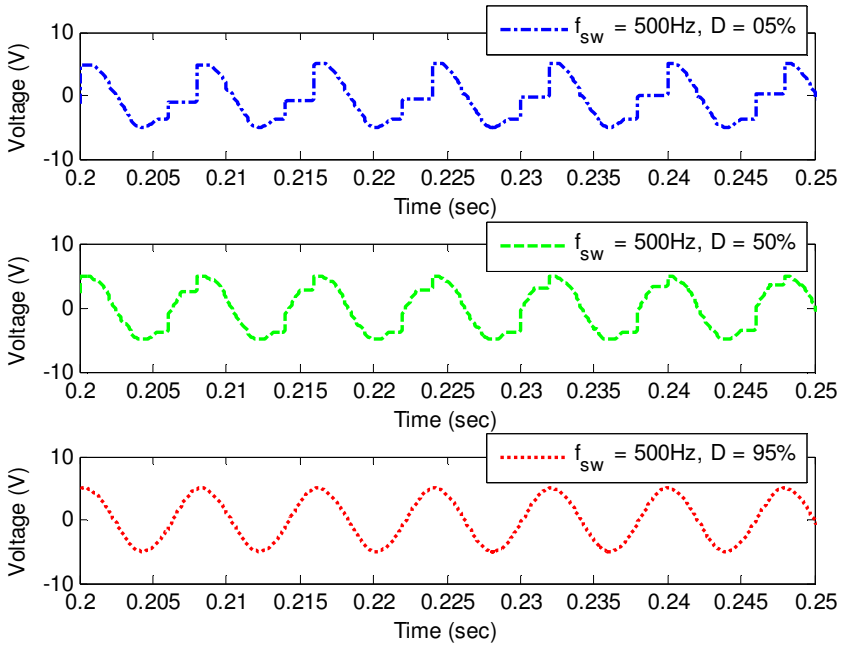

Figure B-3. Voltage across shunt capacitor: f_{sw}=500Hz, Input source frequency(f_s) = 126Hz.

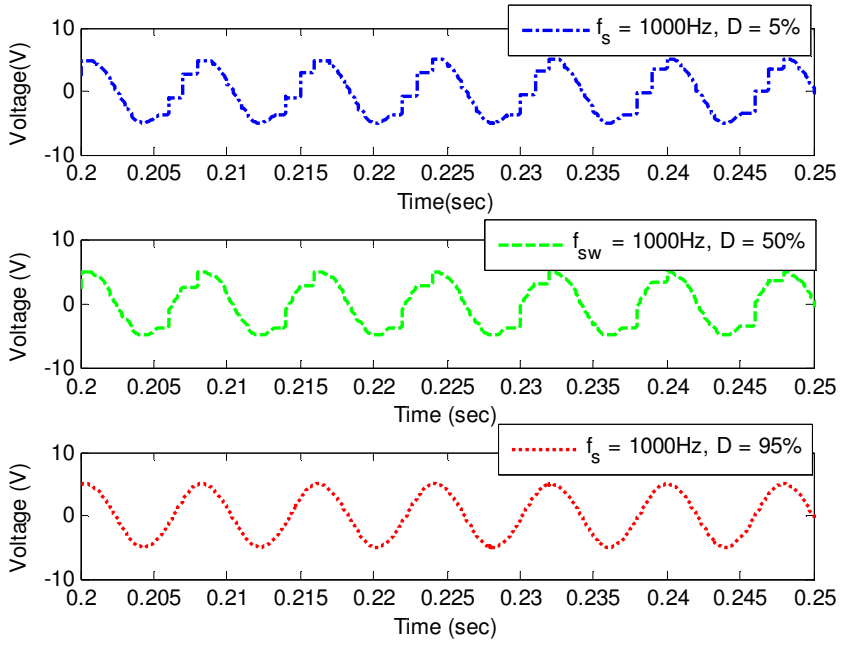

Figure B-4. Voltage across shunt capacitor: f_{sw} = 1kHz, Input source frequency(f_s) = 126Hz.

References

[1] Lesieutre, G.A., *Vibration damping and control using shunted piezoelectric materials.* Shock and Vibration Digest, 1998. **30**(3): p. 187-195.

[2] Tang, J., Liu, Y., and Wang, K.W., *Semiactive and active-passive hybrid structural damping treatments via piezoelectric materials.* Shock and Vibration Digest, 2000. **32**(3): p. 189-200.

[3] Clark, W.W., *Vibration control with state-switched piezoelectric materials.* Journal of Intelligent Material Systems and Structures, 2000. **11**(4): p. 263-271.

[4] Kim, W.K., Kurdila, A.J., and Butrym, B.A. *Analysis of Switching Systems using Averaging Methods for Piezostructures*. in *IMAC XXIX A Conference and Exposition on Structural Dynamics* 2010. USA.

[5] Davis, C.L. and Lesieutre, G.A., *Actively tuned solid-state vibration absorber using capacitive shunting of piezoelectric stiffness.* Journal of Sound and Vibration, 2000. **232**(3): p. 601-617.

[6] Lesieutre, G.A., Ottman, G.K., and Hofmann, H.F., *Damping as a result of piezoelectric energy harvesting.* Journal of Sound and Vibration, 2004. **269**(3-5): p. 991-1001.

[7] Kurdila, A.J., Lesieutre , G.A. , Zhanga, X., Prazenica, C., Niezrecki, C., *Averaging Analysis of State-Switched Piezoelectric Structural Systems.* Proceedings of SPIE, 2005. **Vol. 5760**: p. 413-422.

[8] Haertling, G.H., *Ferroelectric ceramics: History and technology.* Journal of the American Ceramic Society, 1999. **82**(4): p. 797-818.

[9] Collaboration, *IEEE standard on piezoelectricity*. 1988, Inst. Electr. & Electron. Eng., New York, NY, USA: USA. p. 54.

[10] Smith, R.C., *Smart material systems : model development*. Vol. xxvii, 501 p. :. 2005, Philadelphia :: Society for Industrial and Applied Mathematics.

[11] Ikeda, T., *Fundamentals of piezoelectricity*. Vol. xi, 263 p. :. 1990, Oxford ; New York :: Oxford University Press.

[12] Hagood, N.W., Chung, W.H., and von Flotow, A. *Modelling of piezoelectric actuator dynamics for active structural control*. 1990. New York, NY, USA: Publ by AIAA.

[13] Hagood, N.W. and von Flotow, A., *Damping of structural vibrations with piezoelectric materials and passive electrical networks.* Journal of Sound and Vibration, 1991. **146**(2): p. 243-68.

[14] Forward, R.L., *ELECTRONIC DAMPING OF VIBRATIONS IN OPTICAL STRUCTURES.* Applied Optics, 1979. **18**(5): p. 690-697.

[15] Davis, C.L. and Lesieutre, G.A., *A modal strain energy approach to the prediction of resistively shunted piezoceramic damping.* Journal of Sound and Vibration, 1995. **184**(1): p. 129-39.

[16] Wright, R., *A hierarchical noise control system using adaptable tuned vibration absorbers*. 2003, Virginia Polytechnic Institute and State University.

[17] Wang, B.T., Fuller, C.R., and Dimitriadis, E.K., *Active control of structurally radiated noise using multiple piezoelectric actuators.* AIAA Journal, 1991. **29**(11): p. 1802-1809.

[18] Burns, J.A., *Notes on Calculus of Variations With Modern Applications to Control Theory, Numerical Methods, and Differential Equations*. 2009.

[19] Fuller, C.R., et al., *Active control of interior noise in model aircraft fuselages using piezoceramic actuators.* AIAA Journal, 1992. **30**(11): p. 2613-17.

[20] Sodano, H.A., Park, G., and Inman, D.J., *An investigation into the performance of macro-fiber composites for sensing and structural vibration applications.* Mechanical Systems and Signal Processing, 2004. **18**(3): p. 683-697.

[21] Ormondroyd, J. and Den Hartog, J.P., *The theory of the dynamic vibration absorber.* American Society of Mechanical Engineers -- Transactions -- Applied Mechanics, 1928. **50**(17): p. 9-15.

[22] Den Hartog, J.P., *Mechanical vibrations*. Vol. xi, 436 p. ;. 1985, New York :: Dover Publications.

[23] Inman, D.J., *Engineering vibration*. 3rd. ed. ed. Vol. xiv, 669 p. :. 2008, Upper Saddle River, N.J. :: Pearson Prentice Hall.

[24] Roundy, S., *Energy scavenging for wireless sensor nodes with a focus on vibration to electricity conversion*, in *Mechanical Engineering*. 2003, The University of California, Berkeley.

[25] Kim, W., et al. *Averaging models for linear piezostructural systems*. 2009. USA: SPIE - The International Society for Optical Engineering.

[26] Hollkamp, J.J. and Starchville Jr, T.F., *Self-tuning piezoelectric vibration absorber.* Journal of Intelligent Material Systems and Structures, 1994. **5**(4): p. 559-566.

[27] Witsenhausen, H.S., *A class of hybrid-state continuous-time dynamic systems.* IEEE TRANSACTIONS ON AUTOMATIC CONTROL, 1966. **AC-11**(2): p. 161-167.

[28] Branicky, M.S., *Multiple Lyapunov functions and other analysis tools for switched and hybrid systems.* IEEE TRANSACTIONS ON AUTOMATIC CONTROL, 1998. **43**(4): p. 475-82.

[29] Larson, G.D., *The analysis and realization of a state switched acoustic transducer*, in *Mechanical Engineering*. 1996, Georgia Institute of Technology.

[30] Larson, G.D., Rogers, P.H., and Munk, W., *State switched transducers: a new approach to high-power, low-frequency, underwater projectors.* Journal of the Acoustical Society of America, 1998. **103**(3): p. 1428-41.

[31] Clark, W.W., *Semi-active vibration control with piezoelectric materials as variable stiffness actuators.* Proceedings of SPIE - The International Society for Optical Engineering, 1999. **3672**: p. 123-130.

[32] Corr, L.R. and Clark, W.W. *Comparison of low frequency piezoceramic shunt techniques for structural damping*. 2001. Newport Beach, CA, USA: SPIE-Int. Soc. Opt. Eng.

[33] Corr, L.R. and Clark, W.W., *A novel semi-active multi-modal vibration control law for a piezoceramic actuator.* Journal of Vibration and Acoustics, Transactions of the ASME, 2003. **125**(2): p. 214-222.

[34] Corr, L.R. and Clark, W.W., *Similarities between variable stiffness springs and piezoceramic switching shunts.* AIAA Journal, 2006. **44**(11): p. 2797-800.

[35] Dosch, J.J., et al. *Inertial piezoceramic actuators for smart structures*. 1995. San Diego, CA, USA: Society of Photo-Optical Instrumentation Engineers, Bellingham, WA, USA.

[36] Charnegie, D., et al. *Tunable piezoelectric cantilever beams for energy harvesting*. 2006. Chicago, IL, United states: American Society of Mechanical Engineers.

[37] Kim, W.K. and Kurdila, A.J., *SEMI-ACTIVE SWITCHING SYSTEMS FOR LINEAR PIEZOSTRUCTURES, accepted.* Journal of Intelligent Material Systems and Structures - Decision on Manuscript ID, 2012.

[38] Domme, D.J., *Experimental and Analytical Characterization of a Transducer for Energy Harvesting Through Electromagnetic Induction.* 2008, Virginia Polytechnic Institute and State University.

[39] DuToit, N.E., Wardle, B.L., and Kim, S.-G. *Design considerations for MEMS-scale piezoelectric mechanical vibration energy harvesters*. 2005. Cancun, Mexico: Taylor and Francis Inc., Philadelphia PA, PA 19106, United States.

[40] Lu, F., Lee, H.P., and Lim, S.P., *Modeling and analysis of micro piezoelectric power generators for micro-electromechanical-systems applications.* Smart Materials and Structures, 2004. **13**(1): p. 57-63.

[41] Sohn, J.W., Chor, S.B., and Lee, D.Y., *An investigation on piezoelectric energy harvesting for MEMS power sources.* Proceedings of the Institution of Mechanical Engineers, Part C (Journal of Mechanical Engineering Science), 2005. **219**(C4): p. 429-36.

[42] Sunghwan, K., Clark, W.W., and Qing-Ming, W., *Piezoelectric energy harvesting with a clamped circular plate: analysis.* Journal of Intelligent Material Systems and Structures, 2005. **16**(10): p. 847-54.

[43] Twiefel, J., et al. *Model-based design of piezoelectric energy harvesting systems*. 2006. USA: SPIE - The International Society for Optical Engineering.

[44] Roundy, S., *On the effectiveness of vibration-based energy harvesting.* Journal of Intelligent Material Systems and Structures, 2005. **16**(10): p. 809-823.

[45] Roundy, S., Wright, P.K., and Rabaey, J., *A study of low level vibrations as a power source for wireless sensor nodes.* Computer Communications, 2003. **26**(11): p. 1131-1144.

[46] Sodano, H.A., Inman, D.J., and Park, G., *Generation and storage of electricity from power harvesting devices.* Journal of Intelligent Material Systems and Structures, 2005. **16**(1): p. 67-75.

[47] Sodano, H.A., Inman, D.J., and Park, G., *Comparison of piezoelectric energy harvesting devices for recharging batteries.* Journal of Intelligent Material Systems and Structures, 2005. **16**(10): p. 799-807.

[48] Sodano, H.A., Park, G., and Inman, D.J., *Estimation of electric charge output for piezoelectric energy harvesting.* Strain, 2004. **40**(2): p. 49-58.

[49] DuToit, N.E. and Wardle, B.L., *Experimental verification of models for microfabricated piezoelectric vibration energy harvesters.* AIAA Journal, 2007. **45**(5): p. 1126-1137.

[50] Erturk, A. and Inman, D.J., *A distributed parameter electromechanical model for cantilevered piezoelectric energy harvesters.* Journal of Vibration and Acoustics, Transactions of the ASME, 2008. **130**(4).

[51] Erturk, A., Renno, J.M., and Inman, D.J., *Modeling of piezoelectric energy harvesting from an L-shaped beam-mass structure with an application to UAVs.* Journal of Intelligent Material Systems and Structures, 2009. **20**(5): p. 529-544.

[52] Elvin, N.G. and Elvin, A.A., *A Coupled Finite Element—Circuit Simulation Model for Analyzing Piezoelectric Energy Generators.* Journal of Intelligent Material Systems and Structures, 2009. **20**(5): p. 587-595

[53] Ottman, G.K., et al., *Adaptive piezoelectric energy harvesting circuit for wireless remote power supply.* IEEE Transactions on Power Electronics, 2002. **17**(5): p. 669-676.

[54] Ottman, G.K., Hofmann, H.F., and Lesieutre, G.A., *Optimized piezoelectric energy harvesting circuit using step-down converter in discontinuous conduction mode.* IEEE Transactions on Power Electronics, 2003. **18**(2): p. 696-703.

[55] Lallart, M., et al., *Double synchronized switch harvesting (DSSH): A new energy harvesting scheme for efficient energy extraction.* IEEE Transactions on Ultrasonics, Ferroelectrics, and Frequency Control, 2008. **55**(10): p. 2119-2130.

[56] Lallart, M., et al., *High efficiency, wide load bandwidth piezoelectric energy scavenging by a hybrid nonlinear approach.* Sensors and Actuators, A: Physical, 2011. **165**(2): p. 294-302.

[57] Erickson, R.W. and Marksimovic, D., *Fundamentals of Power Electronics*. 2004: Kluwer academic publishers.

[58] Bogoliubov, N.N. and Mitropolsky, Y.A., *Asymptotic methods in the theory of non-linear oscillations*. 1961: Gordon and Breach Science Publishers.

[59] Thomsen, J.J., *Vibrations and stability : advanced theory, analysis, and tools*. 2003: Berlin ; New York : Springer.

[60] Middlebrook, R.D. and Cuk, S., *A general unified approach to modelling switching-converter power stages.* International Journal of Electronics, 1977. **42**(6): p. 521-50.

[61] Sangswang, A. and Nwankpa, C.O., *Effects of switching-time uncertainties on pulsewidth-modulated power converters: Modeling and analysis.* IEEE Transactions on Circuits and Systems I: Fundamental Theory and Applications, 2003. **50**(8): p. 1006-1012.

[62] Witulski, A.F. and Erickson, R.W., *Extension of state-space averaging to resonant switches and beyond.* IEEE Transactions on Power Electronics, 1990. **5**(1): p. 98-109.

[63] Erickson, R.W., et al. *A nonlinear resonant switch*. 1989. New York, NY, USA: IEEE.

[64] Krein, P.T. and Bass, R.M. *A new approach to fast simulation of periodically switching power converters*. 1990. Seattle, WA, USA: Publ by IEEE.

[65] Krein, P.T., et al., *On the use of averaging for the analysis of power electronic systems.* IEEE Transactions on Power Electronics, 1990. **5**(2): p. 182-90.

[66] Craig, R.R. and Kurdila, A.J., *Fundamentals of structural dynamics* 2ed. 2006: John Wiley.

[67] Preumont, A., *Mechatronics : dynamics of electromechanical and piezoelectric systems*. Vol. xv, 207 p. :. 2006, Dordrecht :: Springer.

[68] Sun, J. and Grotstollen, H. *Averaged modelling of switching power converters: reformulation and theoretical basis*. 1992. Toledo, Spain: IEEE.

[69] Kurdila, A.J., et al., *Stability of a class of real-time switched piezoelectric shunts.* Journal of Intelligent Material Systems and Structures, 2002. **13**(2-3): p. 107-116.

[70] Sanders, J.A., Verhulst, F., *Averaging methods in nonlinear dynamical systems* 1985: New York: Springer-Verlag.